Step-scheme photocatalysts: Promising hybrid nanomaterials for optimum conversion of CO2

Yakubu Adekunle Alli, Peter Olusakin Oladoye, Funeka Matebese, Naomi Senehi, Oyekunle Azeez Alimi, Adeniyi Sunday Ogunlaja, Fatwa Abdi, Hazleen Anuar, Adeyemi Adeleye, Karine Philippot

Step-scheme Photocatalysts: Promising Hybrid Nanomaterials for Optimum Conversion of CO_2

Yakubu Adekunle Alli[a,b,c**], Peter Olusakin Oladoye[d], Funeka Matebese[e,j], Naomi L. Senehi[f], Oyekunle Azeez Alimi[g], Adeniyi Sunday Ogunlaja[e*], Fatwa F. Abdi[h,I], ,Hazleen Anuar[c], Adeyemi S. Adeleye[f*], Karine Philippot[a]

[a]CNRS, LCC (Laboratoire de Chimie de Coordination), UPR8241, Université de Toulouse, UPS, INPT, Toulouse cedex 4 F-31077, France.

[b]Department of Chemical Sciences, Faculty of Science and Computing, Ahman Pategi University, Patigi-Kpada Road, Patigi, Kwara State, Nigeria

[c]Department of Manufacturing and Materials Engineering, Kulliyyah of Engineering, International Islamic University Malaysia, Jalan Gombak, 53100 Kuala Lumpur, Malaysia

[d]Department of Chemistry and Biochemistry, Florida International University, 11200 SW 8th St, Miami, FL, 33199, USA

[e]Department of Chemistry, Nelson Mandela University, Gqeberha (Port Elizabeth), South Africa

[f]Department of Civil and Environmental Engineering, University of California, Irvine, CA 92697-2175, USA

[g]Research Center for Synthesis and Catalysis, Department of Chemical Sciences, University of Johannesburg, PO Box 524, Auckland Park, Johannesburg 2006, South Africa

[h]Institute for Solar Fuels, Helmholtz-Zentrum Berlin für Materialien und Energie GmbH, Hahn-Meitner-Platz 1, 14109 Berlin, Germany

[i]School of Energy and Environment, City University of Hong Kong, Kowloon, Hong Kong, People's Republic of China

[j]Institute for Nanotechnology and Water Sustainability, College of Science, Engineering and Technology, University of South Africa, Florida, 1709, Johannesburg, South Africa

Abstract

The appealing prospect of photocatalysts as an environmentally friendly method for converting atmospheric CO_2 into value-added products is undeniable, and scientists are working hard to further enhance their performance. This review outlines the most recent developments in the

synthesis, characterization, computational insights, and emerging application of Step-scheme (S-scheme) photocatalysts in CO_2 transformation into value added products. The review begins with a survey of different generations of heterojunctions and the challenges associated with each heterojunction generation. S-scheme heterojunctions are therefore suggested as a solution to the drawbacks of type-II and Z-scheme family heterojunctions, and the underlying reaction mechanism of S-scheme is critically outlined. The different synthesis approaches for the design of S-scheme heterojunctions are discussed. Following this, direct characterization techniques and emerging computational methods to identify the charge transfer mechanism in S-scheme heterojunctions are presented. Furthermore, emerging applications of S-scheme photocatalysts in CO_2 transformation into value-added products are critically surveyed from recent literature. Finally, the current challenges and prospects of the S-scheme heterojunction photocatalyst are discussed.

Keywords: S-scheme photocatalysts, CO_2 conversion, heterojunction, computational method

Table of contents

1. Introduction

The year 2022 was the sixth warmest year on record, with an average global temperature that was 1.06°C higher than the pre-industrial period (1880-1900) [1]. This increase in temperature is accompanied by increasing sea level rise and a high occurrence of harsh weather events, such as tropical cyclones, drought, severe fluvial floods, and wildfires [2]. These climate changes are reportedly caused by increasing anthropogenic emissions of greenhouse gases (GHGs) in the atmosphere, with carbon dioxide (CO_2), at an emission of 45 ± 5.5 $GtCO_2$-eq in 2019, accounting for the majority of the emitted GHGs. As the atmospheric concentration of CO_2 is increasing at a rate of 2.47 ppm/year (as of 2021) [3,4], there is an urgent need to stabilize the atmospheric abundance of CO_2 to limit the warming of the planet and mitigate the risks of climate change [5].

Strategies for lowering existing CO_2 emissions include capturing, utilizing, and sequestering CO_2 through natural and engineering techniques [6–8] for purposes such as fuel production. Because the high thermodynamic stability of CO_2 ($\Delta G_f^0 = -394.4\ \mathrm{kJ/mol}$) limits its reactivity [9,10], to produce fuel, CO_2 must first be reduced. The photoreduction of CO_2 is espcially promising as certain photocatalysts, such as Step-scheme (S-scheme) photocatalysts, have an enhanced redox potential that may overcome this energy barrier [11]. In general, photoreduction occurs when a light source activates a semiconductor via light absorption [12], causing electrons to be excited from the valence band (VB) to the conduction band (CB). The electron holes and free electrons generated can, in the presence of hydrogen (e.g. in water), migrate to the surface of the photocatalyst. Here, through redox reactions, the electron holes and free electrons reduce CO_2 to

produce CO and various carbon species, such as methanol [13–16]. In an ideal system CO_2 would be reduced all the way to O_2 and H^+, however the lack of a photocatalyst that can (1) prevent recombination, (2) exhibit a large band gap/absorb broad sunlight, and (3) retain redox power [17] limits this achievement.

Since first reported by Inoue et al. [18], efforts to enhance the effectiveness of photocatalytic reduction of CO_2 have intensified. S-scheme heterojunctions for the reduction of CO_2, as well as for the degradation of other environmental contaminants including antibiotics [19][20], nitric oxide [21][22], and organic compounds [23,24], are gaining rapid popularity **(Figure 1)**. S-scheme photocatalysts overcome some of the challenges of mono-component photocatalysts, which include the contrasting need for a narrow band gap (for high solar light absorption efficiency) and possession of a high CB and low VB for strong redox ability. Aside from the aforementioned improved redox power, S-scheme heterojunctions are particularly suited for CO_2 reduction as they exhibit enhanced charge separation which allows a greater proportion of the generated species to react with CO_2 (rather than recombine) [25]. Various studies have explored the use of S-scheme heterojunctions for CO_2 reduction which has been discussed in several recent reviews. These reviews mainly focused on the diversity of materials used for CO_2 conversion [25] and the general fabrication and applications of S-scheme photocatalysts [26,27]. What has yet to be emphasized, and will be in this review, are the identification methods and heterojunction types of S-scheme photocatalysts for CO_2 conversion.

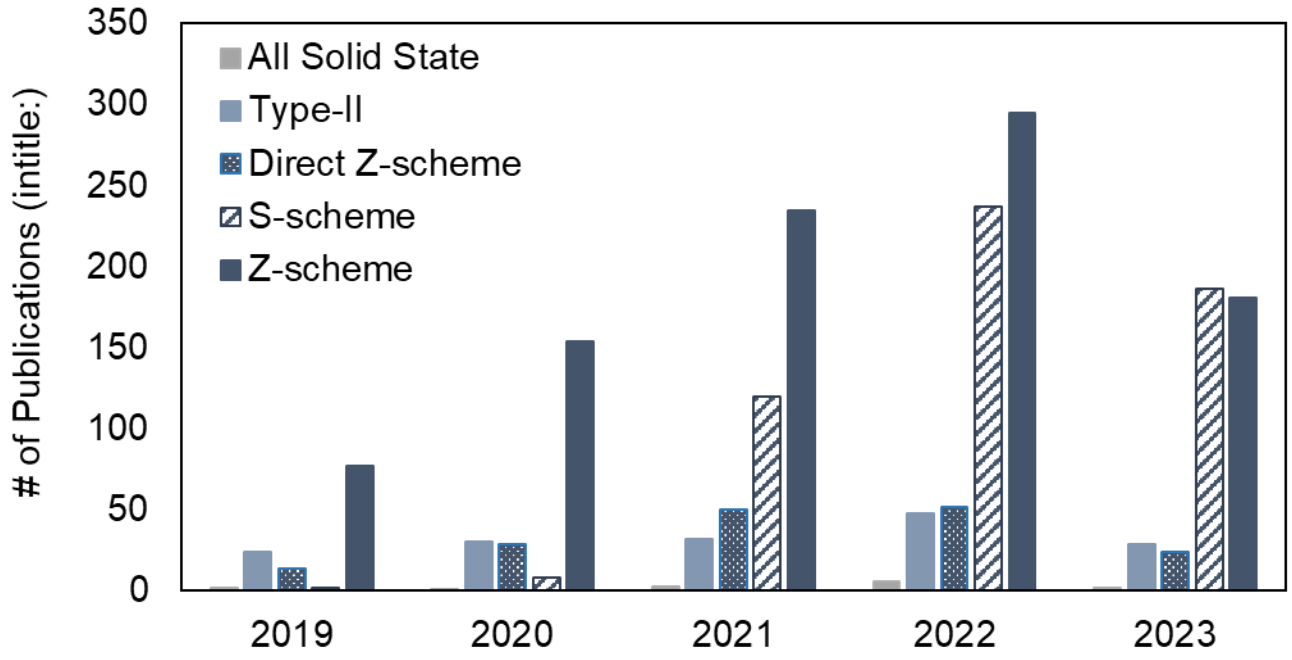

Fig. 1. Web of Science publication report (in August 2023) for search terms intitle: all solid-state heterojunction, type II heterojunction, direct Z-scheme heterojunction, S-scheme heterojunction, and Z-scheme heterojunction.

The goal of this review is to complement existing reviews by summarizing the evolution, identification and synthesis of S-scheme heterojunctions and evaluating their use for CO_2 reduction in particular. Firstly, an overview of their evolution, including the fundamentals of their mechanisms of operation, serves to highlight the unique ability of S-scheme heterojunction to overcome the challenges of other heterojunctions. The routes for synthesizing and characterizing S-scheme heterojunctions are outlined, followed by a detailed description of the applications of different types of S-scheme heterojunctions (n-n, p-p, n-p and p-n). Next, successful applications of S-scheme heterojunctions for CO_2 transformation to value added products are highlighted. Finally, key research gaps and topics for future work are described, and suggestions for addressing the inadequacies of S-scheme photocatalysts are provided.

2. Historical evolution of heterojunctions

One of the approaches to improving the efficiency of photocatalysts is the formation of a heterojunction [28,29]. A heterojunction is an interface made up of two different layers of semiconductors or regions [30] and improves their photocatalytic properties over their individual

counterparts. In contrast to homojunctions, these semiconducting materials have staggered/unequal band gap configurations which enhance the charge transfer. Heterojunctions have evolved since their inception from the late 1970s to date as shown in **Figure 2** and can be divided into five generations. This section critically examines the historical evolution of heterojunctions and their respective benefits and shortcomings.

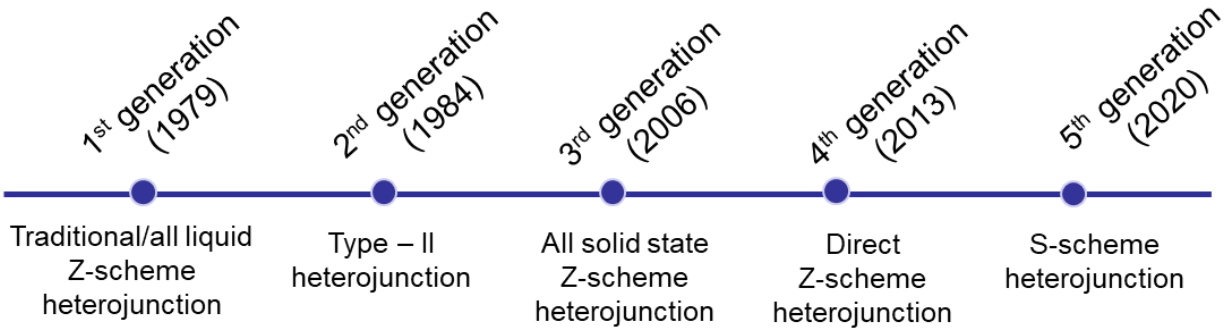

Fig. 2. A timeline of the evolution of heterojunction photocatalysts.

2.1. First generation - Traditional Z-scheme Heterojunction (1979)

Several heterojunction schemes have been constructed to ameliorate the above-mentioned challenges in mono-photocatalysts. The genesis of heterojunction construction can be traced back to 1979 when Bard developed what is generally known as traditional/all liquid phase Z-scheme photocatalysts [31]. Since then, traditional Z-scheme photocatalysts have received considerable attention and have remained relevant for several decades. Typically, this system comprises of two semiconductors with staggered band structures and suitable shuttle redox ion mediators that can act as electron-bridge between the two semiconductors/photocatalysts. The first common shuttle redox ion pair, IO_3^-/I^-, was discovered in 1997 while the second common intermediate couple, Fe^{3+}/Fe^{2+}, was first reported in 2001 [32,33]. I_3^-/I^- has also been reported as a suitable redox shuttle ion chain for the construction of traditional Z-scheme photocatalysts.

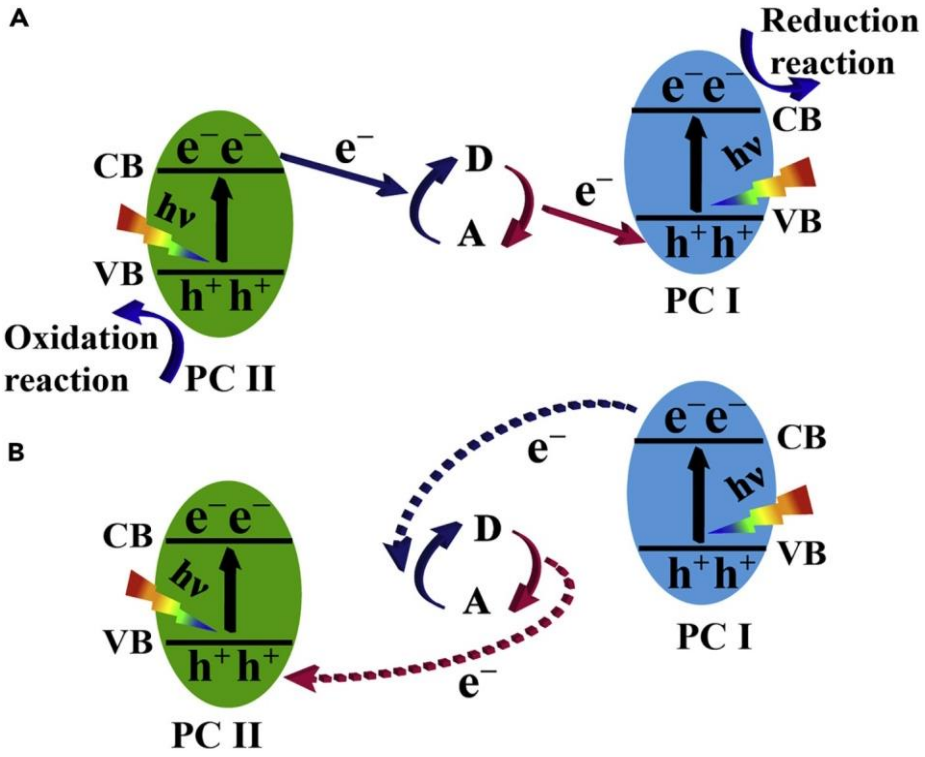

Fig. 3. (A) Supposed and (B) real charge transfer mechanisms of traditional Z-scheme heterojunctions. Printed with permission from [34]. Copyright 2020, Elsevier.

In a typical traditional Z-scheme charge transfer mechanism, as shown in **Figure 3A**, photogenerated positive holes in the VB position of photocatalyst I (PC I) are consumed by electron donors in the intermediate ion mediator whereas the photoexcited electrons in the CB position of photocatalyst II (PC II) are consumed by electron acceptors. Subsequently, the preserved electrons in the CB of PC I and holes in the VB of PC II participate in the reduction and oxidation reactions, respectively. However, the supposed charge transfer mechanism is thermodynamically not reasonable. Because the photogenerated electrons in the CB of PCI possess more reducing power compared to PCII, the electrons are more prone to A than to D (i.e., Fe^{3+} to Fe^{2+}). In the same manner, photogenerated holes in VB position of PCII have greater oxidizing potential compared to those in PCI and are more inclined to gain electrons from D ions. As such, the charge transfer mechanism shown in **Figure 3B** is more thermodynamically favorable. It is important to mention that traditional Z-scheme heterojunctions suffer from (1) light shielding, (2) limited applicability to the solution phase only, (3) back/side reactions, (4) pH

sensitivity, and (5) a thermodynamically unfavorable real charge transfer mechanism (**Figure 3B**). In the light of these weaknesses, new generations of heterojunction were proposed.

2.2. Second generation - Type-II Heterojunction (1984)

In an unrelenting search for photocatalysts that can fulfill all the universal conditions for an effective photocatalytic reaction, Serpone and co-workers introduced a new scheme named type-II heterojunction in 1984 [35]. The group first reported the inter-particle electron transfer to proffer solution to the fast recombination of electron-hole pairs in mono photocatalysts. It was later upgraded in conjunction with Bedja *et al*. from inter-particle electron transfer to inter-particle hole transfer when two combined semiconductors displayed staggered band structures [33,36].

This scheme is made up of a photocatalyst I (SI) and a photocatalyst II (SII) with staggered band configurations. When S I and SII are subjected to irradiation, photogenerated electrons in the CB of the SI semiconductor migrate to the CB of the SII semiconductor while photogenerated positive holes in the CB of the S I semiconductor migrate to the CB of the S II semiconductor (**Figure 4**). Although this generation of heterojunction photocatalyst received considerable attention since it was introduced, it still suffers from thermodynamic (i.e., the transfer mechanism results in lower redox potential of photoelectrons and holes), dynamic (i.e., the photogenerated electrons in CBs of SI and S2 repel, likewise the photogenerated holes repels the VB position), and energy issues (i.e., results in loss of energy in the photocatalytic system). These issues reduce its charge separation efficiency and limit the photocatalytic activity. Additional details of these issues are provided by other publications [12,33,36].

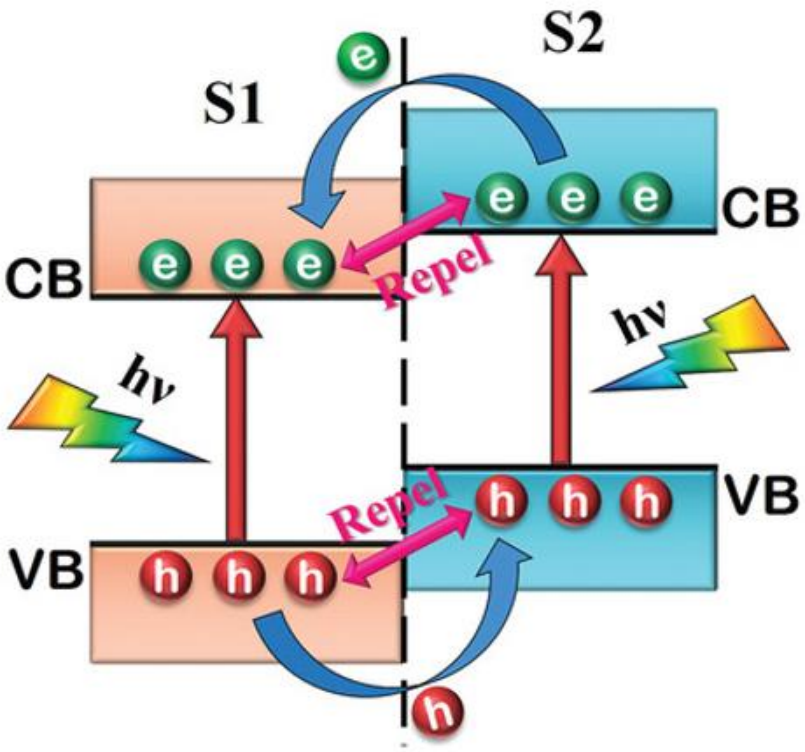

Fig. 4. Charge transfer mechanism of type II heterojunction. Printed with permission from [33]. Copyright 2022, Willey Online Library.

2.3. Third generation - All solid-state Z-scheme heterojunction (2006)

In order to resolve the charge transfer issues and broaden the application scope of the first and second generation heterojunctions, Tada *et al*. designed a new generation of heterojunction, called all solid state Z-scheme heterojunction in 2006 [30,36]. Typically, this scheme consists of two semiconductors with staggered band structure, and solid conductors such as platinum or gold nanoparticles are employed instead of shuttle redox ion mediators (which are used in all liquid state Z-scheme). In principle, when the all-solid state Z-scheme heterojunction is subjected to light irradiation, photogenerated electrons in the CB of S1 transfer to the solid conductor and subsequently migrate to the VB of S2 (**Figure 5a**). The advantage of this scheme over the traditional Z-scheme is that it can be used in liquid and gaseous state. In addition, the charge transfer length is significantly shortened, which, in turn, enhances charge transfer. The real/favorable charge transfer mechanism from the thermodynamic point of view is presented in **Figure 5b**.

Amongst other weaknesses, studies have shown this assumed charge transfer route is thermodynamically unreasonable and the practical application of this scheme suffers a major setback. Firstly, the conducting metal at the center possesses a lower Fermi energy (E_f) level compared to the semiconductor [36]. This results in band bending and formation of two Schottky junctions at the interface, which create barriers for effective migration of photoelectrons at the interface. Secondly, it is difficult to place the metal at the center precisely and some noble metals used as mediators for charge carrier transfer are pricey. Thirdly, the noble metal NPs could result in shielding effect [37].

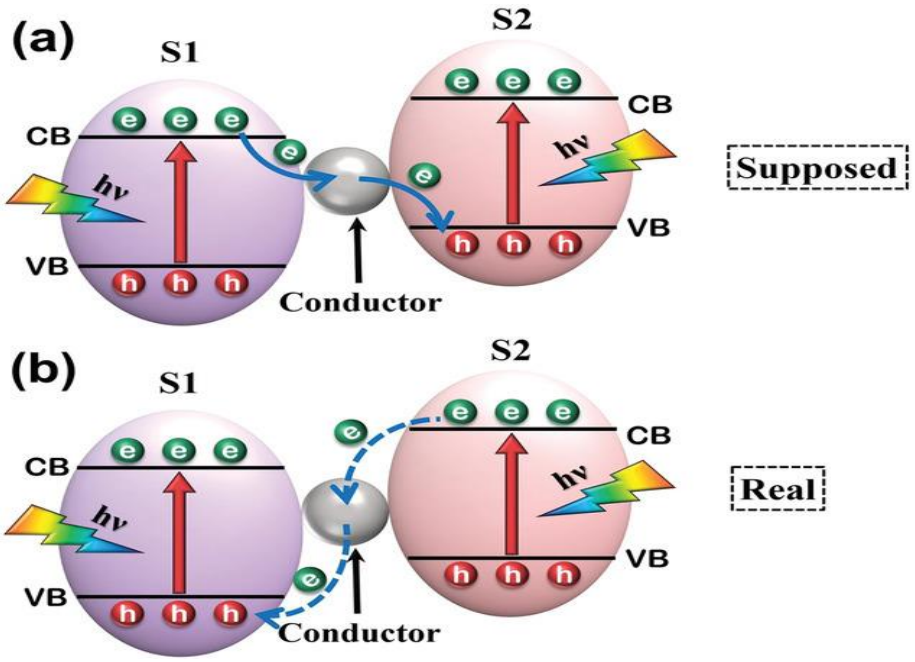

Fig. 5. (A) Supposed and (B) real charge transfer mechanism of the all-solid state Z-scheme heterojunction. Printed with permission from [33]. Copyright 2022, Willey Online Library.

2.4. Fourth generation - Direct Z-scheme heterojunction

The idea of a fourth generation otherwise known as "direct Z-scheme" was introduced intermittently and gradually developed. The oldest of this scheme is in dye-sensitized TiO_2 which dates back about 22 years when Grätzel and colleagues [38] developed a tandem cell by combining nanocrystalline WO_3 or Fe_2O_3 (top layer) with dye-sensitized TiO_2 (bottom layer). However, "direct Z-scheme" is widely misunderstood, in part because its first and second generations—traditional Z-scheme and all-solid-state scheme—are regarded as premature and

problematic. Furthermore, science has evolved and changed over time. The understanding and verification of how electrons transfer is becoming more robust. This made it necessary to look for a new generation of heterojunction that wouldn't have any issues with charge transfer, dynamics, or thermodynamics.

2.5. S-scheme heterojunction

In the year 2020, a group led by Wang [39] introduced a new generation of heterojunction, named Step-scheme (S-scheme), with a plausible and unambiguous mechanism of charge transfer. Since then, S-scheme photocatalysts have attracted tremendous attention particularly for CO_2 reduction, environmental remediation, bacterial disinfection, and hydrogen production. It is pertinent to mention that S-scheme was inspired by the direct Z-scheme generation.

A typical S-scheme heterojunction comprises of a reduction photocatalyst (RP) and an oxidation photocatalyst (OP). The universal condition for the design and development of S-scheme is that the CB and Fermi energy (E_f) of RP must simultaneously be higher than that of the CB and the Fermi level of OP. It was previously assumed that when the OP and RP come in close proximity, the electrons in the RP will migrate continuously to OP until E_f level attains equilibrium at their interface (**Figure 6a**). However, recent studies revealed that the E_f level bends within the interface when the RP and OP come into contact (**Figure 6b)** [37]. This implies that the E_f of RP and OP gradually decrease and increase at the interface, respectively, while the E_f of both at the bulk region remains the same.

The rationale behind the possible migration of electrons from RP to OP can be attributed to higher E_f of RP. As a result of this migration, an internal electric field directing from RP to OP will build up at the interface. In addition, the upward and downward movement of E_f of the two semiconductors will result in band bending at the interface. When the composites are subjected to light irradiation, electrons get excited from VB to CB, which subsequently generates photoelectrons and electron holes. The weak photogenerated electrons in the CB of OP will then combine with the holes in the VB of RP under the influence of the internal electric field, band bending, and columbic attraction, while the powerful electrons and holes in the CB of RP and VB of OP will eventually participate in reduction and oxidation reactions, respectively.

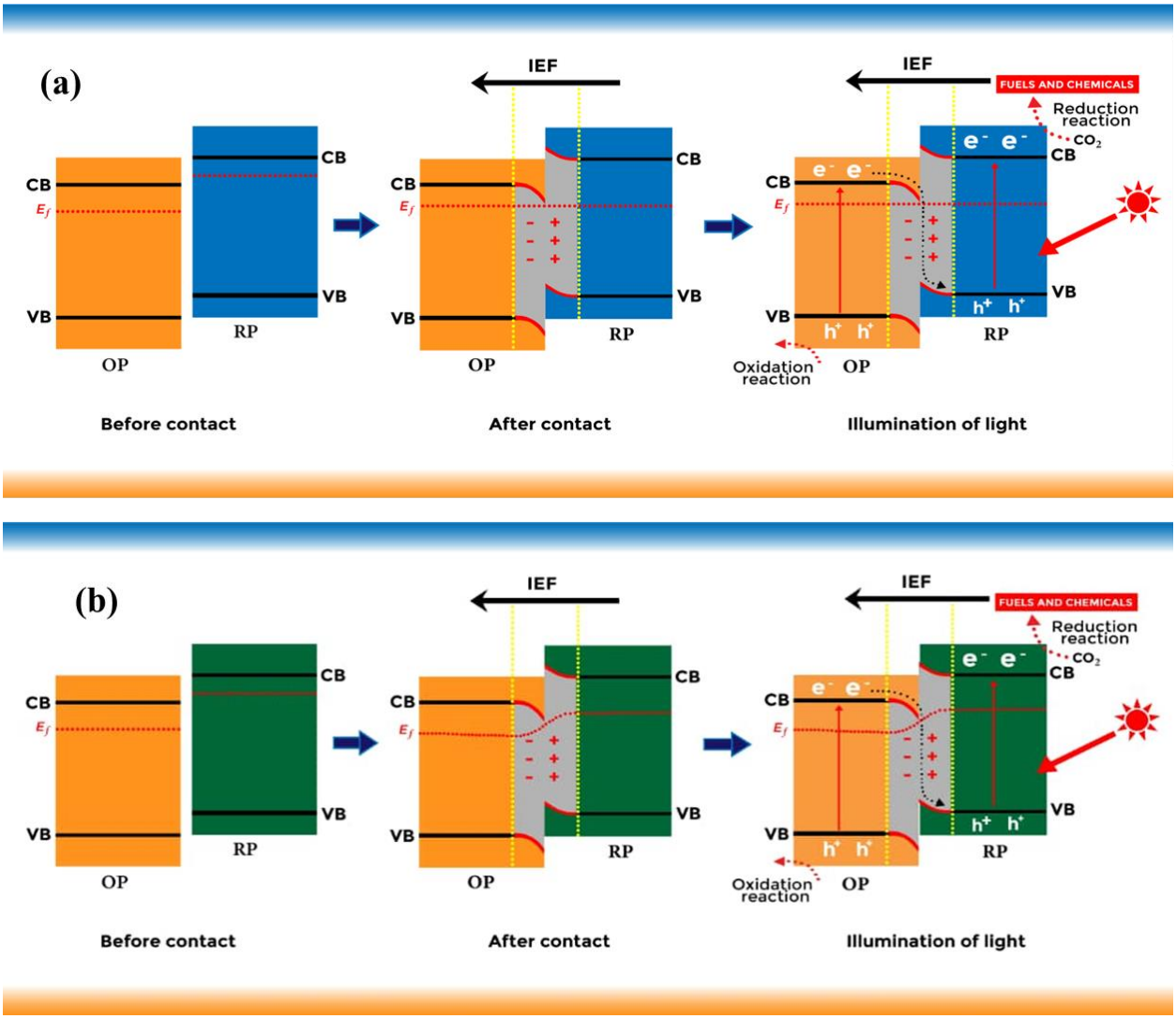

Fig. 6. Charge transfer mechanism of a S-scheme heterojunction: (a) supposed Fermi energy level distribution and (b) real Fermi energy level distribution (before contact, after contact and under illumination).

3. Identification of S-Scheme photocatalysts

Different approaches have been used to identify S-scheme photocatalysts. Theoretically, the S-scheme photocatalyst is identified by the unique "S" figure of the charge carrier, which facilitates the highest redox ability [40]. Experimentally, the S-scheme photocatalysts can be identified by certain spectroscopic techniques, including ex situ and in situ irradiated X-ray photoelectron spectroscopy (XPS), electron paramagnetic resonance (EPR), and Kelvin probe

force microscopy (KPFM) [34]. In situ and ex situ irradiated XPS and AFM are classified as direct identification techniques, while EPR, is classified as indirect techniques [37].

3.1. Kelvin probe force microscopy (KPFM)

KPFM is a derivative of atomic force microscopy (AFM). It relies on the ability to precisely measure the surface potential or contact potential difference (CPD) of the photocatalytic material while also scanning its surface to determine morphology [41]. In practice, the CPD measurement is based on the contact potential difference between the Kelvin probe and the material, suggesting the presence of electron transfer between the heterostructures. The obtained CPD value is the driving force for the charge transfer in the heterojunction composite. The procedure is usually carried out under three different conditions, namely before contact, after contact, and after light irradiation conditions.

Liu *et al.* [42] reported a successful synthesis of ZnO/g-C_3N_4 S- scheme heterojunction, which was characterized by KPFM. The charge transfer process in the catalyst is presented in **Figure 7**. The KPFM technique can also generate a topographic map based on the electron distribution on the sample surface thus providing a visual representation of the S -scheme heterojunction.

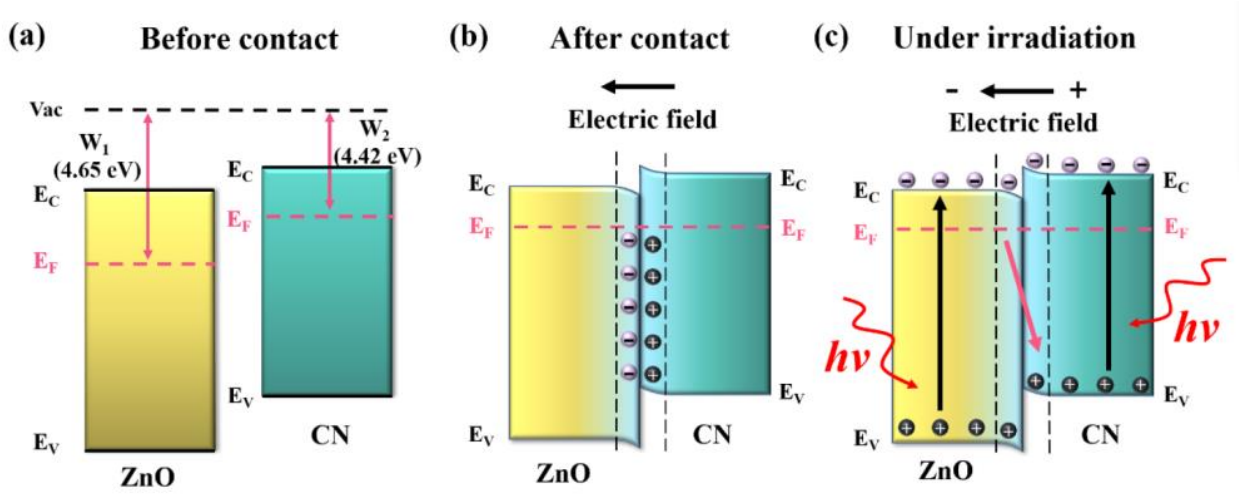

Fig. 7. Charge transfer process of a ZnO/g-C_3N_4 S-scheme heterojunction (a) before contact, (b) after contact, and (c) under illumination. Data was obtained via KPFM. Adapted with permission from [42]. Copyright (2021) American Chemical Society.

3.2. Ex situ and in situ irradiated X-ray photoelectron spectroscopy (XPS)

XPS is an important characterization technique used for the characterization of S-scheme photocatalysts. Specifically, it is used to determine the surface electronic chemical composition and interactions at the heterojunctions [40]. In particular, the ability of high-resolution ex situ and in situ irradiated XPS (ISI-XPS) to measure chemical shifts arising from elemental binding energy in the presence and absence of light irradiation is important to evaluate the differences in electron density [43].

The chemical shift measured by XPS originates from the migration of electrons resulting in a difference in the binding energies. Usually, when electrons are injected into a material, its binding energy decreases, and vice versa. Therefore, XPS gives information about electron movement and charge transfer in S-scheme photocatalysts. **Figure 8** represents an example of a typical S-scheme transfer route illustrated by XPS, which was obtained from an α-Fe_2O_3/Cu_2O S-scheme photocatalyst for the oxidative coupling of amines [44].

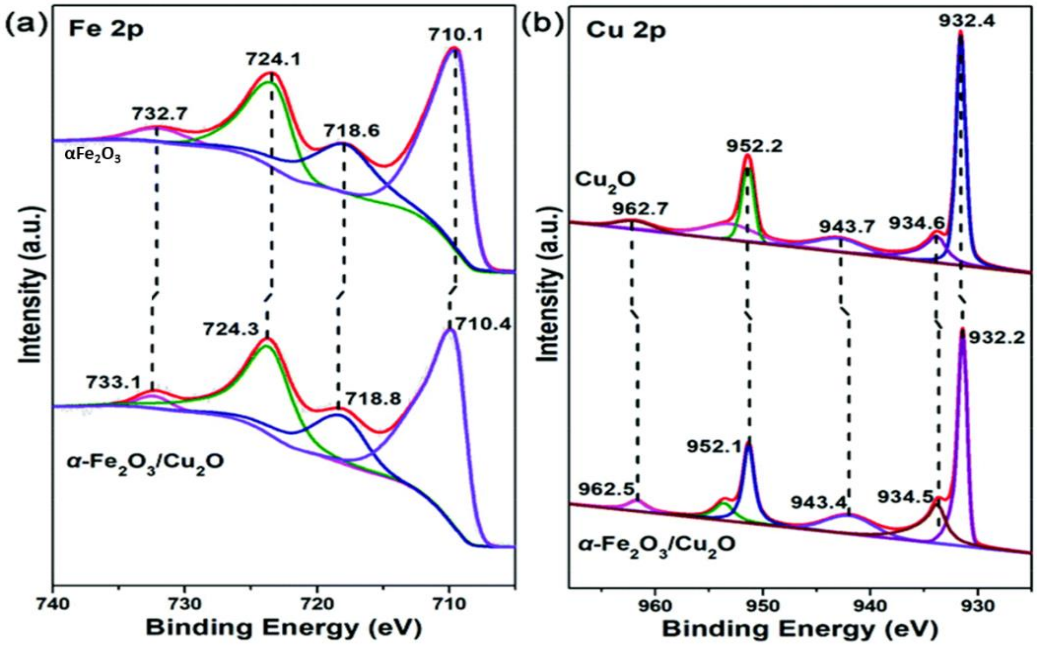

Fig. 8. High resolution XPS spectra of an α-Fe_2O_3/Cu_2O S-scheme photocatalyst showing the (a) electron transfer between Fe_2O_3 and α-Fe_2O_3/Cu_2O and (b) electron transfer between Cu_2O and α-Fe_2O_3/Cu_2O. Adapted from [44]. Copyright (2022) Royal Society of Chemistry.

The XPS spectra illustrated the electron transfer within the composite catalyst. In **Figure 8a**, the peaks at 721.4 and 710.1 eV in α-Fe_2O_3, which were assigned to Fe $2p_{3/2}$ and Fe $2p_{½}$, respectively, confirmed the existence of Fe^{3+} in α-Fe_2O_3 [45]. Also, the two satellite peaks at 732.7 and 718.6 eV further confirmed the presence of Fe^{+} in α-Fe_2O_3 [46]. Noticeably, in the Fe_2O_3/Cu_2O composite, all the peaks assigned to Fe^{3+} shifted positively with respect to the Fe_2O_3/Cu_2O, suggesting a movement of electrons around Fe^{3+} to the Fe_2O_3/Cu_2O composite [47]. Moreover, the presence of Cu was confirmed by two distinct peaks at 932.4 and 952.2 eV (**Figure 8b**), which correspond to Cu $2p_{3/2}$ and Cu $2p_{½}$, respectively, and signifies the presence of copper ions [48]. Other smaller peaks at 934.6, 943.7 and 962.7 eV could be assigned to the Cu $3d^9$ configuration of CuO in the ground state [49]. However, in the Fe_2O_3/Cu_2O composite, all characteristic peaks assigned to Cu_2O shifted negatively with respect to the α-Fe_2O_3/Cu_2O, signifying an increase in an electron cloud density around Cu [44].

Similarly, Xu *et al*. reported the preparation of a TiO_2/Ce_2S_3 S-Scheme photocatalyst (TC5) [50]. XPS was used to confirm the composition of the catalyst and study the migration of electrons within the composite catalyst (**Figure 9)**. The two symmetric peaks at approximately 458.5 and 464.3 eV in pristine TiO_2 correspond to Ti $2p_{3/2}$ and Ti $2p_{½}$, respectively (**Figure 9a**), which confirms the presence of Ti^{4+} in the TiO_2 samples [39]. In the TC5 sample, the TiO_2 characteristics peaks slightly shifted negatively, an indication of electron transfer from TC5 to TiO_2. However, the reverse was observed when TC5 was exposed to UV light (TC5-UV), with the characteristic peaks for the Ti^{4+} shifted positively. These reverse shifts can be attributed to the generation of photoinduced charge carriers.

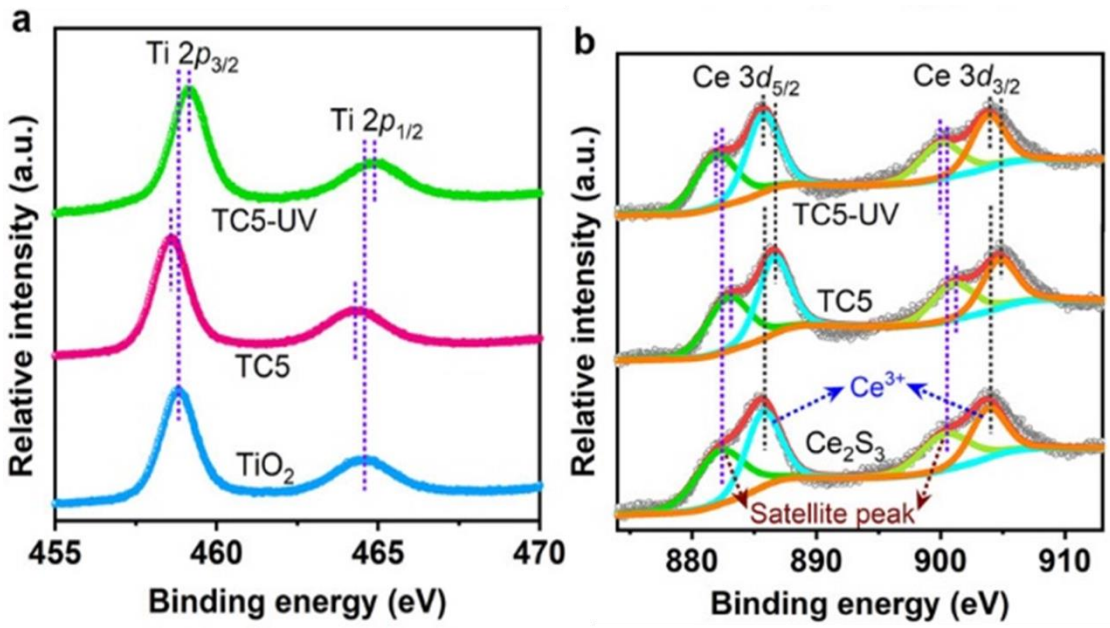

Fig. 9. XPS spectra of (a) Ti 2p and (b) Ce 3d of TiO_2, Ce_2S_3, and TC5, demonstrating electron transfer between TiO_2 nanofibers and Ce_2S_3 nanoparticles. Reproduced with the permission from [50]. Copyright (2022) American Chemical Society.

Two pairs of signals were observed in the high resolution XPS spectra for Ce^{3+} (**Figure 9b**). The first pair, at 885.8 and 903.9 eV, are indicative of Ce^{3+} in Ce_2S_3. The second pair, at 882.4 and 900.5 eV, are the satellite peaks of Ce^{3+} [50]. All peaks attributed to the Ce^{3+} in Ce_2S_3 shifted positively in TC5, compared to pure Ce_2S_3, under dark conditions. However, in the presence of light (TC5-UV), the Ce^{3+} peaks downshifted. This changing trend in the binding energy confirms the formation of S-Scheme heterojunction which can be observed by the XPS technique.

3.3. Electron Paramagnetic Resonance (EPR)

EPR, also referred to as electron spin resonance (ESR) is one of the dominant techniques for identifying S-scheme photocatalysts because of its sensitivity and exceptional ability [51,52]. Unlike other methods, the EPR spectroscopic technique has the unique ability to measure the paramagnetic moments and unpaired electrons in any catalytic samples [53]. It is important to mention that the sensitivity of EPR is towards one or more unpaired electrons and it is blind to materials with diamagnetic properties. Although this seems to be a limitation, the selectivity for unpaired electrons is a clear advantage [53]. To identify S-scheme photocatalysts using EPR, an

appropriate spin trapping agent, such as 5,5-Dimethyl-l-pyrroline N-oxide (DMPO), is used to detect active free radicals such as hydroxyl radical (•OH) and superoxide ($\cdot O_2^-$) [51].

For instance, Dong *et al* [54] demonstrated the applicability of EPR for studying the S-scheme mechanism in their prepared $CsPbBr_3/Cu_2O$ photocatalyst. There was apparently no DMPO-•OH signal from $CsPbBr_3$ under visible light conditions, which suggests a low oxidation potential (E_{vb}) of its photoinduced holes (**Figure 10a).** Strong DMPO-•OH signals were however observed in $CsPbBr_3/CuO_2$, which suggests that the oxidation potential is much higher in the heterocycle due to the accumulation of photogenerated holes. Unlike DMPO-•OH, the characteristic signal for DMPO-$\cdot O_2^-$ was observed in all the samples ($CsPbBr_3$, CuO_2, and $CsPbBr_3/CuO_2$). The intensity of the DMPO-$\cdot O_2^-$ signal observed in the samples was in the order $CsPbBr_3 < CuO_2 <$ CPB/CuO_2, which suggests the accumulation of electrons in the $CsPbBr_3/CuO_2$ heterostructure.

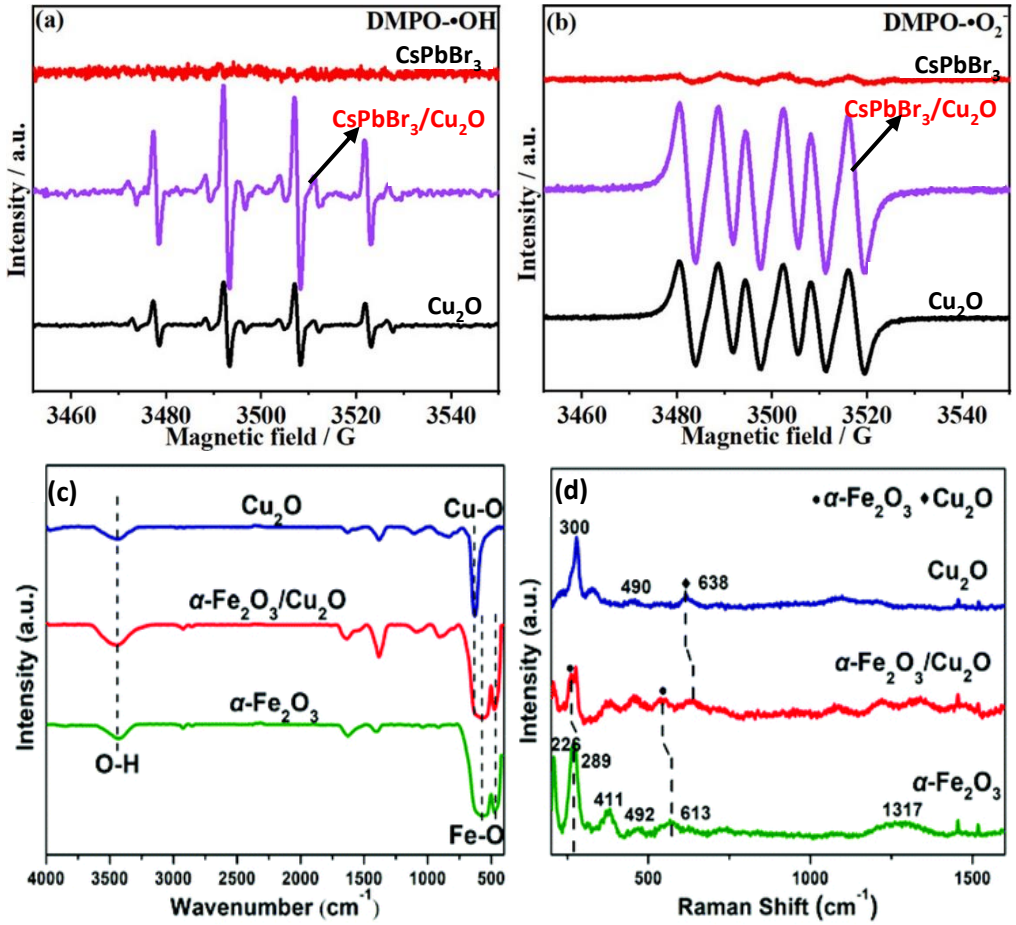

Fig. 10. EPR signals for (a) DMPO-•OH, and (b) DMPO-$\cdot O_2^-$ obtained from $CsPbBr_3$, CuO_2, and $CsPbBr_3/CuO_2$. Adapted with the permission from [54]. Copyright (2022) American Chemical

Society. EPR signals for (c) DMPO-·OH and (d) DMPO-·O_2^- obtained from Fe_2O_3, Cu_2O and α-Fe_2O_3/Cu_2O. Adapted with permission from [44]. Copyright (2022) Royal Society of Chemistry.

EPR spectroscopy was also recently used by Li *et al*. to investigate the S-scheme mechanism in their prepared α-Fe_2O_3/Cu_2O photocatalyst [44]. As shown in **Figure 10c** and **d**, there were no signals in the dark, which suggest that ·OH and ·O_2^- could not be generated in the dark. Upon irradiation, typical signals of DMPO-·OH were observed in the presence of α-Fe_2O_3 and α-Fe_2O_3/Cu_2O (but not in Cu_2O, **Figure 10c)**. In contrast, ·O_2^- was produced by Cu_2O and α-Fe_2O_3/Cu_2O, but not α-Fe_2O_3 (**Figure 10d**). The results show that the photo-induced charge carriers in the α-Fe_2O_3/Cu_2O heterojunction migrated in the S-scheme mode.

3.4. Density Functional Theory Computations (DFT)

DFT is a computational technique commonly used to predict the chemical structure and reactivity of pure and hybridized materials [55]. With DFT calculations, many catalytic materials have been investigated especially in the absence of alternative experimental techniques [56]. Recently, several authors have reported the application of DFT calculation for the characterization of S-scheme photocatalysts. In one of the earliest studies that adopted DFT to identify S-scheme, Wang and co-authors [57] employed DFT calculations to gain more insight into the mechanism of charge transfer in a heterojunction of BiOBr/NiO photocatalyst. As shown in **Figure 11a** and **b** below, the study carefully calculated the electrostatic potentials of individual BiOBr and NiO which revealed surface wave function of 7.0 and 4.6 eV, respectively. As such, the electrons from the NiO will transfer to the BiOBr when the two are in contact up until E_f equilibrium is achieved. **Figure 11c** shows the charge density difference of the BiOBr/NiO heterojunction to illustrate this mechanism. Yellow and cyan, respectively, are used to color the charge accumulation and depletion regions. It is clear that the bridge for electron transmission is formed by the bond between the Br atoms of BiOBr and the Ni atoms of NiO. A compelling reason for why BiOBr/15 wt% NiO composites exhibits efficient charge transfer and high CO_2 photoreduction activity is the intense interaction on the BiOBr/NiO heterojunction interface. The shift of about 0.112e from NiO to BiOBr is measured by Bader charge analysis.

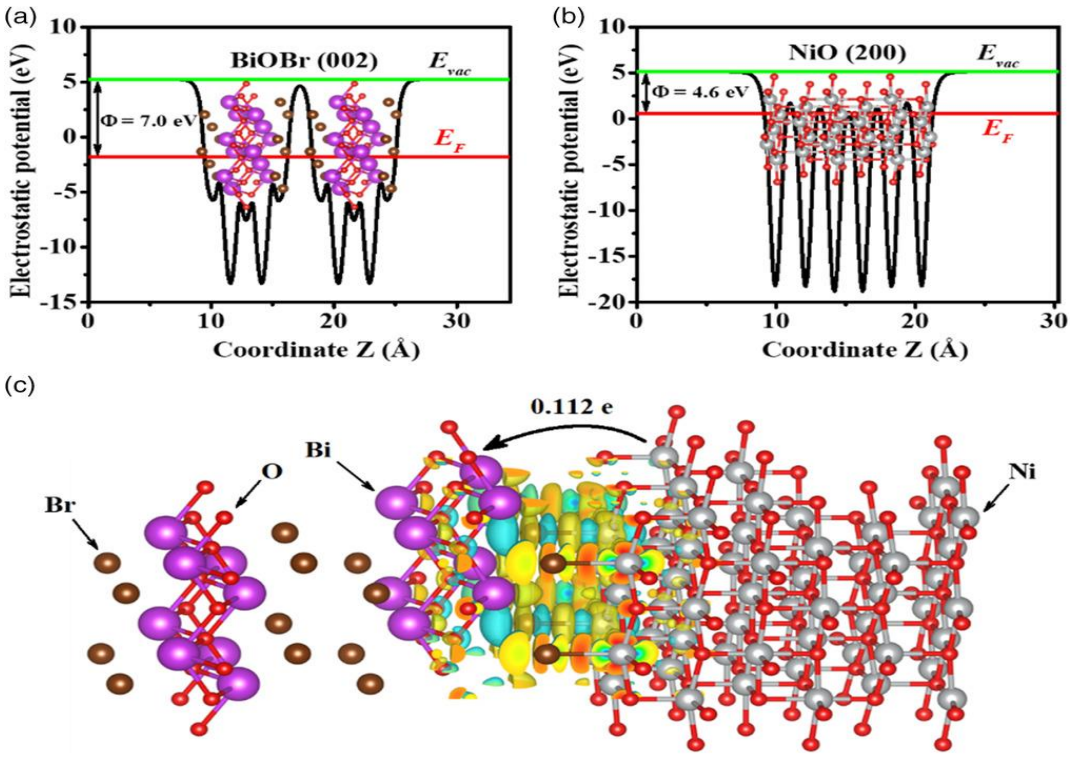

Fig. 11. Electrostatic potentials of (a) BiOBr and (b) NiO, and (c) charge density difference of the BiOBr/NiO heterojunction. Printed with permission from [57]. Copyright 2021, Willet VCH GmbH.

In another recent study, Li and co-workers [58] synthesized a butterfly like 2D/2D carbon nitride (CN)/Zn-doped bismuth vanadium oxide S-scheme photocatalyst and employed DFT to rationalize the mechanism of charge transfer. The variation in charge circulation in **Figure 12** demonstrated the stages of the transfer of electrons, with the yellow and cyan colors denoting the accumulation and depletion of the electrons, respectively. Since pristine CN and ZnBVO possess distinctive work functions, in a CN-ZnBVO-3 heterojunction, the free electrons from CN travel to ZnBVO, creating an electric field at their interface that serves as a catalyst for the transfer of photogenerated electrons from ZnBVO to CN, which leads to charge enhancement on the CN. As a result, from the above, the theoretical findings predicted that photoexcited electrons migrate from the CB of the ZnBVO to the VB of the CN via the interfacial internal electric field and then combine with photogenerated holes in the CN-ZnBVO-3 S-scheme heterojunction. As a result, the powerful electrons that had high reducibility generated in the CB of CN were preserved for the purpose of reducing CO_2.

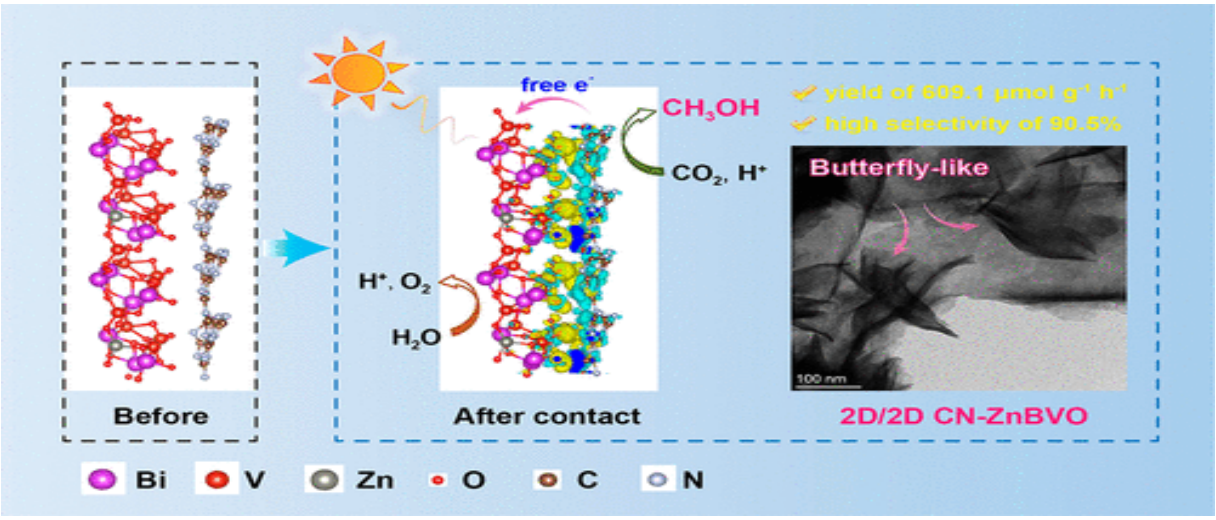

Fig. 12. Charge density difference of carbon nitride and Zn-doped bismuth vanadium oxide. Printed with permission from [58]. Copyright 2023, American Chemical Society.

In a related but recent report, Hua and colleagues [59] designed a highly dispersed MOF-BiOBr/MCS S-scheme nanocomposites and the formation of the heterojunction was confirmed by theoretical calculations based on DFT. Based on the DFT calculations, the work functions of pristine BiOBr and MCS are evaluated to be 7.8 and 4.6 eV, respectively (**Figure 13 a-b**). The DFT results revealed that the E_f of MCS is greater than the E_f of MOF-BiOBr. Simply put, electrons migrated from MCS to MOF-BiOBr as a result of the lower E_f of MOF-BiOBr. Furthermore, **Figure 13 (d–f)** indicates the spatial distribution of the 3D charge density distinction of BiOBr/MCS. The charge density variation demonstrates that MCS and BiOBr are enveloped by cyan and yellow regions, suggesting the transfer of electrons from MCS to BiOBr. It is nevertheless challenging to identify which of the electron density changes are significantly close to the interface between the two materials according to the report. It is important to mention that the planar average charge density variation of BiOBr/MCS is positive for BiOBr and negative for MCS, indicating that MCS loses electrons and BiOBr gains electrons during the formation of BiOBr/MCS interface. A Bader charge assessment was carried out to better understand the charge change and transfer, and the findings demonstrate that roughly 1.8 free electrons migrated from MCS to BiOBr (**Figure 13c)**.

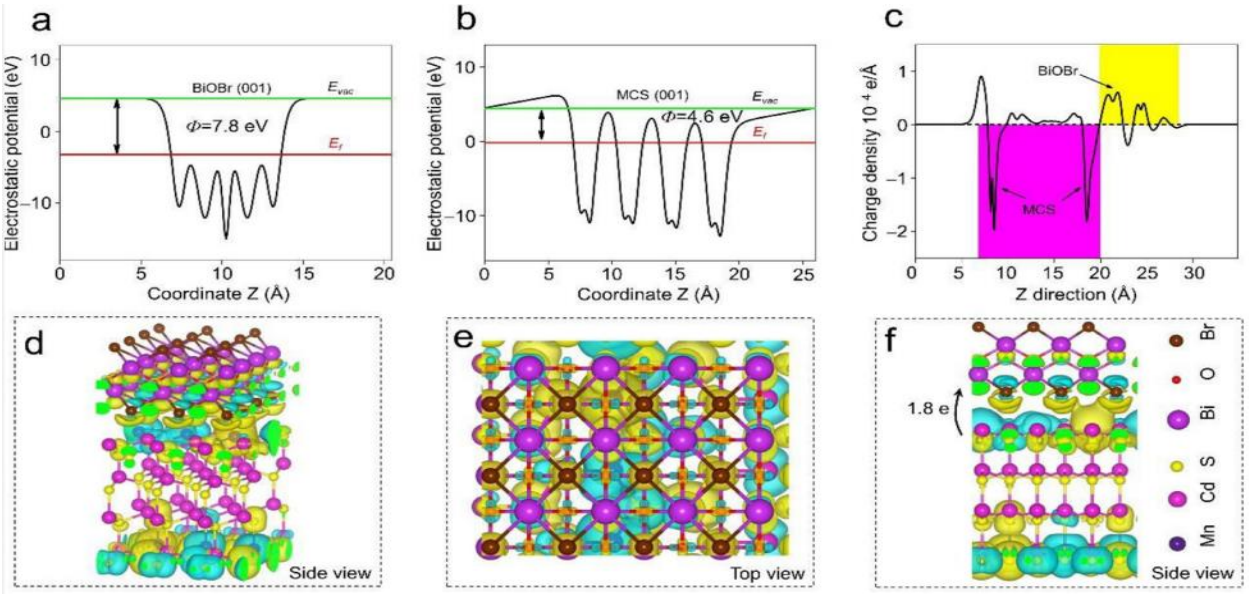

Fig. 13. Work function of the (a) BiOBr (001) and (b) MCS (001) surface. (c) Planar averaged for BiOBr/MCS. (d, f) Side view and (e) top view of the charge density difference of BiOBr/MCS. Printed with permission from [58]. Copyright 2023, Elsevier.

4. Synthesis route of S-scheme photocatalysts

There are multiple considerations to take into account for the successful synthesis of S-scheme photocatalysts. First, the chosen components for synthesis should have different CBs and VBs such that the CB, VB and/or work function of one is higher or lower than the other. Since S-scheme heterojunctions are composed of two semiconducting materials, it is important to couple physiochemically-varied semiconductors to obtain S-scheme of suitably unique physicochemical properties. For example, semiconductor photocatalysts of different interfacial features, morphologies, exposed facets and surface states, should be used for S-scheme synthesis. Further, it is important to factor-in the organization of building blocks, during synthesis so as to obtain heterostructure with a particular and/or unique photocatalytic property for a particular photocatalytic system. To do this, enhanced surface areas for more active sites, increased response to light, improved charge carrier migration and separation and high crystallinity of semiconductor photocatalyst should be considered. As a summary, **Table 1** provides an overview of the advantages and shortcomings of the various synthesis methods discussed in this section for preparing S-scheme photocatalysts.

Table 1: Summarized comparison of various S-scheme photocatalyst synthesis methods.

Method	Shortcomings	Advantages	Interfacial features of the prepared S-scheme heterojunction
Co-precipitation	Time consuming; co-precipitation of impurities; reproducibility issues.	Simple and rapid; low temperature requirement; ability to control the homogeneity.	Enhanced interfacial charge transfer efficiency.
Facile impregnation method	High temperature requirement during calcination.	Development of desirable size and structure.	Improved optical absorption; fast electron channelization; high interfacial contact; prolonged excited state lifetime.
Sol-gel electrospinning method	Long preparation cycle; presence of toxic organic substances in the final product.	Enhanced surface area; simple setup.	Effective and strong interaction coupled with intimate interface.
Hydrothermal/solvothermal method	High pressure and temperature requirements.	Tunable size; improved crystallinity; low-cost; one-pot synthesis; no post annealing.	Strong interaction and intimate interface between the two semiconductors.
Photoreduction method	Lack of size uniformity.	Low toxicity, low-cost and simple.	Excellent interfacial features of the prepared S-scheme nanocomposite.

4.1. Co-precipitation synthesis method

The synthesis of S-scheme photocatalysts via co-precipitation is one of the simplest approaches to prepare a suitable S-scheme heterojunction. The simplicity is characteristically attributed to the mixing of homogeneous chemical reagents at low-temperatures for the synthesis of active metal chalcogenide. S-scheme heterojunctions synthesized via this route are a dried product which usually exhibit high reactivity at low. Jabbar et al. employed the co-precipitation method (**Scheme 1**) to synthesis bare ZIF-8, Ag_2S and ZIF-8/Ag_2S heterostructure nanocomposites for the degradation of organic pollutant [60]. From **Figure 14a**, ZIF-8 revealed a uniform cubic and rhombic dodecahedron crystals with sharp edge from Field emission scanning electron microscopy study [61] while, from **Figure 14b**, Ag_2S showed aggregation of sphere-like particle crystals of 38 nm size [62]. A proof of ZIF-8/Ag_2S synthesis was obtained from the scanning (**Figure 14c**) and transmission (**Figure 14d**) electron microscopies; whereby Ag_2S nanoparticles are dispersed on/around the ZIF-8 with 6–15 nm, as the average size of dispersed Ag_2S. Also, the XRD for the heterostructure revealed there was no shift in the characteristic peaks of both ZIF-8 and Ag_2S, confirming the completeness of the synthesis. The heterostructure ZIF-8/Ag2S was found to have enhanced photodegradation efficiency (100%) as compared with ZIF-8 (51.6%) and Ag_2S (39.7%) at 120 min which was attributed to low e^-—h^+ recombination ZIF-8/Ag_2S.

A facile co-precipitation technique for the synthesis of S-scheme Ag_2CrO_4/$ZnFe_2O_4$ (ACO/ZFO) nanofibers heterojunction was investigated by Yang and coworkers [63]. The ACO/ZFO heterostructure was prepared by loading ACO particles on the surface of ZFO nanofibers to form a nanocomposite. According to XRD of ACO/ZFO, it was shown that the diffraction peak intensity of (031) and (131) corresponding to ACO increases proportionally with an increase in ACO loading from 20–60%. Similar to a previous study [60], it was observed that the ACO particles are uniformly dispersed on the ZFO nanofibers surface from TEM. In terms of band gap measurement, the 40%ACO/ZFO nanocomposite recorded a narrower band-gap, as compared with ACO and ZFO having 1.8 eV and 2.12 eV, respectively. Further, photoluminescence spectroscopy revealed excitation wavelength at 468 nm and an increased intensity as more ACO are loaded. This implies that ZFO/ACO would exhibit reduced charge separation, enhanced electron-hole pairs generation and improved photocatalytic performance [64,65]. A simple schematic diagram for $MeSe_2$/CNT S-scheme photocatalyst synthesis is shown in **Scheme 1.** In summary, the improvements in the overall properties of the S-scheme synthesized via co-

precipitation are expected, by extension, to act as suitable photocatalyst for CO_2 reduction. However, this method suffers from low purity of product, ineffective product dispersion, and low rate of reaction. Hence, the need to explore other feasible methods with fewer drawbacks like the facile impregnation method.

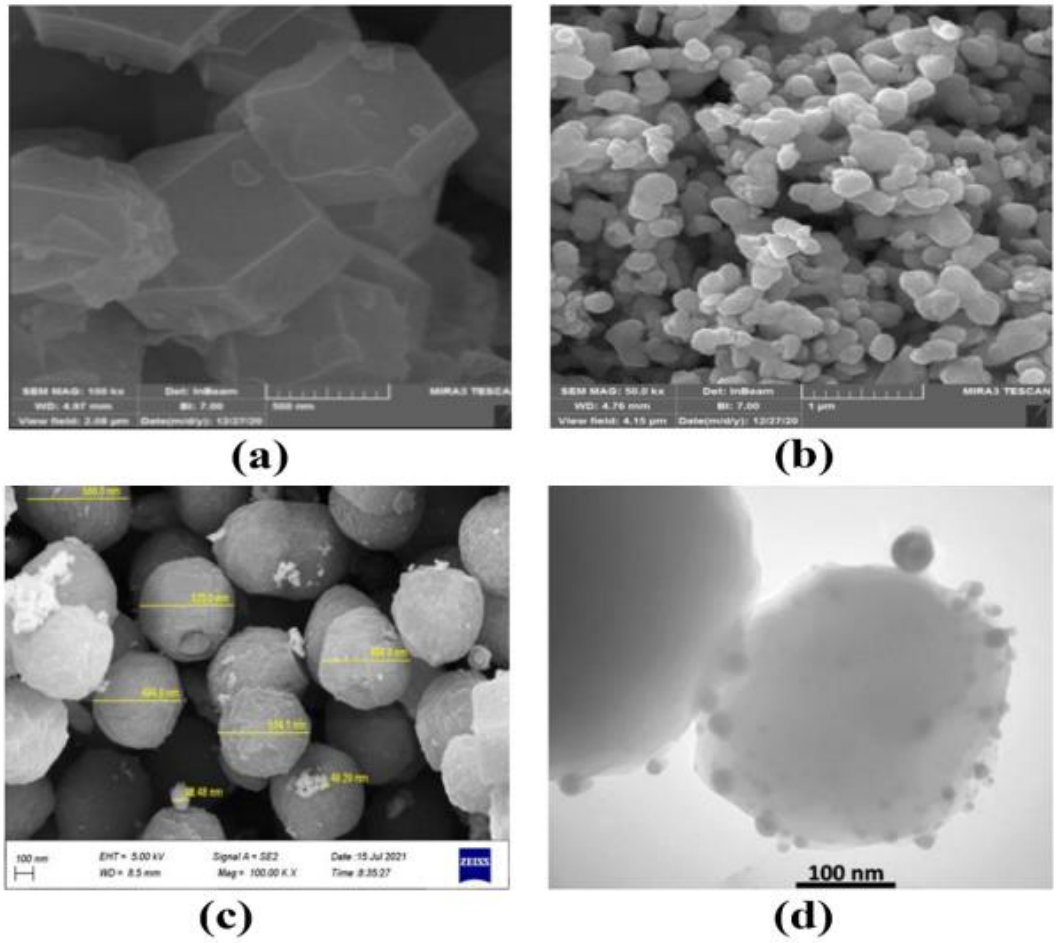

Fig. 12. Field emission scanning electron microscopy images of (a) ZIF-8; (b) Ag2S, (c) ZIF-8/Ag_2S, and (d) TEM of ZIF-8/Ag_2S. Reproduced with permission from Elsevier [60].

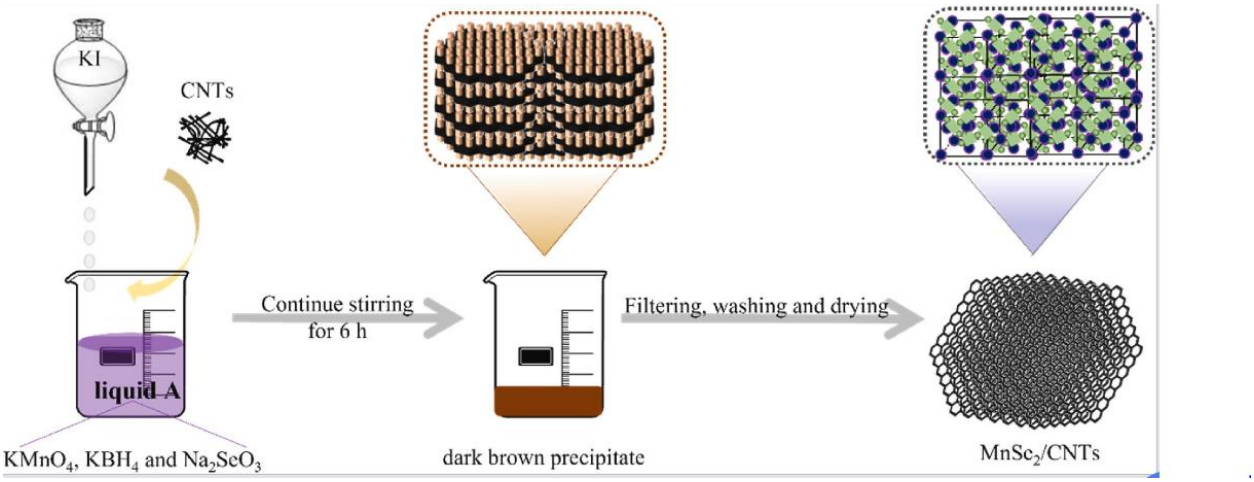

Scheme 1: Schematic co-precipitation method for $MnSe_2$/CNT synthesis. Reproduced with permission from Elsevier [66].

4.2. Facile impregnation synthesis method

This is also known as the evaporative solvent method whereby one precursor is impregnated into another. As an eco-friendly approach, a facile impregnation method can be applied for S-scheme synthesis involving the impregnation of small-sized components onto large-sized materials; and due to solvent involvement, uniformly deposited and/or dispersed composites are commonly obtained. For instance, El-Hosainy and coworkers fabricated an S-scheme heterojunction via a facile impregnation technique [67] where porous ZrO_2 synthesized via Poloxamer P-338 template and then impregnated with NiS nanoparticles at various xNiS concentrations (x = 0.5–2.0 wt %), followed by calcination at 250^{o}C. The synthesis was confirmed with XRD spectra (**Figure 15a**) where there was no change in the intensity and position of diffraction peaks of NiS and ZrO_2, after the addition of the former to the latter. **Figure 15b** indicated that the NiS, ZrO_2 and NiS@ZrO_2 exhibited type IV isotherms with the H3 hysteresis loop category. This means all the samples have porous structures useful for CO_2 adsorption and subsequent reduction upon photocatalyst activation. Moreover, there was a decrease in band energy of ZrO_2 at 2%wt NiS loading from 2.86 eV to 2.32 eV, indicating feasibility of using the S-scheme NiS@ZrO_2 under visible light irradiation. The TEM images of the samples are displayed in **Figure 16 a-c**. In all, the solvent used during the impregnation method for synthesizing S-scheme photocatalysts have several merits like increase porosity, enhanced surface area, and increased rate of reaction. However, it also has some drawbacks such as the presence of impurities, side reactions and a

requirement for controlled reaction conditions. All these limitations affect its use as the best route for s-scheme nanocomposite synthesis.

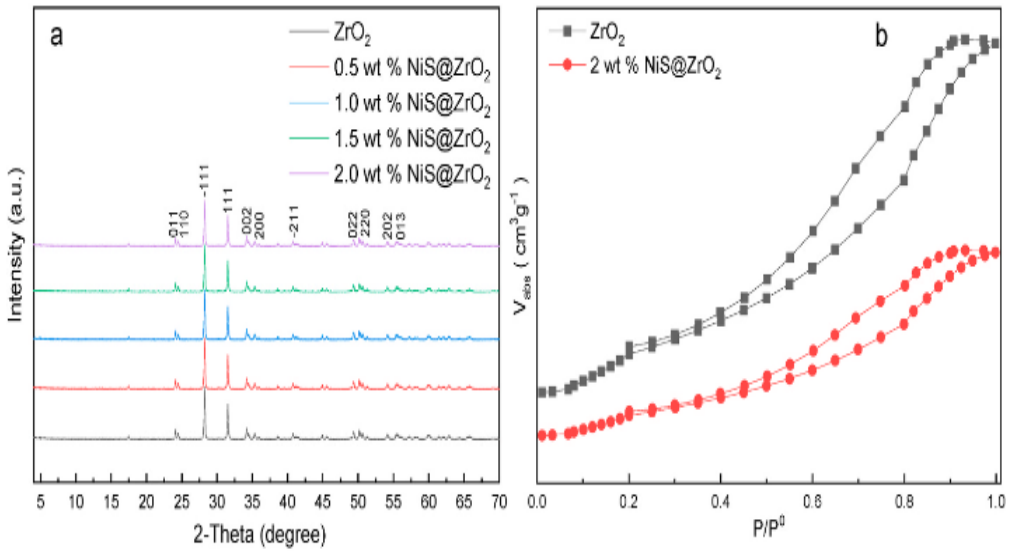

Fig. 15. (a) XRD diffractograms and (b) N_2 adsorption–desorption isotherms of ZrO_2 and NiS@ZrO_2. Reproduced with permission from Elsevier [60].

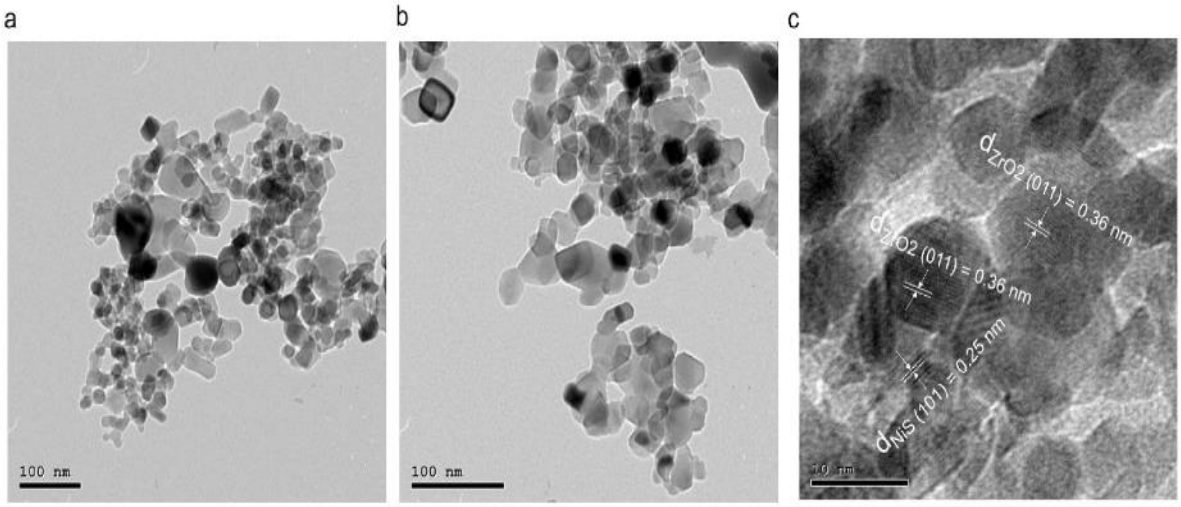

Fig. 16. TEM micrographs of (a) bare ZrO_2, (b) 2 wt % NiS@ZrO_2, and (c) HR-TEM micrograph of 2 wt% NiS@ZrO_2. Reproduced with permission from [60].

4.3. Sol-gel electrospinning synthesis method

The aim behind the use of the sol-gel electrospinning approach is to obtain a high purity nanocomposite with enhanced surface area. This method has also been used for the facile synthesis of robust chromatographic materials, fine thin film powders, and pharmaceuticals. Simply, the technique involves the suspension of previously dried and thermally treated solids in a suitable solvent [27]. Enesa and Isac synthesized an S-scheme $Cu_2S\_TiO_2\_WO_3$ heterostructure using a two-step sol-gel approach [68]. Briefly, Cu_2S was prepared by mixing aqueous solutions of copper nitrate and sodium thiosulfate with continuous stirring. The gel formed was allowed to form a precipitate before drying at 120^oC to obtain powders. The other individual semiconductors (TiO_2 and WO_3) and the final S-scheme heterostructure are prepared using a similar method. According to this study, the $Cu_2S\_TiO_2\_WO_3$ heterostructure revealed compact particles that were close, forming an assembly. During the sol-gel process, it was found that the formation of smaller Cu_2S crystallite size was favored by the presence of TiO_2. On the other hand, the presence of WO_3 enhances the size of Cu_2S crystallite formation. Thus, individual metal oxide often exhibits different nucleation roles during Cu_2S synthesis [69,70]. From **Figure 17**, it can be seen that the S-scheme heterostructure has a narrower band gap than the individual metal oxide and thus, the ability to absorb a broader spectrum of light (e.g., visible, ultraviolet and infrared) [71,72]. Further, when compared to the individual metal oxide or two-component heterostructure, the three-component heterostructure has enhanced photocatalytic efficiency (61%). In the three-component heterostructure, slower charge recombination and more spectra absorption might account for the improved photocatalytic efficiency.

Another example is a TiO_2/g-C_3N_4 S-scheme heterojunction that was synthesized using a one step sol-gel method [73]. A known volume of anhydrous ethanol and tetraethyl titanate was mixed, followed by the addition of urea. Distilled water and concentrated hydrochloric acid were added, and the mixture was allowed to stand for 12 h to form a sol-gel. This sol-gel was later dried at 80^oC and calcined at 550^oC. The pore size, volume and specific surface area of the TiO_2/U5-g-C_3N_4 S-scheme heterostructure were greater than bare TiO_2 and TiO_2/U5-g-C_3N_4. An increase in the urea and g-C_3N_4 content led to more carbon dioxide and ammonia gas liberation [74] during the calcination process as the urea thermally polymerized. Hence, the passivation of the S-scheme heterojunction by the gas bubbles proportionally created pores of enhanced size, area, and volume. By inference, it leads to improved charge carrier separation, and improved

photocatalytic activity. It is worth mentioning that the sol-gel method finds its merits in having a broad range of temperatures for synthesis, optimization and controlled morphology [75].

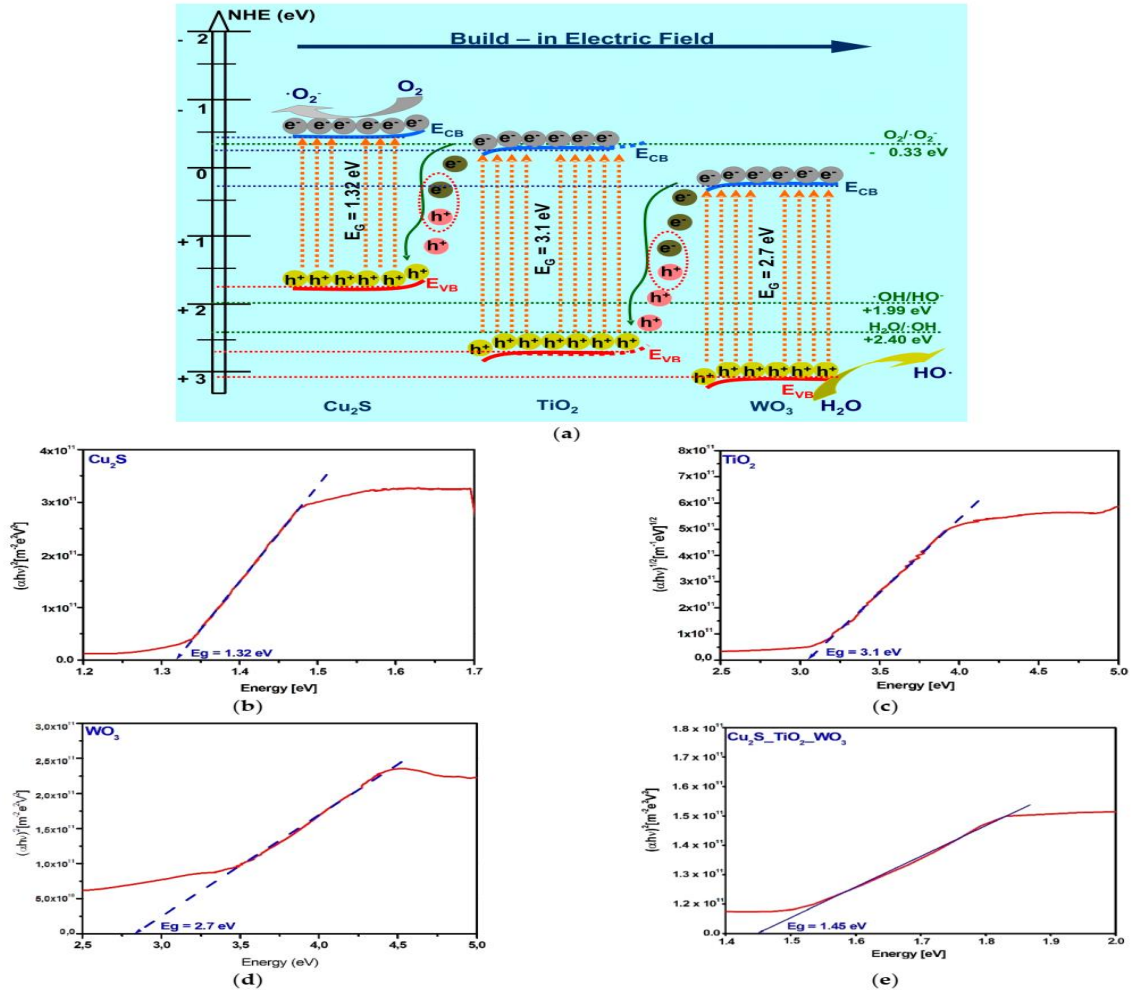

Fig. 17. (a) Schematic diagram of band energy S-scheme $Cu_2S\_TiO_2\_WO_3$ heterostructure and the respective band gaps of (b) Cu_2S, (c) TiO_2, (d) WO_3, and (e) $Cu_2S\_TiO_2\_WO_3$. Reproduced with permission from [68].

4.4. Solvothermal/hydrothermal synthesis method

In this method, powders of the S-scheme photocatalyst are obtained by crystalizing metal oxides at high pressure and temperature in a steel autoclave, as shown in **Scheme 2**. As a merit, an interface is produced which enhanced the surface area of the S-scheme heterojunction synthesized. Tayyab and coworkers synthesized ternary $In_2S_3/Nb_2O_5/Nb_2C$ Schottky/S-scheme for hydrogen production via a one-pot *in-situ* hydrothermal method [76]. In this process, sol-gel

is not allowed to form nor is the mixture dried, rather the metal oxides needed to form the S-scheme are suspended in ultrapure water, ultrasonicated for dispersion and then crystallized in an autoclave at optimum temperature. In this study, Nb_2O_5/Nb_2C (NNC), pure In_2S_3 and the ternary $In_2S_3/Nb_2O_5/Nb_2C$ synthesis were carried out by autoclaving at 463.15 K. **Figure 18** shows the SEM images of Nb_2AlC, Nb_2C MXene, NNC and INNC-2, respectively. According to the SEM analysis (**Figure 18a**), it could be confirmed that Nb_2AlC has a compact structure; after treatment with HF solution, the accordion-type MXene is obtained [77]. Further, a nanorod-shaped morphology of Nb_2C MXene (**Figure 18b**) was formed as a result of anchoring Nb_2O_5 nanorods on its surface, as aided by the presence of fluoride ions [78]. The presence of Nb, O, and C, together with F shows that fluoride ion is attached to MXene and thus, serves as a template for nanorod Nb_2O_5 formation [78]. Clearly, this indicated the actual conversion of Nb_2C MXene to Nb_2O_5/Nb_2C by the hydrothermal method, for which the EDS spectra are presented in **Figure 18 (e-g).** Moreover, the ternary $In_2S_3/Nb_2O_5/Nb_2C$ achieved hydrogen production efficiency at the ternary $In_2S_3/Nb_2O_5/Nb_2C$, which is about 7.5 and 11 times more than bare In_2S_3 and two-component Nb_2O_5/Nb_2C (NNC) photocatalysts, correspondingly.

Bahadoran and coworkers studied the two-step hydrothermal process to load CeO_2 onto 3D hierarchical WO_3 with band gaps of 2.81 eV and 2.74 eV, respectively [79]. The photocatalytic activity of WO_3/CeO_2 (E_f = 2.68 eV) S-scheme heterostructure nanocomposite was improved as compared to bare WO_3 and CeO_2 samples. With a CeO_2 content of 30 mol.%, a 100 % sulfamerazine degradation was achieved. The formation of oxygen vacancies at the interface connecting the two metal oxides was reported, which further improved the charge carrier separation in the WO_3/CeO_2 S-scheme. Throughout the hydrothermal process of preparing the S-scheme, it was revealed that there was retainment of the hollow, spherical and hierarchical structure of WO_3 following the addition of CeO_2.

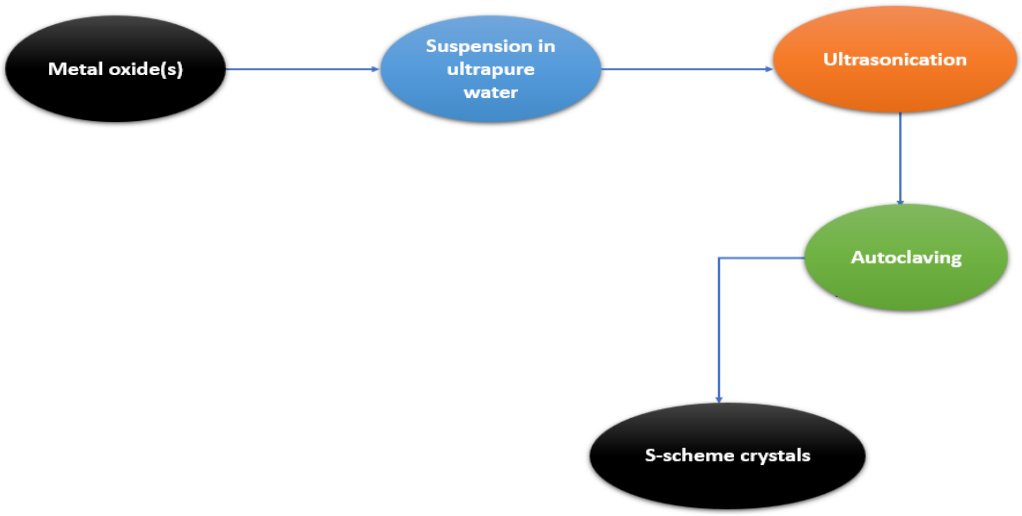

Scheme 2. Schematic representation of the hydrothermal synthesis procedure.

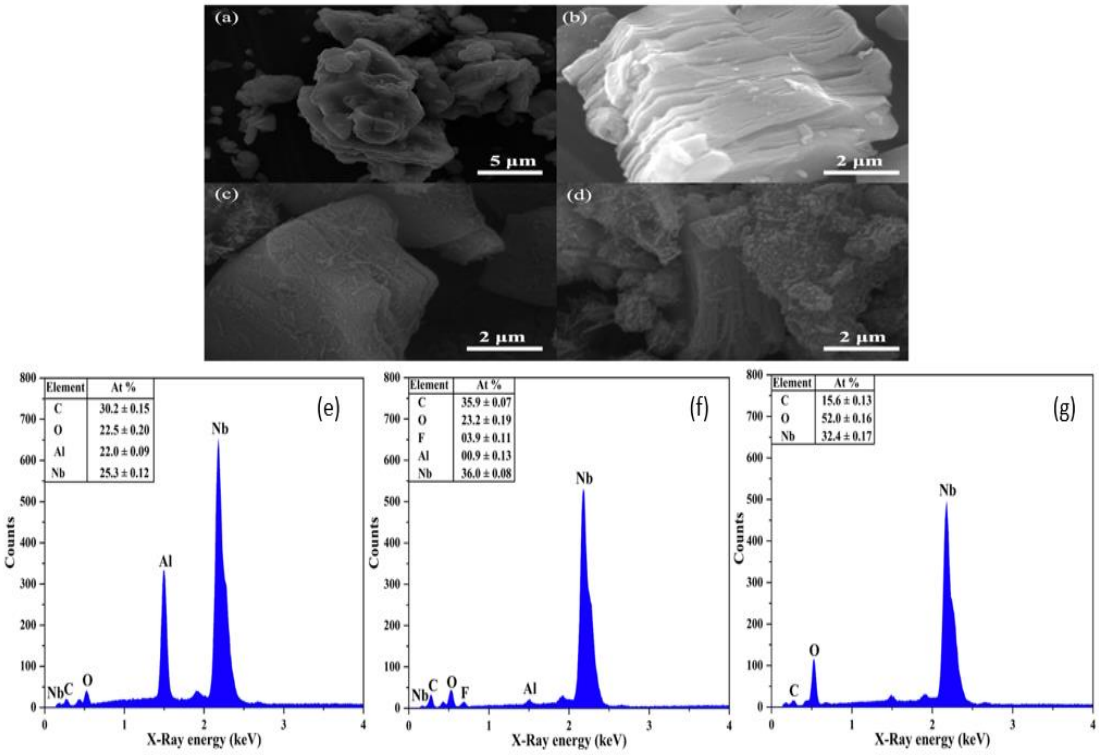

Fig. 18. SEM micrographs of (a) Nb_2AlC, (b) Nb_2C MXene, (c) NNC, and (d) INNC-2. EDS spectra of (e) Nb_2AlC, (f) Nb_2C MXene, and (g) NNC. Reprinted with permission from [76].

4.5 Photoreduction synthetic method

The photoreduction method, also known as the photo-deposition method, is a method in which one semiconductor is deposited on another through photoreduction. In this method, electrons are photogenerated by one of the semiconductors upon irradiation. The electrons generated therefore reduce ions adsorbed on the surface of the semiconductor to produce another semiconductor that is deposited on the surface of the main semiconductor. This route of S-scheme synthesis is preferred because it has lower toxicity and is more cost-effective.

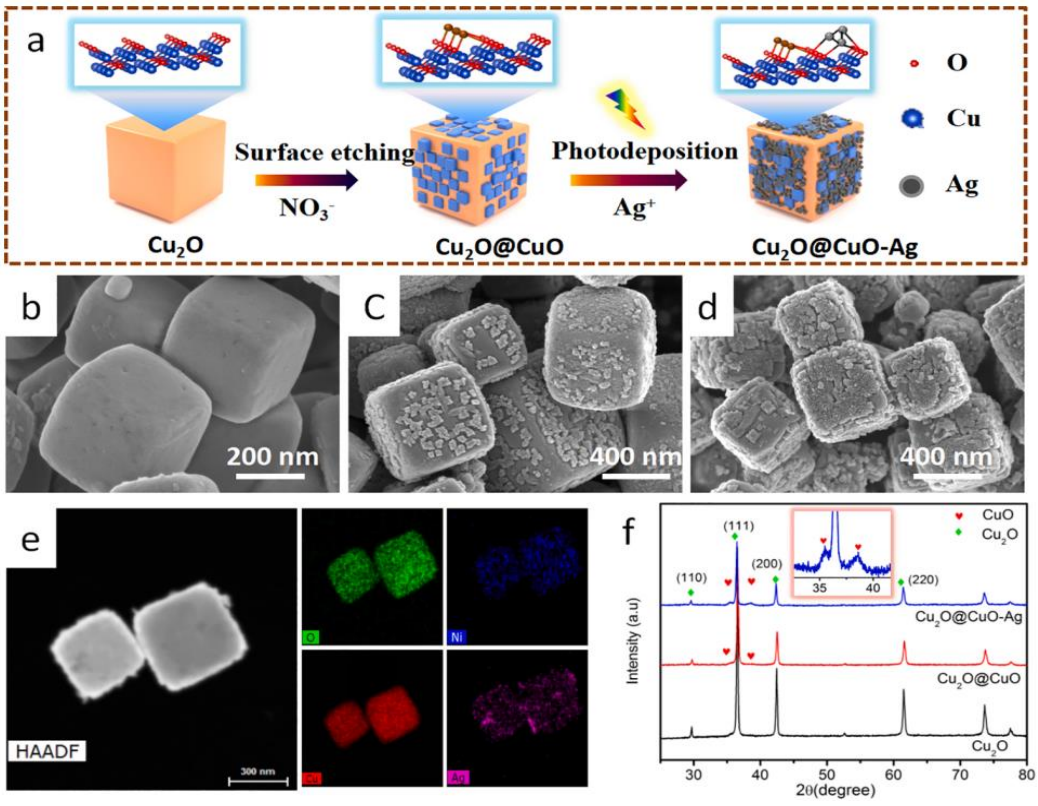

Fig. 19. (a) Synthesis procedure of the Cu_2O@CuO-Ag. (b) SEM of Cu_2O, (c) Cu_2O@CuO, and (d) Cu_2O@CuO-Ag. (e) EDS mapping micrographs of Cu_2O@CuO-Ag. (f) XRD patterns of as-prepared samples. Reprinted with permission from [80].

Li and his group employed photodeposition and surface etching to synthesize core-shell Cu_2O@CuO-Ag with S-scheme heterojunction as a highly efficient photocatalysis [80]. As displayed in **Figure 19b, c and d,** the sample surfaces of Cu_2O change from smooth to granular for Cu_2O@CuO and later to pit for Cu2O@CuO-Ag because of etching and photoreduction, respectively. The EDS results (**Figure 19e**) show that silver (Ag) displayed a bright distribution, and that nickel (Ni) is faintly light. By implication, this implies that more of Ag and less of Ni

are deposited on Cu2O@CuO-Ag. Crytal plane peaks of (110), (111), (200) and (220) were correlated to the four distinct peaks at 29.7◦, 36.5◦, 42.4◦ and 61.4◦, as shown in **Figure 19f.** From this, it can be deduced that the etching of $Ni(NO_3)_2{\cdot}6H_2O$ salt did not produce any new peak and therefore has no effect on the bulk crystalline property of the salt. For Ag, there was no appearance of a new peak for Ag, and this is attributed to less Ag being formed on Cu_2O@CuO surface. Although this method has benefits, the non-uniformity particle size resulting from photo-deposition is a general drawback.

5. Emerging application of Scheme photocatalysts in CO_2 reduction

The application of S-scheme photocatalysts is gaining momentum and research efforts are being carried out to improve the charge transfer and powerful redox potential of S-scheme photocatalysts towards the transformation of CO_2. A wide range of semiconductors has been reported, which include n-type semiconductors (e.g., TiO_2, ZnS, C_3N_4, MoO_3, In_2O_3, CeO_2, AgBr, ZnO, CdS, GaAs, Ta_2O_5, $BiVO_4$ and CdSe), which have large numbers of free electrons and negative charge carriers [81–84], and p-type semiconductors (e.g., PbS, Co_3O_4, $GaLnP_2$, MoS_2, NiS, Cu_2O, and NiO), which have a majority of its charge carries as positive holes [85–88]. Generally, n-type semiconductors are more stable than p-type semiconductors and have higher conductivity [89–91]. Semiconductor heterojunctions are divided majorly into n–n junctions, p–p junctions, and p–n junctions [92,93].

5.1. n-n heterojunctions

n-n type heterojunctions, are formed when n-type semiconductors with different electron affinity are brought in contact, thus enabling the charge transfer between the semiconductors when the Fermi levels reach the same energy level, with several n-type semiconductors having limited absorption in the visible light range. Yu et al. [94] proved that typical n-n heterojunctions in Bi_2MoO_6-SOVs/In_2S_3 (surface oxygen vacancies) offered intrinsic conductivity when in close contact. The photocatalytic CO_2 reduction activity of n-type (In_2S_3) and n-type (Bi_2MoO_6) semiconductors are much lower than Bi_2MoO_6-SOVs/In_2S_3 (**Table 2**, item 1, Bi_2MoO_6 (CO – 3.67 $\mu molg^{-1}h^{-1}$), In_2S_3 (CO – 4.31 $\mu molg^{-1}h^{-1}$) and Bi_2MoO_6/In_2S_3 (CO – 28.54 $\mu molg^{-1}h^{-1}$)). The observed interface potential difference, from In_2S_3 to Bi_2MoO_6-SOVs, accelerates the separation and transfer of photogenerated charges, thus preventing recombination of electrons

from the CB of In_2S_3 to the CB of Bi_2MoO_6-SOVs [81]. This leads to increased activity observed for Bi_2MoO_6-SOVs/In_2S_3. When Bi_2MoO_6-SOVs/In_2S_3 is irradiated by visible light, both the energy band edge of In_2S_3 (semiconductor losing electrons) and Bi_2MoO_6-SOVs (semiconductor gaining electrons) will bend to allow VB electrons of Bi_2MoO_6-SOVs and In_2S_3 to jump to their CBs leading to the S-scheme charge transfer mechanistic route (**Figure 20**).

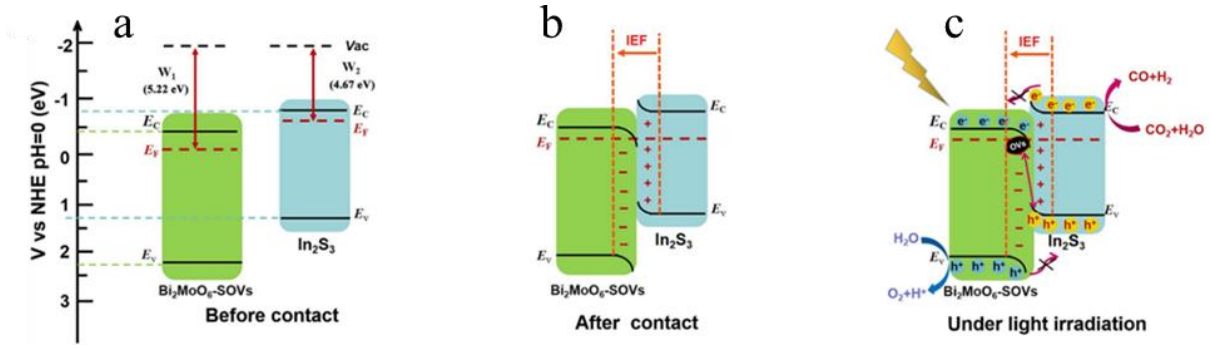

Fig. 20. Schematic illustration for photocatalytic CO_2 reduction over the Bi_2MoO_6-SOVs@In_2S_3 heterojunction. (a) Band position before contact, S-scheme charge transfer mechanism (b) after contact and (c) under visible-light radiation. Printed with permission from [94]. Copyright 2022, Elsevier.

In another study, a ZnS and ZnO semiconductor exhibited CO_2 photoreduction to form CH_3OH (126 and 127.8 $\mu molg^{-1}$), respectively after 9 h illumination (**Table 2**, item 2) [95]. The use of the Pt/ZnS@ZnO heterostructure exhibited a significant increase in CO_2 photoreduction to form CH_3OH (1,402 $\mu molg^{-1}$) after 9 h of sunlight [95]. The interface contact among Pt (the co-catalyst), ZnS and ZnO improved charge transportation and separation, thus, decreasing the nanocomposite's band gap (**Table 2**, item 2) [95]. Owing to the wide band gap of g-C_3N_4 and cubic bixbyite (C-In_2O_3) (**Table 2**, item 3), both respond to ultraviolet light, thus generating electrons and holes that aggregate on the CB and VB [96]. Both g-C_3N_4 and C-In_2O_3 presented considerable CO_2 photoreduction properties, with g-C_3N_4 (CO – 24.95 $\mu molg^{-1}h^{-1}$, CH_4 – 11.67 $\mu molg^{-1}h^{-1}$) and C-In_2O_3 (CO – 75.86 $\mu molg^{-1}h^{-1}$, CH_4 – 55.76 $\mu molg^{-1}h^{-1}$). The formation of the p-n junction between In_2O_3 and g-C_3N_4, (In_2O_3/g-C_3N_4) gave excellent photocatalytic activity (**Figure 21**). The simultaneous transfer of carriers could have contributed to the narrower band gap of In_2O_3/g-C_3N_4 when compared to g-C_3N_4 and C-In_2O_3. This was influenced by the migration of photoinduced electrons (from CB of g-C_3N_4 to CB of In_2O_3) and holes (from VB of

In_2O_3 to VB of g-C_3N_4) which improve the charge separation efficiency and suppress recombination of electron-hole pairs and enlarge the light response range under light irradiation.

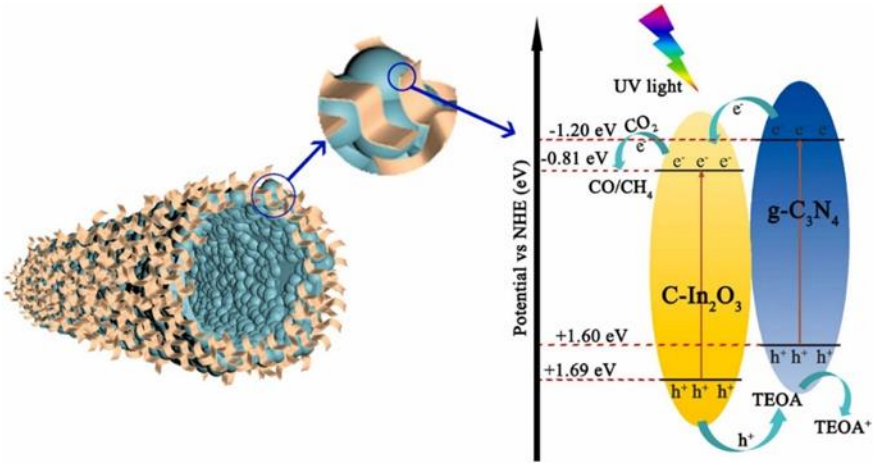

Fig. 21. Schematic illustration of band position, charge transfer process and photocatalytic mechanism of CO_2 reduction. Printed with permission from [96]. Copyright 2021, Elsevier.

Wang et al. synthesized a $La_2Ti_2O_7/Ti_3C_2$ visible light photocatalyst by depositing $La_2Ti_2O_7$ nanoparticles onto Ti_3C_2 [97]. Their results show that the $La_2Ti_2O_7/Ti_3C_2$ heterostructured photocatalyst had enhanced activity (CO – 14.78 $\mu molg^{-1}h^{-1}$ and CH_4 – 11.16 $\mu molg^{-1}h^{-1}$) compared to unsupported $La_2Ti_2O_7$ (CO – 14.78 $\mu molg^{-1}h^{-1}$ and CH_4 – 11.16 $\mu molg^{-1}h^{-1}$) (**Table 2**, item 4). The enhanced activity was due to the free flow of photo-excited electrons from the conduction band of LTO ($La_2Ti_2O_7$) to Ti_3C_2.

Meng et al. [98] fabricated a series of polydopamine-modified TiO_2 (TiO_2@PDA) hollow spheres and investigated the effect of PDA wrapping on the photocatalytic CO_2 reduction activities of TiO_2. From the reported data, TiO_2@PDA photocatalysts presented the highest value of methane yield, which was 5 times more than that of TiO_2. To understand the role of PDA in enhancing photoactivity, the charge transfer mechanism was proposed in **Figure 22**. The band gap of anatase TiO_2 and PDA was 3.2 and 1.6 eV, respectively with PDA contributing to the extension of visible light adsorption (**Table 2**, item 5). According to the study, photogenerated electrons of TiO_2 move to PDA while photogenerated holes of PDA transfer to the VB of TiO_2 (**Figure 22**), this leads to effective charge-hole separation, with inhibited charge recombination.

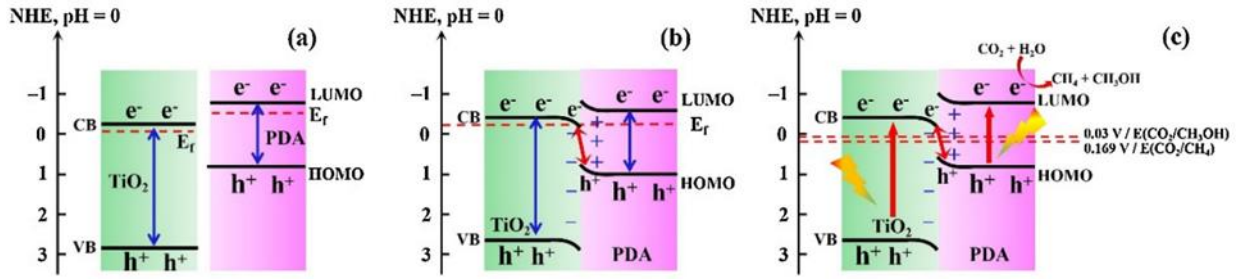

Fig. 22. Schematic illustration of the relative band energy positions of TiO_2 and PDA before contact (a), after contact, (b) and under irradiation. (c) The S-scheme charge transfer mechanism between TiO_2 and PDA under irradiation. Printed with permission from [98]. Copyright 2021, Elsevier.

Additional studies [99–103][40,104–108][109–114] have shown that interfacing n-type to n-type semiconductors with different electron affinities effectively improves the charge separation and photocatalytic performance by shifting its Fermi level depending on the relative VB and CB position of both semiconductors. As can be seen from **Table 2**, several semiconductors, $InVO_4$/g-C_3N_4 [99], p-C_3N_4/$InVO_4$ [100], 2D/2D/0D TiO_2/C_3N_4/Ti_3C_2 [101], O-doped g-C_3N_4/N-doped Nb_2O_5 [102], g-C_3N_4@CeO_2 [103], ZnS@$ZnIn_2S_4$ [104], TiO_2/$CsPbBr_3$ [40], CdS/TiO_2 [105], Pt@CeO_2/3D g-C_3N_4 [106], g-C_3N_4/$ZnIn_2S_4$ [107], g-C_3N_4/COF [108], CdSe/CN [109], g-C_3N_4/(Cu/TiO_2) [110], $CsPbBr_3$@mesoporous TiO_2 beads [111], $BiVO_4$/$CsPbBr_3$ [112], In_2S_3/MoO_3@MoS_2 [113], and 2D/2D g-C_3N_4/MoS_2 [114] exhibited excellent visible-light CO_2 reduction compared to the individual semiconductors. These enhanced photocatalytic activities were attributed to large surface areas [103], charge-hole separation and extended visible-light absorption. This is because at the n–n junction, free electrons and holes diffuse until equilibrium is reached, consequently leaving negative and positive regions at the heterojunction interface. Generally, n-type semiconductors offer several advantages such as a broader range of materials which allows for the optimization of photocatalytic properties such as improved electron mobility which enables efficient charge transport and reduced electron-hole recombination. TiO_2 based semiconductors [35, 110] are known to present excellent stability and resistance to photocorrosion. The semiconductors are suitable for long-term photocatalytic reduction applications. However, achieving favorable energy band alignment between different n-type semiconductors can be very challenging, and improper band alignment may hinder charge

transfer processes. In addition, the weak potential of n-n heterojunctions results in lower charge separation efficiency and possibly higher recombination rates.

Table 2. A summary of works using n-n S-scheme heterojunctions for CO_2 reduction.

Number	**Catalyst**	**Oxidation site**	**Reduction site**	**Bandgap energies (eV)**	**Photocatalytic activity ($\mu molg^{-1}h^{-1}$)**	**Ref.**
1	Bi_2MoO_6/ln_2S_3	Bi_2MoO_6	ln_2S_3	Bi_2MoO_6 – 2.68 In_2S_3 – 2.16	*Bi_2MoO_6* CO – 3.67 *In_2S_3* CO – 4.31 *Bi_2MoO_6/ln_2S_3* CO – 28.54	[94]
2	Pt/ZnS@ZnO	Pt	ZnS@ZnO	ZnO – 3.21 ZnS@ZnO – 3.11 Pt/ZnS@ZnO – 2.11	*ZnO* CH_3OH – 126 (9 h) *ZnS@ZnO* CH_3OH – 127.8 (9 h) *Pt/ZnS@ZnO* CH_3OH – ~1402 (9 h)	[95]
3	MIL-68 derived C-In_2O_3/g-C_3N_4	g-C_3N_4	C-In_2O_3	g-C_3N_4 – 2.72 C-In_2O_3 – 2.51 C-In_2O_3/g-	*MIL-67* CO – 24.95 CH_4 – 11.67 *C-In_2O_3*	[96]

				C_3N_4 – 2.67	CO – 75.86 CH_4 – 55.76	
4	$La_2Ti_2O_7/Ti_3C_2$	$La_2Ti_2O_7$	Ti_3C_2	$La_2Ti_2O_7$ – 3.73	*C-In_2O_3/g-C_3N_4* CO – 153.42 CH_4 – 110.31 *$La_2Ti_2O_7$* CO – 2.57 CH_4 – 0.27	[97]
5	TiO_2/polydopamine (PDA)	TiO_2	PDA	TiO_2 – 3.2 PDA – 1.6	*$La_2Ti_2O_7/Ti_3C_2$* CO – 14.78 CH_4 – 11.16 *TiO_2* CH_4 – 0.30 CH_3OH – 0.63	[98]
6	$InVO_4$/g-C_3N_4	g-C_3N_4	$InVO_4$	$InVO_4$ – 2.02 g-C_3N_4 – 2.70 $InVO_4$/g-C_3N_4 – 1.81	*TiO_2/PDA* CH_4 – 1.50 CH_3OH – 0.26 *$InVO_4$* CH_4 – 9.02 CO – 26.92 *g-C_3N_4* CO – 3.83	[99]
7	p-C_3N_4/$InVO_4$	p-C_3N_4	$InVO_4$	p-C_3N_4 – 2.74 $InVO_4$ – 2.17	*$InVO_4$/g-C_3N_4* CO – 69.8 *p-C_3N_4/$InVO_4$* CO – 5.43	[100]

					p-C_3N_4/$InVO_4$ CO – 14.05	
8	2D/2D TiO_2/C_3N_4/Ti_3C_2	TiO_2	Ti_3C_2	TiO_2 – 2.66 C_3N_4 – 1.81	*TiO_2/C_3N_4* CO – 3.14 *TiO_2/C_3N_4/Ti_3C_2* CO – 4.39 CH_4 – 1.20	[101]
9	O-doped g-C_3N_4/N-doped Nb_2O_5	N-doped Nb_2O_5	O-doped g-C_3N_4	O-doped g-C_3N_4 – 2.71 N-doped Nb_2O_5 – 2.91 O-doped g-C_3N_4/N-doped Nb_2O_5 – 2.81	*O-doped g-C_3N_4* CO – 56.78 CH_4 – 7.67 *N-doped Nb_2O_5* CO – 2.75 CH_4 – 20.69 *O-doped g-C_3N_4/N-doped Nb_2O_5* CO – 253.34 CH_4 – 68.11	[102]
10	g-C_3N_4@CeO_2	CeO_2	C_3N_4	C_3N_4 – 2.70 CeO_2 – 2.93	*g-C_3N_4* CH_4 – 1.8 CH_3OH – 3.1 *CeO_2* CO – 5.3 CH_3OH – 3.3 *g-C_3N_4@CeO_2*	[103]

					CH_4 – 3.5 CH_3OH – 5.2 CO – 16.8	
11	$ZnS@ZnIn_2S_4$	ZnS	$ZnIn_2S_4$	ZnS – 3.49 $ZnIn_2S_4$ – 2.50 $ZnS@ZnIn_2S_4$ – 2.65	*$ZnIn_2S_4$* CO – 25.99 CH_4 – 0.90 *$ZnS@ZnIn_2S_4$* CO – 87.43	[104]
12	$TiO_2/CsPbBr_3$	TiO_2	$CsPbBr_3$	TiO_2 – 3.10 $CsPbBr_3$ – 2.24	*TiO_2* CO – 4.68 *$TiO_2/CsPbBr_3$* CO – 9.02	[40]
13	CdS/TiO_2	TiO_2	CdS	CdS – 2.27 TiO_2 – 3.04	*CdS* CO – 4.59 CH_4 – 0.19 CH_3OH – 2.22 *TiO_2* CO – 2.26 CH_4 – 5.80 CH_3OH – 0.24 *CdS/TiO_2* CH_4 – 27.85	[105]
14	$Pt@CeO_2$/3D g-C_3N_4	Pt	CeO_2/3D g-C_3N_4	3D g-C_3N_4 – 2.61 CeO_2/3D g-C_3N_4 – 2.50 $Pt@CeO_2$/3D g-C_3N_4 – 2.48	*3D g-C_3N_4* CO – 0.89 CH_4 – 0.69 *CeO_2/3D g-C_3N_4* CO – 4.69	[106]

					CH_4 – 3.03	
15	g-C_3N_4/$ZnIn_2S_4$	g-C_3N_4	$ZnIn_2S_4$	g-C_3N_4 – 2.82 $ZnIn_2S_4$ – 2.41	*g-C_3N_4/$ZnIn_2S_4$* CO – 1453 H_2 – 863	[107]
16	g-C_3N_4/COF	g-C_3N_4	COF	g-C_3N_4 – 2.50 COF – 1.68	*g-C_3N_4* CO – 3.5 *g-C_3N_4/COF* CO – 11.25	[108]
17	CdSe/CN	CN	CdSe	CdSe – 2.38 CN – 2.74 CdSe/CN – 2.67	*CdSe* H_2 – 1.2 *CN* H_2 – 5.1 *CdSe/CN* H_2– 20.1	[109]
18	g-C_3N_4/(Cu/TiO_2)	g-C_3N_4	Cu/TiO_2	g-C_3N_4 – 2.74 TiO_2 – 3.1 g-C_3N_4/(Cu/TiO_2) – 2.38	*g-C_3N_4/(Cu/TiO_2)* CH_3OH – 2574 µmol/g.cat HCOOH – 5069 µmol/g.cat	[110]
19	$CsPbBr_3$@mesoporous TiO_2 beads	TiO_2	$CsPbBr_3$	$CsPbBr_3$ – 2.30 mesoporous TiO_2 beads – 3.10	*$CsPbBr_3$* CO – 41.65 *mesoporous TiO_2 beads* CO – 31.32 *$CsPbBr_3$@mesoporous TiO_2 beads*	[111]

					CO – 145.25	
30	$BiVO_4/CsPbBr_3$	$BiVO_4$	$CsPbBr_3$	$BiVO_4$ – 2.42 $CsPbBr_3$ – 2.31	*$BiVO_4$* CO – 22.42 (4 h) *$CsPbBr_3$* CO – 41.90 (4 h) *$BiVO_4/CsPbBr_3$* CO – 103.5 (4 h)	[112]
31	$In_2S_3/MoO_3@MoS_2$	MoS_3	$MoO_3@MoS_2$	MoS_3 – 2.81 $MoO_3@MoS_2$ – 2.50	*$MoO_3@MoS_2$* CH_4 – 15.75 CO – 22.26 *$In_2S_3/MoO_3@MoS_2$* CH_4 – 49.11 CO – 6.19	[113]
32	2D/2D g-C_3N_4/MoS_2	2D/2D g-C_3N_4	MoS_2	2D/2D g-C_3N_4/MoS_2	*g-C_3N_4* CO – 11 CH_4 – 15 *MoS_2* CO – 1.96 CH_4 – 3.9 *2D/2D g-C_3N_4/MoS_2* CO – 146.7	[114]
33	$TiO_2@In_2Se_3@Ag_3PO_4$	In_2Se_3	Ag_3PO_4	TiO_2 – 3.10 In_2Se_3 – 2.30 Ag_3PO_4 – 1.78	*$TiO_2@Ag_3PO_4$* CH_4 – 2.58 CH_3OH – 3.87	[115]

					CO – 5.03 *TiO_2@In_2Se_3* CH_4 – 2.72 CH_3OH – 4.03 CO – 5.52 *TiO_2@In_2Se_3@Ag_3PO_4* CH_4 – 3.98 CH_3OH – 4.32 CO – 8.2	
34	2D/3D g-C_3N_4/ZnO	ZnO	g-C_3N_4	g-C_3N_4 – 2.6 ZnO – 3.1 g-C_3N_4/ZnO – 2.5	*g-C_3N_4/ZnO* CH_4 – 16	[116]
35	$LaNiO_3$/$CdLa_2S_4$			$LaNiO_3$ – 1.66 $CdLa_2S_4$ – 2.28	*$LaNiO_3$/$CdLa_2S_4$* CO – 10 243	[117]
36	Fe_3N/Fe_2O_3/C_3N_4	C_3N_4	Fe_3N/Fe_2O_3	C_3N_4 – 2.79 Fe_3N/Fe_2O_3/C_3N_4 – 2.23	*Fe_3N/Fe_2O_3/C_3N_4* CO – 8.03 CH_4 – 1.6	[118]
37	$K_4Nb_6O_{17}$/Fe_3N/α-Fe_2O_3/C_3N_4			$K_4Nb_6O_{17}$/Fe_3N/α-Fe_2O_3/C_3N_4 – 2.75	*$K_4Nb_6O_{17}$/Fe_3N/α-Fe_2O_3/C_3N_4* CO – 7.01 CH_4 – 1.3	[119]
38	2D/2D WO_3/g-C_3N_4	WO_3	g-C_3N_4	WO_3 – 2.77 g-C_3N_4 – 2.68	*WO_3* H_2 – no activity *g-C_3N_4*	[120]

					H_2 - 583 *WO_3/g-C_3N_4* H_2 - 982	
39	p-CNQDs/Vo-ZnO			ZnO – 3.04 p-CNQDs – 2.91	*p-CNQDs/Vo-ZnO* H_2 – 481.3	[121]
40	$BiVO_4/WO_3$	$BiVO_4$	WO_3	$BiVO_4$ – 2.36 WO_3 – 2.48 $BiVO_4/WO_3$ – 2.32	*$BiVO_4$* CO – 14.64 *WO_3* CO – 17.31 *$BiVO_4/WO_3$* CO – 29.14 H_2 – 9.24	[122]
41	TiO_2 nanofiber/$CsPbBr_3$	TiO_2	$CsPbBr_3$		*TiO_2 nanofiber* CO – 4.68 *TiO_2 nanofiber/ $CsPbBr_3$* CO – 9.02	[123]

5.2. p-p heterojunction S-scheme for CO_2 reduction Research on p-p semiconductor heterojunctions is limited because there are less p-type semiconductors suitable for p-p heterojunctions compared to other semiconductors such as n-type. p-p junctions (with the p semiconductor Fermi level slightly above the VB) limit the electron density, which is needed for the photocatalytic reduction of CO_2. However, a recent study by Mokhtar et al. [124], reported the incorporation of PdO in $GdFeO_3$ in a S-scheme $PdO/GdFeO_3$ heterojunction, which resulted in a lowering of the band gap and enhanced photocatalytic reduction of CO_2 (**Table 3**, item 1). Mott-Schottky plots from the study proposed that both PdO and $GdFeO_3$ are p-type

semiconductors. The heterojunction formation amongst PdO and $GdFeO_3$ enable S-Scheme charge transfer to occur resulting in band bending and electric field (E) generation at the interface and the unified Fermi levels [124]. The photocatalytic reduction path with energy potential for CO_2 into CH_3OH is schematically represented in **Figure 23**.

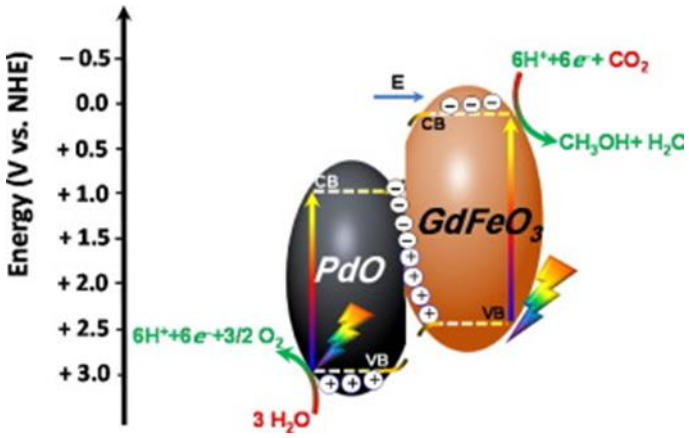

Fig. 23. Band diagrams, charge separations and photoreduction route of CO_2 into methanol over PdO/$GdFeO_3$ heterostructures. Printed with permission from [124]. Copyright 2023, Elsevier.

Ávila-López et al. [125] reported the use of CuO/Cu_2O and NiO/Ni_2O_3 for CO_2 photoreduction to selectively yield CH_4 and CH_3OH (CuO/Cu_2O) and CO and HCOOH (NiO/Ni_2O_3), respectively. It is proposed that electrons (e-) in the CB of Cu_2O (in CuO/Cu_2O) transferred to the CB of CuO, which allowed for $CO_2^{\delta-}$ species interaction. At the same time, photogenerated electrons in the NiO conduction band transferred to the Ni_2O_3 to allow Ni-O = C = O interaction. The superior performance of the heterojunction was attributed to the unique rod-shape morphology, the presence of oxygen vacancies, and efficient charge transfer in the CuO/Cu_2O heterostructure (**Table 3**, item 2 and 3).

Table 3: A summary of p-p S-scheme heterojunction for CO_2 reduction.

Number	Catalyst	Oxidation site	Reduction site	Bandgap energies (eV)	Photocatalytic activity ($\mu molg^{-1}h^{-1}$)	Ref.
1	PdO/$GdFeO_3$	PdO	$GdFeO_3$	$GdFeO_3$ – 2.37	*$GdFeO_3$* CH_3OH – 22	[124]

				$PdO/GdFeO_3$ – 2.13	($198\ \mu mg^{-1}$)	
					$PdO/GdFeO_3$ CH_3OH – 136 ($1550\ \mu mg^{-1}$)	
2	CuO/Cu_2O	Cu_2O	CuO	CuO/Cu_2O – 1.6	*CuO/Cu_2O* CH_4 – 95 CH_3OH – 177 HCOOH – 1450	[125]
3	NiO/Ni_2O_3	NiO	Ni_2O_3	NiO/Ni_2O_3 – 3.2	*NiO/Ni_2O_3* CH_4 – 103 CH_3OH – 5 HCOOH – 4245	[125]

Generally, p-p semiconductors offer enhanced charge separation that can promote efficient charge separation. A favorable energy band alignment between the p-type and p-type semiconductors facilitates the transfer of photogenerated charge carriers, leading to improved photocatalytic activity. Copper oxide (CuO) and copper(I) oxide (Cu_2O), p-type semiconductors (CuO/Cu_2O), exhibit good visible light absorption properties which allow them to utilize a broader range of the solar spectrum for photocatalytic reduction of CO_2 [116]. On the other hand, p-type semiconductors generally present lower stability due to surface oxidation, thus limiting the duration of the photocatalyst application. In addition, lower electron mobility observed in p-type compared to n-type semiconductors, hinders efficient transport of electrons, and leads to lower overall photocatalytic performance [115].

5.3. p-n and n-p S-scheme heterojunctions for CO_2 reduction

The combination of p-type and n-type semiconductor materials for the development of "p-n" type heterojunctions, can sufficiently reduce the recombination rate of photogenerated electrons, thus improving the photocatalytic activity [126–128] due to better electrical and optical properties [129,130]. The p-n junctions have a built-in electrical field that effectively separates photoexcited electron-hole pairs. The likelihood of recombination is decreased by this separation

due to excellent migration of charge carriers, thus, increasing the overall photocatalytic activity. p-n semiconductors can inhibit backward reactions, which occurs when reduced species interact with electron-hole pairs and thus lower the yield of the desired reduction products. Furthermore, the high bandgap energy of p-n semiconductors typically results in a narrow spectrum of light absorption. Due to this restriction, only certain wavelengths of light can be used for photocatalysis, decreasing their overall efficiency. The issue with p-n semiconductor production is that it can be technically difficult and demands exact control over doping and junction formation. Their complexity may make synthesis more expensive and challenging [131–135].

An n-p heterojunction, on the other hand, is formed by interfacing an n-type and a p-type semiconductor material leading to a flow of electrons at the interface in the opposite direction until the Fermi levels are equilibrated [136–139]. Construction of an n-p heterojunction facilitates the separation of photogenerated carriers in photocatalytic systems [140–144]. Due to their smaller bandgap energy, n-p semiconductors frequently absorb light throughout a larger spectrum. They can take in a wider range of light, including visible light, which is present in greater amounts in solar radiation. Their photocatalytic activity is improved by the larger absorption spectrum. Compared to p-n semiconductors, n-p semiconductors are typically simpler to synthesize. This property distinguishes n-p semiconductors from other semiconductors. Because the doping and junction production processes are more straightforward, they are easier to use and more economical. n-p junctions may, however, have less effective charge separation than p-n junctions. This could result in higher rates of electron-hole recombination, which would lower the overall photocatalytic efficiency. A greater backward reaction rate in n-p semiconductors can also result in more reduced species recombining with electron-hole pairs. The yield of the targeted reduction products may decrease as a result. It's crucial to remember that the specific application, required photocatalytic activity, and accessible light source all influence whether p-n or n-p semiconductors are used for photocatalytic reduction. The decision should be based on the specific requirements of the process since both types of semiconductors have benefits and drawbacks [133,134,145–147].

Huang et al. [148] reported the amination of CdS, 2D/2D BiOBr/CdS-diethylenetriamine (B/CS-DETA) S-scheme heterojunction for CO_2 reduction. It was reported that 2D/2D BiOBr/CdS-diethylenetriamine photocatalyst exhibited superior photocatalytic activity compared to the CdS-

D alone. The photocatalyst, 2D/2D BiOBr/CdS-diethylenetriamine, exhibited high stability. The photocatalytic mechanism for 2D/2D BiOBr/CdS-diethylenetriamine is shown in **Figure 24**. The VB and CB position of CdS is higher than BiOBr. The authors confirmed the transfer of photogenerated electrons from VB of CdS to CB of BiOBr when 2D/2D BiOBr/CdS-diethylenetriamine heterojunction when irradiated. This transfer reduces the recombination of electron–hole pairs. The improved stability due to the existence of amine molecules and increased area of the contact, thereby speeding up the separation and transmission of carriers which leads to the superior photocatalytic activity of 2D/2D BiOBr/CdS-diethylenetriamine for CO_2 reduction (**Table 4**, item 1).

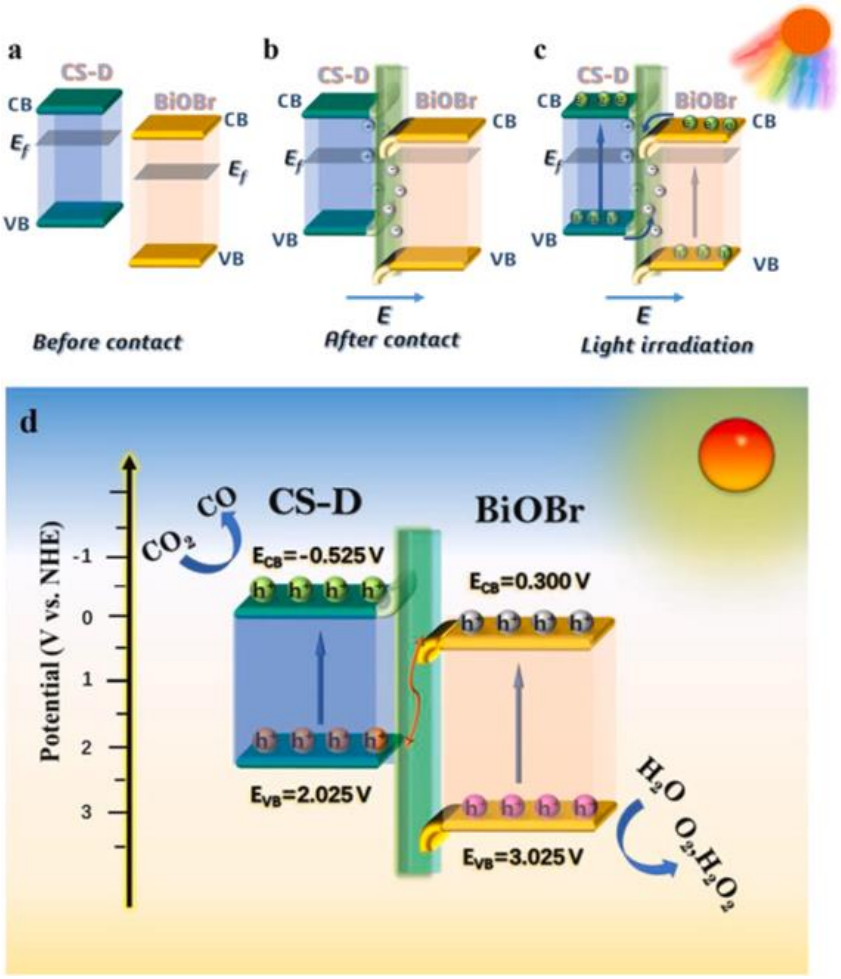

Fig. 24. Schematic illustration showing band energy positions of semiconductors (a) before contact, (b) after contact, and (c) under irradiation. (d) Photocatalytic CO_2 reduction pathways of

the BiOBr/CdS-diethylenetriamine heterojunction. Printed with permission from [148]. Copyright 2022, Elsevier.

As reported by Huang et al. [148], it is widely accepted that the combination of "p-n" type heterojunctions limits fast recombination of photogenerated charge carriers (e^-/h^+) and influence heterostructure band gap properties. Several other studies [149,150,159,151–158] have also reported similar findings of improved catalytic activities (**Table 4**, items 2-12).

Zhao et al. [160] reported that hierarchical heterostructures, carbon-supported In_2O_3@MO (MO = ZnO, C, and $ZnCo_2O_4$) derived from dual MOF, n-p heterojunctions promote electron-hole separation and accelerate carrier transfer. The hollow-structure of the C-In_2O_3@MO heterojunction reduced the bulk-to-surface diffusion path of light-excited electrons and holes, and effectively absorbed solar energy through reflection in the internal void and light scattering. The combination of In_2O_3 with $ZnCo_2O_4$ (narrow band gap), extended visible-light response range thus confirming narrowing of the band gap. Consequently, the In_2O_3@$ZnCo_2O_4$ heterojunction photocatalysts played a pivotal role in improving the efficiency of CO_2 conversion (**Table 4**, item 1). The study compared n-p heterostructure In_2O_3@$ZnCo_2O_4$ activity to In_2O_3@ZnO n-n heterojunction photocatalyst. The low activity of In_2O_3@ZnO n-n heterojunction photocatalyst, was due to the insufficient separation of electron-holes across the heterojunctions, which were unable to suppress electron-hole rapid recombination on semiconductors [160]. **Figure 25 (a-c)** depicts the energy level and charge separation of bare semiconductors, In_2O_3 and $ZnCo_2O_4$, and heterostructures C-In_2O_3@ZnO, C-In_2O_3@Co_3O_4, C-In_2O_3@$ZnCo_2O_4$ under light irradiation. A photocatalytic mechanism for CO_2 reduction using In_2O_3@$ZnCo_2O_4$ n-p heterojunction is also provided in **Figure 25d**.

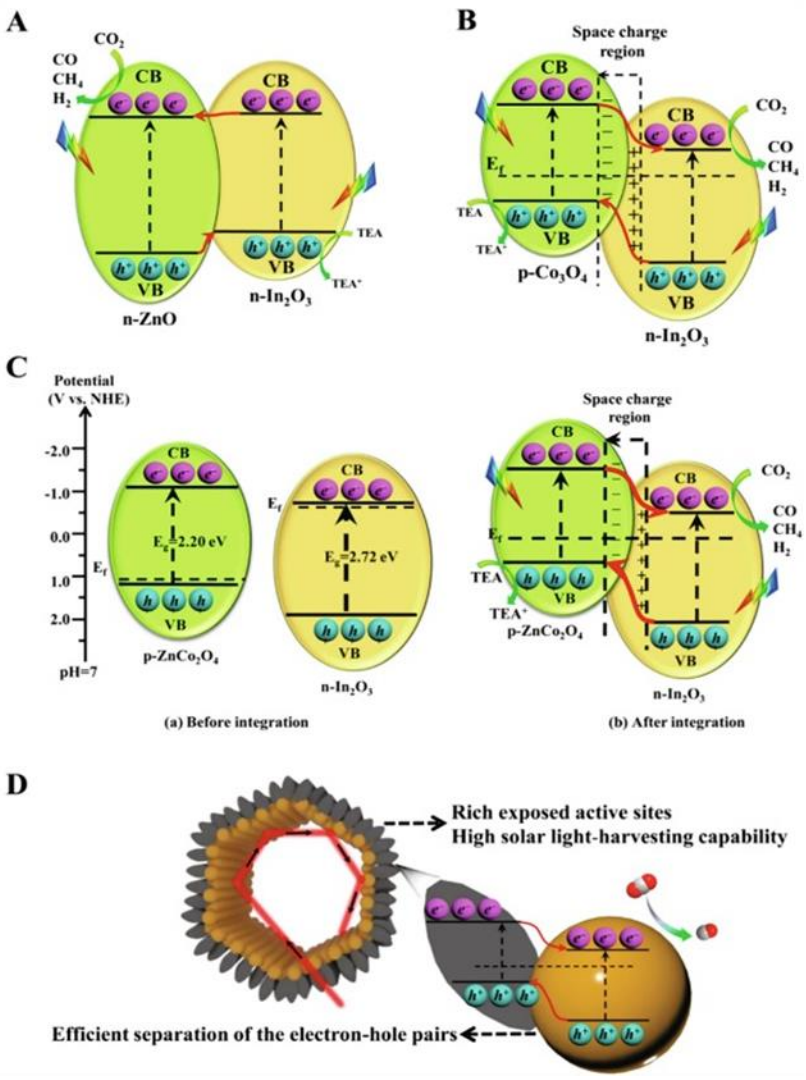

Fig. 25. Schematic illustration of the band structure and charge separation of (A) C-In_2O_3@ZnO and (B) C-In_2O_3@Co_3O_4 heterojunctions under light irradiation. (C) Schematic illustration of (a) energy level for bare In_2O_3 and $ZnCo_2O_4$, and (b) the band structure and charge separation of the C-In_2O_3@$ZnCo_2O_4$ under light irradiation. (D) Schematic of the hypothetical photocatalytic mechanisms for CO_2 reduction on the hollow C-In_2O_3@$ZnCo_2O_4$ n-p heterojunction. Printed with permission from [160]. Copyright 2021, Elsevier.

Jiang et al. [161] suggested that a CeO_2@$MoSe_2$ hollow n-p heterojunction with surface defects and rich vacancy sites of oxygen improved the photocatalytic CO_2 activity reduction through enhancement of the surface area and activity sites of CeO_2@$MoSe_2$. The introduction of $MoSe_2$ material which has a narrow band gap semiconductor on CeO_2 exhibited an increased visible

light absorption range, enhanced activity for CO_2 to CH_4, as well as separation efficiency of photogenerated carriers. Incorporation of CeO_2 and $MoSe_2$, upon light irradiation, and resulted in the discovery of n-p heterojunction in the internal electric field. With the presence of oxygen vacancies on the CeO_2@$MoSe_2$ surface, the Fermi level of oxide moves upward, and the defect level appears near the bottom of the conduction band (**Table 4**, item 2).

Han et al. [162] reported that a NiIn LDH/In_2S_3 heterojunction effectively promoted photogenerated electron-hole transport and rapid electron transfer due to the n-p type heterojunction thus increasing CO_2 photoreduction activity. The NiIn LDH/In_2S_3 heterojunction exhibited a CO generation rate of 29.43 μmol g^{-1} h^{-1}, which is 3.5 and 4.3 times higher than pristine NiIn LDH and In_2S_3, and high stability under visible light irradiation for 9 h (**Table 4**, item 3). The internal electric field (IEF) in the S-scheme configuration was reported to be moving photoinduced electrons transfer from the CB of In_2S_3 to the VB of NiIn LDH, thereby easing photogenerated charge carriers' separation.

However, a study reported by Li et al. [163] shows that photocatalytic activity of the heterostructure ZnO–In_2O_3X%/MoS_2Y was governed by the photocatalysts' surface properties and the energy band structure. Photogenerated charge carriers on ZnO were participating more actively in the CO_2 photoreduction process in the presence of MoS_2 (lower band gap, 1.43 eV). Nonetheless, the limited photocatalytic activity of ZnO was ascribed to lower adsorption ability, its smaller specific surface area, larger bandgap of 3.14 eV, and fast recombination of the photo-generated carriers (**Table 4**, item 4).

There are few works relevant to photocatalytic CO_2 reduction by designing Bismuth based S-Bi_2WO_6/NiO [164], $BiPO_4$/BiOBr [165], AgBr/BiOBr [166,167], In_2O_3/BiOI [168] n-p heterostructures composites. The coupling of semiconductors, NiO, In_2O_3, AgBr, with Bismuth material (BiOBr and Bi_2WO_6) enhanced rapid separation and transfer of charges and enhanced its photocatalytic performance (**Table 4**, items 5-9). The construction of Bismuth based S-scheme heterojunction accelerates the separation and transfer of hole (h^+)/ electron (e^-) and can maintain a strong redox ability unlike the traditional type II heterojunction. For example, AgBr/BiOBr shows an S-scheme band structure, which enhances redox ability, charge-separation efficiency, adsorption, as well as activation of CO_2 (**Figure 26**). The AgBr/BiOBr heterojunction was 9.2 times higher compared to pristine BiOBr.

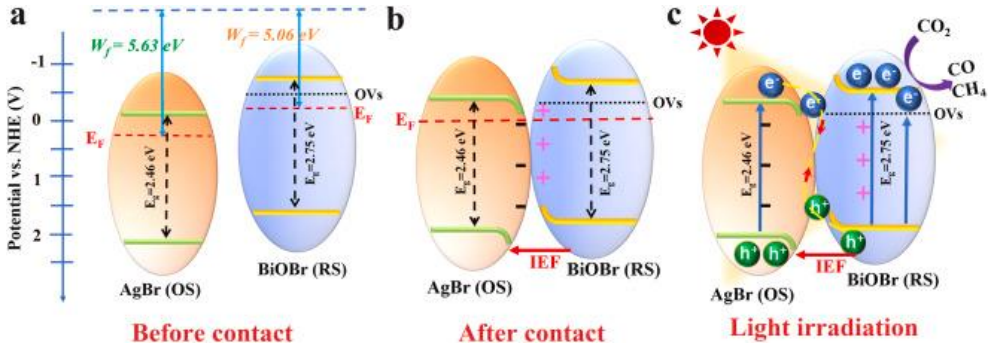

Fig. 26. The S-scheme charge transfer mechanism between AgBr and BiOBr under irradiation. Band energy positions of AgBr and BiOBr (a) before contact, (b) after contact, and (c) under irradiation. Printed with permission from [166]. Copyright 2022, Elsevier.

Experimental results from solvothermal prepared $CdSe_{0.8}S_{0.2}$-diethylenetriamine (DETA)/$SnNb_2O6$ heterostructure illustrated that the CO production rate using 1D/2D CdSe0.8S0.2-DETA/$SnNb_2O_6$ composite can be 4.8 and 2.8 higher compared to pristine CdSe0.8S0.2-DETA and $SnNb_2O_6$, respectively [169]. This was ascribed to strong redox ability, recombination of electron-hole pairs inhibition, and effective separation and transfer of electrons. The deposition of $CdSe0.8S_{0.2}$-DETA (lower band gap) nanowires on $SnNb_2O_6$ nanosheets improved the absorption range leading to more electron-hole pairs generation (**Table 4**, item 10).

Other related n-p heterostructured materials such as $WO_3/CuBiO_4$ [170], Ag2S/Sb_2S_3 [171], 2D/2D g-C_3N_4/MoS_2/Cu [114], g-C_3N_4/BiOI [172] and Bi_2O_3/$SrBi_4Ti4O_{15}$ [173], $Cd_{0.7}Zn_{0.3}Se$/Cu_2O@Cu [174] (**Table 4**, item 11-16) showed improved CO_2 reduction when semiconductors are combined. Charge transfer mechanisms in the design of n-p junctions is very important for efficient CO_2 photoreduction. Hence, the two types for n-p are S-scheme and type II heterojunction, which could be designed from series of oxidation photocatalysts (OP) and reduction photocatalyst (RP) (**Figure 26a**).

In type-II heterojunctions, the photogenerated electrons would transfer from CB (RP) to CB (OP), while the photogenerated holes would transfer from VB (OP) to VB (RP). The effective separation of electron–hole pairs is beneficial. With S-scheme heterojunction, electrons in the positively charged RP spontaneously diffuse to negatively charged OP (when semiconductor are in contact), thereby causing electron depletion layer and electron accumulation layer nearby RP and OP interface, respectively (**Figure 27**) [34]. Generally, S scheme is preferred over Z-scheme

as the latter suffers from charge-transfer related problems. A report by Xu et al. [34], the redox couples tend to be unstable and can react with one another. Consequently, the whole system electrons in the photocatalyst get corrupted. Furthermore, considering the charge transfer route, electrons in the photocatalyst with higher CB potential prefer to transfer via conductor to the photocatalyst with lower VB potential due to a larger driving force stemming from a higher potential difference.

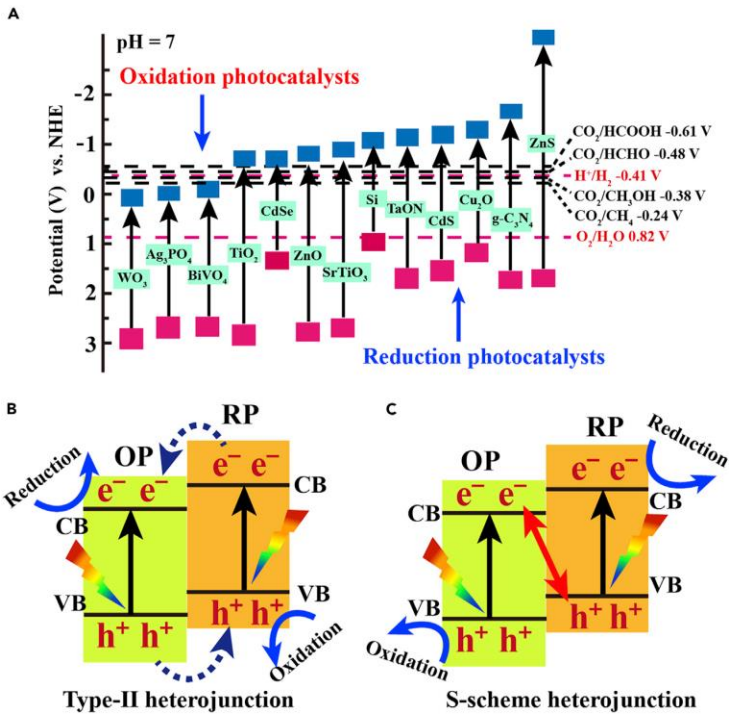

Fig. 27. (A) Band structures of various representative photocatalysts. Charge transfer routes between (B) Type-II and (C) S-Scheme heterojunctions. Printed with permission from [34]. Copyright 2020, Elsevier.

Table 4. A summary of works for p-n and n-p S-scheme heterojunctions for CO_2 reduction.

p-n heterojunction S-scheme for CO_2 reduction					
Catalyst	**Oxidation site**	**Reduction site**	**Bandgap energies (eV)**	**Photocatalytic activity ($\mu molg^{-1}h^{-1}$)**	**Ref.**
BiOBr/CdS-DETA	BiOBr	CdS-DETA	BiOBr – 2.71	*BiOBr* No reduction	[148]

			CdS-DETA – 2.55	*CdS-DETA* CO – 5.3 *BiOBr/CdS-DETA* CO – 19.4	
Ag_2O/Bi_2O_2S	Ag_2O	Bi_2O_2S	Ag_2O – 1.31 Bi_2O_2S – 1.30	*Ag_2O* CO – no reduction CH_4 – 4.94 (120 min) *Bi_2O_2S* No reduction *Ag_2O/Bi_2O_2S* CO – 14.49 (120 min) CH_4 – 12.06 (120 min)	[149]
CuPc/N-rich doped (001) TiO_2	CuPc	N-doped TiO_2	CuPc – 2.43 N-rich doped (001) TiO_2 – 2.41	*N-rich doped (001) TiO_2* CO – 0.6 *CuPc/N-rich doped (001) TiO_2* CO – 5.4	[150]
$MnOx/CeO_2$ @SnS_2/ Ni_2P	$MnOx/CeO_2$	SnS_2/ Ni_2P	CeO_2 – 2.75 SnS_2 – 2.43	*CeO_2* CO – 3.03 CH_4 – 0.32 *SnS_2* CO – 5.76 CH_4 – 0.41	[151]

				CeO_2@SnS_2 CO – 15.8 CH_4 – 0.58	
				MnOx/CeO_2@SnS_2/Ni_2P CO – 29.67 CH_4 – 0.71	
$ZnMn_2O_4$/ZnO	$ZnMn_2O_4$	ZnO	$ZnMn_2O_4$ – 1.98 ZnO – 3.15	CO – 3.251 CH_4 – 0.275	[152]
$CuCo_2O_4$/CeO_2	$CuCo_2O_4$	CeO_2	CeO_2 – 2.93 $CuCo_2O_4$/CeO_2 – 2.36	*CeO_2* CH_3OH – 440 (9 h) *$CuCo_2O_4$/CeO_2* CH_3OH – 1320 (9 h)	[153]
Black phosphorus (BP)/Bi_2WO_6	Black phosphorus	Bi_2WO_6	MBWO – 2.78 OvMBWO – 2.66	*Pt/BP- OvMBi$_2$WO$_6$* CO – 84.2 H_2 – 102.3	[154]
us-Cu_3P|S/g-C_3N_4	us-Cu_3P|S	g-C_3N_4	us-Cu_3P|S – 1.52 g-C_3N_4 – 2.85	*us-Cu_3P|S* no reduction *g-C_3N_4* CO – 58 *us-Cu_3P|S/g-C_3N_4* CO – 137	[155]
0D/1D $Cu_{2-x}S$/TiO_2	$Cu_{2-x}S$	TiO_2	$Cu_{2-x}S$ – 1.45 TiO_2 – 3.24	*TiO_2* CO – 3.6 CH_4 – 0.2	[156]

				$Cu_{2-x}S/TiO_2$ CH_4 – 14.1	
Ag/$AgVO_3$/TiO_2-NWs	Ag	TiO_2-NWs		*Ag/$AgVO_3$/TiO_2-NWs* CH_3OH – 9561	[157]
Co_3O_4/Ti^{3+}-TiO_2	Co_3O_4	Ti^{3+}-TiO_2	Co_3O_4 – 0.767 Ti^{3+}-TiO_2 – 0.720	*Co_3O_4* H_2 – 5.28 CH_4 – 12.93 CO – 1.21 *Ti^{3+}-TiO_2* H_2 – 12.75 CH_4 – 16.41 CO – 0.68 *Co_3O_4/Ti^{3+}-TiO_2* H_2 – 20.32 CH_4 – 80.57 CO – 9.85	[158]
NiO-In_2O_3/TiO_2	NiO-In_2O_3	TiO_2	TiO_2 – 3.11 NiO-In_2O_3/TiO_2 – 3.06	*TiO_2* CH_4 – 37 CO – 18 *NiO-In_2O_3/TiO_2* CH_4 – 240 CO – 60	[159]
n-p heterojunction S-scheme for CO_2 reduction					
C-In_2O_3@$ZnCo_2O_4$	$ZnCo_2O_4$	C-In_2O_3	In_2O – 2.72 $ZnCo_2O_4$ – 2.20	*C-In_2O_3@$ZnCo_2O_4$* CO – 23.3	[160]

				C-In_2O_3@$ZnCo_2O_4$ CO – 44.1 CH_4 – 10.9	
CeO_2@$MoSe_2$	CeO_2	$MoSe_2$	H-CeO_2 – 2.20 $MoSe_2$ – 1.45	*H-CeO_2* CO – 15. 3 (4 h) *$MoSe_2$* CO – 7.5 (4 h) *CeO_2@$MoSe_2$* CH_4 – 10.2 (4 h) CO – 33.2 (4 h)	[161]
NiIn LDH/In_2S_3	In_2S_3	NiIn LDH	NiIn LDH – 1.48 In_2S_3 – 2.11 NiIn LDH/In_2S_3 – 1.36	*NiIn LDH* CO – 6.87 *In_2S_3* CO – 8.30 *NiIn LDH/In_2S_3* CO – 29.43	[162]
ZnO–In_2O_3/MoS_2	ZnO–In_2O_3	MoS_2	ZnO – 3.14 In_2O_3 – 2.89 MoS_2 – 1.43	*ZnO* CO – 2.044 (8 h) CH_4 – 0.887 (8 h) *In_2O_3* CO – 1.556 (8 h) CH_4 – 0.751 (8 h) *MoS_2* CO – 0.774 (8 h) CH_4 – 0.699 (8 h)	[163]

			ZnO– *In_2O_3X%/MoS_2Y%* CO – 4.502 (8 h) CH_4 – 2.438 (8 h)	
S-Bi_2WO_6	NiO	NiO – 2.35 S-Bi_2WO_6 – 2.93 S-Bi_2WO_6/NiO – 2.15	*S-Bi_2WO_6* No reduction *NiO* CO – 21.5 CH_4 – 6.68 *S-Bi_2WO_6/NiO* CO – 46.9 CH_4 – 12.1	[164]
BiOBr	$BiPO_4$	BiOBr – 2.77 $BiPO_4$/BiOBr – 2.85	*$BiPO_4$/BiOBr* CO – 17.18 *$BiPO_4$/BiOBr* CO – 32.94	[165]
AgBr	BiOBr	AgBr – 2.46 BiOBr – 2.75	*AgBr* No reduction *BiOBr* CO – 20.1 CH_4 – 1.2 *AgBr/BiOBr* CO – 212.6 CH_4 – 5.7	[166]
AgBr	BiOBr	AgBr –	*AgBr*	[167]

		2.29 BiOBr – 2.56	CO – 0.12 *BiOBr* CO – 4.27 *AgBr/BiOBr* CO – 12.43	
BiOI	In_2O_3	In_2O_3 – 2.62 BiOI – 1.79	*In_2O_3* CO – 2.25 CH_4 – 2.82 *BiOI* CO – 2.24 CH_4 – 2.91 *In_2O_3/BiOI* CO – 11.98 CH_4 – 5.69	[168]
$SnNb_2O_6$	$CdSe_{0.8}S_{0.2}$-DETA	$CdSe_{0.8}S_{0.2}$-DETA – 1.71 $SnNb_2O_6$ – 2.51	*$CdSe_{0.8}S_{0.2}$-DETA* CO – 3.6 *$SnNb_2O_6$* CO – 6.2 *$CdSe_{0.8}S_{0.2}$-DETA/$SnNb_2O_6$* CO – 17.31	[169]
WO_3	$CuBiO_4$	WO_3 – 2.65 $CuBiO_4$ – 1.86	*WO_3/$CuBiO_4$* CO – 1,115.8 μmol/m^2 (9 h) CH_4 – 67.2	[170]

			µmol/m^2 (9h)	
Ag_2S	Sb_2S_3	Ag_2S – 0.85 Sb_2S_3 – 1.73	*Ag_2S* CH_4 – 0.15 CO – 0.09 *Sb_2S_3* CH_4 – 1.12 CO – 0.71 *Ag_2S/Sb_2S_3* CH_4 – 6.75 CO – 1.22	[171]
2D/2D g-C_3N_4/MoS_2	Cu	g-C_3N_4 – 2.68 MoS_2 – 1.94 g-C_3N_4/MoS_2 /Cu – 2.2	*g-C_3N_4* CO – 11 CH_4 – 15 *MoS_2* CO – 1.96 CH_4 – 3.9 *2D/2D g-C_3N_4/MoS_2/Cu* CO – 146.7	[114]
BiOI	g-C_3N_4	g-C_3N_4 – 2.78 BiOI – 1.96	*g-C_3N_4* CO – 2.30 *BiOI* CO – 2.85 *g-C_3N_4/BiOI* CO – 12.45	[172]

Bi_2O_3	$SrBi_4Ti_4O_{15}$	Bi_2O_3 – 2.97 $SrBi_4Ti_4O_{15}$ – 3.30	Bi_2O_3 No reduction $SrBi_4Ti_4O_{15}$ CO – 27.2 $Bi_2O_3/SrBi_4Ti_4O_{15}$ CO – 73. CH_4 – 30.2	[173]
Cu_2O@Cu	$Cd_{0.7}Zn_{0.3}Se$	$Cd_{0.7}Zn_{0.3}Se$ – 1.81 Cu_2O@Cu – 2.12	*$Cd_{0.7}Zn_{0.3}Se$* CO – 13.3 *Cu_2O@Cu* CO – 4.7 *$Cd_{0.7}Zn_{0.3}Se/Cu_2O$@Cu* CO – 50.5	[174]
Bi_2MoO_6	BiOI	Bi_2MoO_6 – 2.50 BiOI – 1.88	*BiOI* CO – 2.39 CH_4 – 1.68 *Bi_2MoO_6* No reduction *Bi_2MoO_6/BiOI* CO – 8.34 CH_4 – 3.31	[175]
AgCl	$ZnTiO_3$	$ZnTiO_3$ – 3.17	*Ag/AgCl/$ZnTiO_3$* CO – 95.0	[176]

	Ag/AgCl/Z nTiO$_3$ – 2.89	CH$_4$ – 18.5

Overall, the selectivity of various S-scheme heterojunctions towards CH_4, and/or CO usually depend on surface properties, band alignment, and active site composition, which are mainly controlled by the choice of semiconductors, and metal co-catalysts employed in the S-scheme heterojunctions [34, 177]. When two semiconductors with different band gaps combine, they promote electron-hole pair separation with enhance photocatalytic reduction of CO_2 to CH_4 or CO.

The CO_2 reduction reactions are thermodynamically favourable. The introduction of metal co-catalysts such as Pt [101], Cu [141], Fe [177] or Ag [167] in the photocatalytic s-scheme junctions, often promote the reduction of CO_2 into CO and H_2 by breaking the C-H bonds of CH_4 produced. Likewise, metal-free COFs such as triazine-based COF membranes [178] gave high CO yield. MoS [109], Nb_2O_5 [97] and Fe-based catalysts promote CH_4 formation due their reductive nature. For example, CdS/TiO_2 [100] show selectivity towards CH_4 in a s-scheme junction of TiO_2 and CdS. The CdS component acts as a reducing agent to generate electrons for the reduction of CO_2. In general, the design of s-scheme junctions influences the selectivity of CH_4, and CO production.

6. Future directions and perspectives

S-scheme photocatalysts are promising materials for CO_2 conversion and several improvements can enhance their evolution, including (1) broadening their application from powder-based photocatalysts, (2) introducing them into the field of photoelectrochemistry, (3) creating facile synthesis strategies for co-catalyst doping and, (4) improving upon other non-n-type forms (e.g., p-type, n-p type, p-n type).

S-scheme heterojunctions have mainly been synthesized in powdered form with applications of S-scheme heterojunctions on substrate anchored thin films being limited. Powdered photocatalysts suffer many disadvantages compared to their non-powdered counterparts (e.g., thin films). For example, the quantity of powder used must be thoroughly optimized to produce

enough photoreactivity while inhibiting shading or light scattering effects that can hinder the efficiency of the photocatalytic reactions. Additionally, recovery of the particles from the aqueous phase remains a major challenge. A second underutilized opportunity for S-scheme heterojunction photocatalysts is their application in photoelectrochemical systems. Photoelectrochemistry combines photochemical and electrochemical techniques into a single system. In this system, a semiconducting anode or cathode is photoexcited, which generates current to the cathode or anode; oxidation reactions occur at the semiconductor interface while reduction reactions take place at the opposite anode or cathode. Because photocatalysts typically behave as semiconductors, novel photocatalysts can be made and deposited on a substrate for enhancement. However, as aforementioned, thin film deposition of S-scheme photocatalysts is an underexplored topic and is still in its infancy. The application of photoelectrochemical systems to CO_2 reduction is also limited but has been shown by Yuan et.al. [179]. The authors noted that the use of photoelectrochemical systems for CO_2 reduction is challenging due to the need for large overpotential, but that this may be mitigated by using co-catalysts.

When incorporated into heterojunctions, co-catalysts can improve the photocarrier separation rate and increase photocatalytic efficiency by altering the surface of the RP and OP [180]. This surface modification may take many forms. For example, when Pt atoms were incorporated into the surface of a g-C3N4/BiOCl S-scheme photocatalyst, they served as active sites for CO_2 reduction. They enhanced photocatalysis by lowering the energy barrier of multiple reactions and making the CO_2 to COOH step spontaneous [181]. In another work, Cheng and co-workers [182] synthesized Co-doped CeO_2/crystalline carbon nitride S-scheme photocatalysts for CO_2 reduction. In this work, Co served various roles; it enhanced the material's light absorption intensity, altered its electronic properties and local crystallinity, and suppressed recombination. Ultimately, the enhanced electronic transferability of electrons needed for efficient CO_2 to CH_4 conversion (up to 181.7 μmol g^{-1} CH_4) was attributed to Co doping. Characterization of this material revealed that it was an n-type, which encourages future designs of n-type co-catalyst S-scheme heterojunctions.

For CO_2 conversion into desired value-added products, a more logical design of S-scheme heterojunctions is required. More research combining experimental and computational investigation is required to acquire a better understanding of the mechanism of S-scheme charge-

transfer processes at the molecular and atomic levels. For example, machine learning could be employed to predict suitable OP and RP for CO_2 reduction into hydrocarbon fuels with exceptional redox potential. Aside from figuring out new photocatalysts such as OP or RP through screening and artificial intelligence, it is pertinent to mention that various modification techniques on existing materials are attainable. For example, to achieve the optimized S-scheme heterojunction system, suitable oxidation and reduction cocatalysts and co-dopants must be loaded on the surface of OP and RP. Furthermore, there is limited research on p-p semiconductors because the p-p junctions (with p semiconductor Fermi level slightly above VB) limit the charge-carrier density, which is needed for the photocatalytic reduction of CO_2. As such, more research works must be devoted on n-n junctions to form a reasonable S-scheme to maximize their photocatalytic reduction potential in CO_2 transformation.

7. Conclusions

Overall, S-scheme heterojunctions show promise in their application for CO_2 reduction and have evolved even since their introduction in 2020. This review highlights that, compared to the previous generations of heterojunctions (traditional Z-scheme, type II-scheme, all solid state Z-scheme and direct Z-scheme) S-scheme heterojunctions are preferred, as their mechanism of action allows for greater charge separation and redox potential. Although they are distinct in their mechanism, S-scheme heterojunctions are derived from Z-scheme heterojunctions and thus proper characterization using techniques such as KPFM (surface potential and morphology), XPS (binding energy), EPR (paramagnetic moments and unpaired electrons), and DFT (theoretical mechanisms) is pertinent. The corresponding synthesis method should be selected based on several factors including the desired amount of tunability (e.g., for size, homogeneity, surface area), sustainability score, ease of synthesis, and cost. Synthesis of various S-scheme heterojunctions (n-n, p-p, n-p and p-n) can be carried out based on the desired enhancement, for example, improved charge separation in p-n heterojunctions compared to enhanced electron mobility in n-n heterojunctions. All four types of S-scheme heterojunctions have been used for CO_2 conversion and are promising. The unique analysis from this review provides insight into how to advance S-scheme photocatalysts from a synthesis and characterization perspective and gives guidance to how S-scheme photocatalysts can be further improved (e.g., using p-types and co-catalysts). If suggested changes are followed, the emergence of S-scheme photocatalysts for

CO_2 conversion would greatly enhance the efficiency, reduce the cost and provide novelty in the use of photocatalysts for CO_2 conversion.

Funding

This research received no external funding.

Acknowledgements

Alli, Y.A. would like to express profound gratitude to LCC-CNRS for postdoctoral research activities. Dr Ogunlaja would also like to appreciate the support of Royal Society of Chemistry (R22-3427614666).

Conflicts of interest

The authors declare no conflict of interest.

References

[1] NOAA. Monthly Global Climate Report for Annual 2022., (2023).

[2] H.-O. Portner, D.C. Roberts, H. Adams, E. Al., Climate change 2022: Impacts, adaptation and vulnerability. 2022, (2022) 3675p.

[3] Carbon dioxide now more than 50% higher than pre-industrial levels, (2022).

[4] NOAA. Annual Mean Global Carbon Dioxide Growth Rates, (2023).

[5] M. Beuse, B. Steffen, M. Dirksmeier, T.S. Schmidt, Comparing CO2 emissions impacts of electricity storage across applications and energy systems, Joule. 5 (2021) 1501–1520. https://doi.org/10.1016/j.joule.2021.04.010.

[6] R. Lal, Carbon sequestration, Philos. Trans. R. Soc. B Biol. Sci. 363 (2008) 815–830. https://doi.org/10.1098/rstb.2007.2185.

[7] D.P. Schrag, Preparing to capture carbon, Science (80-.). 315 (2007) 812–813. https://doi.org/10.1126/science.1137632.

[8] A.F. Service, U. Forest, S. Unl, F. Publications, D.J. Nowak, U.F. Service, E.J. Greenfield, U.F. Service, R.E. Hoehn, U.F. Service, E. Lapoint, U.F. Service, J. David, J. Eric, E. Robert, D.J. Nowak, E.J. Green, R.E. Hoehn, E. Lapoint, DigitalCommons @ University of Nebraska - Lincoln Carbon storage and sequestration by trees in urban and community areas of the United States Carbon storage and sequestration by trees in urban and community areas of the United States, (2013).

[9] A. Baiker, Utilization of carbon dioxide in heterogeneous catalytic synthesis, in: Appl. Organomet. Chem., 2000: pp. 751–762. https://doi.org/10.1002/1099-0739(200012)14:12<751::AID-AOC85>3.0.CO;2-J.

[10] J. Ma, N. Sun, X. Zhang, N. Zhao, F. Xiao, W. Wei, Y. Sun, A short review of catalysis for CO2 conversion, Catal. Today. 148 (2009) 221–231. https://doi.org/10.1016/j.cattod.2009.08.015.

[11] J. Li, H. Yuan, W. Zhang, B. Jin, Q. Feng, J. Huang, Z. Jiao, Advances in Z-scheme semiconductor photocatalysts for the photoelectrochemical applications: a review, Carbon Energy. 4 (2022) 294–331.

[12] Y.A. Alli, P.O. Oladoye, A.T. Onawole, H. Anuar, S. Adewuyi, O.D. Ogunbiyi, K. Philippot, Photocatalysts for CO2 reduction and computational insights, Fuel. 344 (2023) 128101. https://doi.org/10.1016/J.FUEL.2023.128101.

[13] H. Tong, S. Ouyang, Y. Bi, N. Umezawa, M. Oshikiri, J. Ye, Nano-photocatalytic materials: Possibilities and challenges, Adv. Mater. 24 (2012) 229–251. https://doi.org/10.1002/adma.201102752.

[14] K. Rajeshwar, N.R. de Tacconi, C.R. Chenthamarakshan, ChemInform Abstract: Semiconductor-Based Composite Materials: Preparation, Properties, and Performance, ChemInform. 32 (2010) no-no. https://doi.org/10.1002/chin.200148247.

[15] T. Tatarchuk, A. Peter, B. Al-Najar, J. Vijaya, M. Bououdina, Photocatalysis: Activity of Nanomaterials, in: Nanotechnol. Environ. Sci., Wiley-VCH Verlag, 2018: pp. 209–292. https://doi.org/10.1002/9783527808854.ch8.

[16] N. Shehzad, M. Tahir, K. Johari, T. Murugesan, M. Hussain, A critical review on TiO2 based photocatalytic CO2 reduction system: Strategies to improve efficiency, J. CO2 Util. 26 (2018) 98–122. https://doi.org/10.1016/j.jcou.2018.04.026.

[17] S. Nahar, M.F.M. Zain, A.A.H. Kadhum, H.A. Hasan, M.R. Hasan, Advances in photocatalytic CO2 reduction with water: A review, Materials (Basel). 10 (2017). https://doi.org/10.3390/ma10060629.

[18] T. Inoue, A. Fujishima, S. Konishi, K. Honda, Photoelectrocatalytic reduction of carbon dioxide in aqueous suspensions of semiconductor powders [3], Nature. 277 (1979) 637–638. https://doi.org/10.1038/277637a0.

[19] S. Li, M. Cai, Y. Liu, C. Wang, K. Lv, X. Chen, S-Scheme photocatalyst TaON/Bi2WO6 nanofibers with oxygen vacancies for efficient abatement of antibiotics and Cr (VI): Intermediate eco-toxicity analysis and mechanistic insights, Chinese J. Catal. 43 (2022) 2652–2664.

[20] S. Li, C. Wang, Y. Liu, M. Cai, Y. Wang, H. Zhang, Y. Guo, W. Zhao, Z. Wang, X. Chen, Photocatalytic degradation of tetracycline antibiotic by a novel Bi2Sn2O7/Bi2MoO6 S-scheme heterojunction: performance, mechanism insight and toxicity assessment, Chem. Eng. J. 429 (2022) 132519.

[21] Y. Ren, Y. Li, X. Wu, J. Wang, G. Zhang, S-scheme Sb2WO6/g-C3N4 photocatalysts with enhanced visible-light-induced photocatalytic NO oxidation performance, Chinese J. Catal. 42 (2021) 69–77.

[22] Y. Wang, K. Wang, J. Wang, X. Wu, G. Zhang, Sb2WO6/BiOBr 2D nanocomposite S-scheme photocatalyst for NO removal, J. Mater. Sci. Technol. 56 (2020) 236–243.

[23] P. Raizada, P. Thakur, A. Sudhaik, P. Singh, V.K. Thakur, A. Hosseini-Bandegharaei, Fabrication of dual Z-scheme photocatalyst via coupling of BiOBr/Ag/AgCl heterojunction with P and S co-doped g-C3N4 for efficient phenol degradation, Arab. J. Chem. 13 (2020) 4538–4552.

[24] Y. Su, X. Xu, R. Li, X. Luo, H. Yao, S. Fang, K. Peter Homewood, Z. Huang, Y. Gao, X.

Chen, Design and fabrication of a CdS QDs/Bi2WO6 monolayer S-scheme heterojunction configuration for highly efficient photocatalytic degradation of trace ethylene in air, Chem. Eng. J. 429 (2022) 132241. https://doi.org/10.1016/j.cej.2021.132241.

[25] L. Wang, B. Zhu, J. Zhang, J.B. Ghasemi, M. Mousavi, J. Yu, S-scheme heterojunction photocatalysts for CO2 reduction, Matter. 5 (2022) 4187–4211.

[26] V. Hasija, A. Kumar, A. Sudhaik, P. Raizada, P. Singh, Q. Van Le, T.T. Le, V.-H. Nguyen, Step-scheme heterojunction photocatalysts for solar energy, water splitting, CO 2 conversion, and bacterial inactivation: A review, Environ. Chem. Lett. 19 (2021) 2941–2966.

[27] A. Kumar, A. Khosla, S. Kumar Sharma, P. Dhiman, G. Sharma, L. Gnanasekaran, M. Naushad, F.J. Stadler, A review on S-scheme and dual S-scheme heterojunctions for photocatalytic hydrogen evolution, water detoxification and CO2 reduction, Fuel. 333 (2023). https://doi.org/10.1016/j.fuel.2022.126267.

[28] C. Xia, H. Wang, J.K. Kim, J. Wang, Rational Design of Metal Oxide-Based Heterostructure for Efficient Photocatalytic and Photoelectrochemical Systems, Adv. Funct. Mater. 31 (2021). https://doi.org/10.1002/adfm.202008247.

[29] D. Zhu, Z. Dong, F. Lv, C. Zhong, W. Huang, The development of balanced heterojunction photocatalysts, Cell Reports Phys. Sci. 3 (2022). https://doi.org/10.1016/j.xcrp.2022.101082.

[30] M. Lin, H. Chen, Z. Zhang, X. Wang, Engineering interface structures for heterojunction photocatalysts, Phys. Chem. Chem. Phys. 25 (2023) 4388–4407. https://doi.org/10.1039/d2cp05281d.

[31] A.J. Bard, Photoelectrochemistry and heterogeneous photo-catalysis at semiconductors, J. Photochem. 10 (1979) 59–75. https://doi.org/10.1016/0047-2670(79)80037-4.

[32] B.J. Ng, L.K. Putri, X.Y. Kong, Y.W. Teh, P. Pasbakhsh, S.P. Chai, Z-Scheme Photocatalytic Systems for Solar Water Splitting, Adv. Sci. 7 (2020). https://doi.org/10.1002/advs.201903171.

[33] L. Zhang, J. Zhang, H. Yu, J. Yu, Emerging S-Scheme Photocatalyst, Adv. Mater. 34 (2022) 1–14. https://doi.org/10.1002/adma.202107668.

[34] Q. Xu, L. Zhang, B. Cheng, J. Fan, J. Yu, S-Scheme Heterojunction Photocatalyst, Chem. 6 (2020) 1543–1559. https://doi.org/10.1016/j.chempr.2020.06.010.

[35] N. Serpone, A. V. Emeline, Semiconductor Photocatalysis — Past, Present, and Future Outlook, J. Phys. Chem. Lett. 3 (2012) 673–677. https://doi.org/10.1021/jz300071j.

[36] L. Wang, C. Bie, J. Yu, Challenges of Z-scheme photocatalytic mechanisms, Trends Chem. 4 (2022) 973–983. https://doi.org/10.1016/j.trechm.2022.08.008.

[37] Q. Xu, S. Wageh, A.A. Al-Ghamdi, X. Li, Design principle of S-scheme heterojunction photocatalyst, J. Mater. Sci. Technol. 124 (2022) 171–173. https://doi.org/10.1016/j.jmst.2022.02.016.

[38] M. Grätzel, Photoelectrochemical cells, Nature. 414 (2001) 338–344. https://doi.org/10.1038/35104607.

[39] J. Wang, G. Wang, B. Cheng, J. Yu, J. Fan, Sulfur-doped g-C3N4/TiO2 S-scheme heterojunction photocatalyst for Congo Red photodegradation, Chinese J. Catal. 42 (2021) 56–68.

[40] F. Xu, K. Meng, B. Cheng, S. Wang, J. Xu, J. Yu, Unique S-scheme heterojunctions in self-assembled TiO2/CsPbBr3 hybrids for CO2 photoreduction, Nat. Commun. 11 (2020) 1–9. https://doi.org/10.1038/s41467-020-18350-7.

[41] L. Zhang, J. Zhang, H. Yu, J. Yu, Emerging S-scheme photocatalyst, Adv. Mater. 34 (2022) 2107668.

[42] B. Liu, C. Bie, Y. Zhang, L. Wang, Y. Li, J. Yu, Hierarchically porous ZnO/g-C3N4 S-scheme heterojunction photocatalyst for efficient H2O2 production, Langmuir. 37 (2021) 14114–14124.

[43] A. Shawky, R.M. Mohamed, S-scheme heterojunctions: Emerging designed photocatalysts toward green energy and environmental remediation redox reactions, J.

Environ. Chem. Eng. 10 (2022) 108249. https://doi.org/10.1016/j.jece.2022.108249.

[44] Z. Li, S. Ye, P. Qiu, X. Liao, Y. Yao, J. Zhang, Y. Jiang, S. Lu, An S-scheme α-Fe 2 O 3/Cu 2 O photocatalyst for an enhanced primary amine oxidative coupling reaction under visible light, Dalt. Trans. 51 (2022) 10578–10586.

[45] M.E. Aguirre, R. Zhou, A.J. Eugene, M.I. Guzman, M.A. Grela, Cu2O/TiO2 heterostructures for CO2 reduction through a direct Z-scheme: Protecting Cu2O from photocorrosion, Appl. Catal. B Environ. 217 (2017) 485–493.

[46] M. Hou, L. Cui, F. Su, X. Dong, H. Dang, Two-step calcination synthesis of Z-scheme α-Fe2O3/few-layer g-C3N4 composite with enhanced hydrogen production and photodegradation under visible light, J. Chinese Chem. Soc. 67 (2020) 2050–2061.

[47] H. Zhu, Z. Chen, Y. Hu, L. Gong, D. Li, Z. Li, A novel immobilized Z-scheme P3HT/α-Fe2O3 photocatalyst array: Study on the excellent photocatalytic performance and photocatalytic mechanism, J. Hazard. Mater. 389 (2020) 122119.

[48] K. Kaviyarasan, S. Anandan, R.V. Mangalaraja, T. Sivasankar, M. Ashokkumar, Sonochemical synthesis of Cu2O nanocubes for enhanced chemiluminescence applications, Ultrason. Sonochem. 29 (2016) 388–393.

[49] J.-C. Wang, L. Zhang, W.-X. Fang, J. Ren, Y.-Y. Li, H.-C. Yao, J.-S. Wang, Z.-J. Li, Enhanced photoreduction CO2 activity over direct Z-scheme α-Fe2O3/Cu2O heterostructures under visible light irradiation, ACS Appl. Mater. Interfaces. 7 (2015) 8631–8639.

[50] F. Xu, K. Meng, S. Cao, C. Jiang, T. Chen, J. Xu, J. Yu, Step-by-step mechanism insights into the TiO2/Ce2S3 S-scheme photocatalyst for enhanced aniline production with water as a proton source, ACS Catal. 12 (2021) 164–172.

[51] X. Xu, Y. Sun, Z. Fan, D. Zhao, S. Xiong, B. Zhang, S. Zhou, G. Liu, Mechanisms for· O 2-and· OH production on flowerlike BiVO4 photocatalysis based on electron spin resonance, Front. Chem. 6 (2018) 64.

[52] O. Al-Madanat, B.N. Nunes, Y. AlSalka, A. Hakki, M. Curti, A.O.T. Patrocinio, D.W.

Bahnemann, Application of EPR spectroscopy in TiO2 and Nb2O5 photocatalysis, Catalysts. 11 (2021) 1514.

[53] M. Chiesa, E. Giamello, On the role and applications of electron magnetic resonance techniques in surface chemistry and heterogeneous catalysis, Catal. Letters. (2021) 1–20.

[54] Z. Dong, J. Zhou, Z. Zhang, Y. Jiang, R. Zhou, C. Yao, Construction of a p–n Type S-Scheme Heterojunction by Incorporating CsPbBr3 Nanocrystals into Mesoporous Cu2O Microspheres for Efficient CO2 Photoreduction, ACS Appl. Energy Mater. 5 (2022) 10076–10085.

[55] K.A. Baseden, J.W. Tye, Introduction to density functional theory: Calculations by hand on the helium atom, J. Chem. Educ. 91 (2014) 2116–2123.

[56] M. Hu, Z. Yao, X. Wang, Characterization techniques for graphene-based materials in catalysis, AIMS Mater. Sci. 4 (2017) 755–788.

[57] Z. Wang, B. Cheng, L. Zhang, J. Yu, H. Tan, BiOBr/NiO S-Scheme Heterojunction Photocatalyst for CO2 Photoreduction, Sol. RRL. 6 (2022). https://doi.org/10.1002/solr.202100587.

[58] K. Li, Y. Zhang, J. Jia, L. Zheng, B. Li, X. Li, T. Zhang, X. Feng, G. Liu, 2D/2D Carbon Nitride/Zn-Doped Bismuth Vanadium Oxide S-Scheme Heterojunction for Enhancing Photocatalytic CO2 Reduction into Methanol, Ind. & Eng. Chem. Res. 62 (2023) 5552–5562. https://doi.org/10.1021/acs.iecr.2c03536.

[59] J. Hua, Z. Wang, J. Zhang, K. Dai, C. Shao, K. Fan, A hierarchical Bi-MOF-derived BiOBr/Mn0.2Cd0.8S S-scheme for visible-light-driven photocatalytic CO2 reduction, J. Mater. Sci. Technol. 156 (2023) 64–71. https://doi.org/10.1016/j.jmst.2023.03.003.

[60] L.R. Jabbar, A. Al-Farraji, S-scheme ZIF-8/Ag2S heterojunction photocatalyst for degradation of organic pollutant using batch and external loop airlift reactors, Environ. Nanotechnology, Monit. Manag. 18 (2022). https://doi.org/10.1016/j.enmm.2022.100701.

[61] D. Tuncel, A.N. Ökte, Improved Adsorption Capacity and Photoactivity of ZnO-ZIF-8 Nanocomposites, Catal. Today. 361 (2021) 191–197.

https://doi.org/10.1016/j.cattod.2020.04.014.

[62] L. Di, T. Xian, X. Sun, H. Li, Y. Zhou, J. Ma, H. Yang, Facile preparation of CNT/Ag2S nanocomposites with improved visible and NIR light photocatalytic degradation activity and their catalytic mechanism, Micromachines. 10 (2019). https://doi.org/10.3390/mi10080503.

[63] H. Yang, H. Hao, Y. Zhao, Y. Hu, J. Min, G. Zhang, J. Bi, S. Yan, H. Hou, An efficient construction method of S-scheme Ag2CrO4/ZnFe2O4 nanofibers heterojunction toward enhanced photocatalytic and antibacterial activity, Colloids Surfaces A Physicochem. Eng. Asp. 641 (2022). https://doi.org/10.1016/j.colsurfa.2022.128603.

[64] J. Liqiang, Q. Yichun, W. Baiqi, L. Shudan, J. Baojiang, Y. Libin, F. Wei, F. Honggang, S. Jiazhong, Review of photoluminescence performance of nano-sized semiconductor materials and its relationships with photocatalytic activity, Sol. Energy Mater. Sol. Cells. 90 (2006) 1773–1787. https://doi.org/10.1016/j.solmat.2005.11.007.

[65] T. Jia, F. Fu, F. Long, Z. Min, J. Zhao, J. Chen, J. Li, Synthesis, characterization and enhanced visible-light photocatalytic activity of Zn2SnO4/C nanocomposites with truncated octahedron morphology, Ceram. Int. 42 (2016) 13893–13899. https://doi.org/10.1016/j.ceramint.2016.05.199.

[66] J. Xie, G. Liu, X. Jiang, Z. Sui, S. Gao, One-step co-precipitation of MnSe2/CNTs as a high-performance cathode material for zinc-ion batteries, Ceram. Int. 49 (2023) 10165–10171. https://doi.org/10.1016/j.ceramint.2022.11.199.

[67] H. El-Hosainy, W.T. Alsaggaf, Z.I. Zaki, M.H.H. Mahmoud, Facile synthesis of S-scheme NiS@ZrO2 nano-heterostructure for superior degradation of antibiotic under visible light irradiation, Opt. Mater. (Amst). 133 (2022) 113011. https://doi.org/10.1016/j.optmat.2022.113011.

[68] A. Enesca, L. Isac, Tuned S-Scheme Cu2S_TiO2_WO3 Heterostructure Photocatalyst toward S-Metolachlor (S-MCh) Herbicide Removal, Materials (Basel). 14 (2021) 2231. https://doi.org/10.3390/ma14092231.

[69] V. Baviskar, D. Salunkhe, H. Tarkas, R. Wagh, P. Baviskar, R. Patil, Sensitization of TiO2 by chemically deposited Cu2S for solar cell: Effect of deposition time on photoelectrochemical performance, Optik (Stuttg). 207 (2020) 163890. https://doi.org/10.1016/j.ijleo.2019.163890.

[70] S.V. Singh, A. Sharma, S. Biring, B.N. Pal, Solution processed Cu2S/TiO2 heterojunction for visible-near infrared photodetector, Thin Solid Films. 710 (2020) 138275. https://doi.org/10.1016/j.tsf.2020.138275.

[71] C. Gao, J. Li, Z. Shan, F. Huang, H. Shen, Preparation and visible-light photocatalytic activity of In2S3/TiO2 composite, Mater. Chem. Phys. 122 (2010) 183–187. https://doi.org/10.1016/j.matchemphys.2010.02.030.

[72] T. Mise, T. Nakada, Low temperature growth and properties of Cu–In–Te based thin films for narrow bandgap solar cells, Thin Solid Films. 518 (2010) 5604–5609. https://doi.org/10.1016/j.tsf.2010.04.065.

[73] Y. Wu, D. Meng, Q. Guo, D. Gao, L. Wang, Study on TiO2/g-C3N4 S-Scheme heterojunction photocatalyst for enhanced formaldehyde decomposition, Opt. Mater. (Amst). 126 (2022) 112213. https://doi.org/10.1016/j.optmat.2022.112213.

[74] L. Zhang, Y.-H. Qin, L. Yang, C.-W. Wang, Multi-role graphitic carbon nitride-derived highly porous iron/nitrogen co-doped carbon nanosheets for highly efficient oxygen reduction catalyst, J. Colloid Interface Sci. 582 (2021) 1257–1265. https://doi.org/10.1016/j.jcis.2020.08.122.

[75] K. Bano, S. Kaushal, P.P. Singh, A review on photocatalytic degradation of hazardous pesticides using heterojunctions, Polyhedron. 209 (2021) 115465. https://doi.org/10.1016/j.poly.2021.115465.

[76] M. Tayyab, Y. Liu, Z. Liu, L. Pan, Z. Xu, W. Yue, L. Zhou, J. Lei, J. Zhang, One-pot in-situ hydrothermal synthesis of ternary In2S3/Nb2O5/Nb2C Schottky/S-scheme integrated heterojunction for efficient photocatalytic hydrogen production, J. Colloid Interface Sci. 628 (2022) 500–512. https://doi.org/10.1016/j.jcis.2022.08.071.

[77] M. Naguib, M. Kurtoglu, V. Presser, J. Lu, J. Niu, M. Heon, L. Hultman, Y. Gogotsi, M.W. Barsoum, Two-Dimensional Nanocrystals Produced by Exfoliation of Ti3AlC2, Adv. Mater. 23 (2011) 4248–4253. https://doi.org/10.1002/adma.201102306.

[78] Y. Wang, X. Hu, H. Song, Y. Cai, Z. Li, D. Zu, P. Zhang, D. Chong, N. Gao, Y. Shen, C. Li, Oxygen vacancies in actiniae-like Nb2O5/Nb2C MXene heterojunction boosting visible light photocatalytic NO removal, Appl. Catal. B Environ. 299 (2021) 120677. https://doi.org/10.1016/j.apcatb.2021.120677.

[79] A. Bahadoran, S. Ramakrishna, S. Masudy-Panah, J. Roshan De Lile, B. Sadeghi, J. Li, J. Gu, Q. Liu, Novel S-scheme WO3/CeO2 heterojunction with enhanced photocatalytic degradation of sulfamerazine under visible light irradiation, Appl. Surf. Sci. 568 (2021) 150957. https://doi.org/10.1016/j.apsusc.2021.150957.

[80] J. Li, J. Guo, J. Zhang, Z. Sun, J. Gao, Surface etching and photodeposition nanostructures core-shell Cu2O@CuO-Ag with S-scheme heterojunction for high efficiency photocatalysis, Surfaces and Interfaces. 34 (2022) 102308. https://doi.org/10.1016/j.surfin.2022.102308.

[81] X. Feng, P. Wang, J. Hou, J. Qian, Y. Ao, C. Wang, Significantly enhanced visible light photocatalytic efficiency of phosphorus doped TiO2 with surface oxygen vacancies for ciprofloxacin degradation: Synergistic effect and intermediates analysis, J. Hazard. Mater. 351 (2018) 196–205. https://doi.org/10.1016/j.jhazmat.2018.03.013.

[82] M. Basu, N. Garg, A.K. Ganguli, A type-II semiconductor (ZnO/CuS heterostructure) for visible light photocatalysis, J. Mater. Chem. A. 2 (2014) 7517–7525. https://doi.org/10.1039/c3ta15446g.

[83] W. Feng, Z. Fang, B. Wang, L. Zhang, Y. Zhang, Y. Yang, M. Huang, S. Weng, P. Liu, Grain boundary engineering in organic-inorganic hybrid semiconductor ZnS(en)0.5 for visible-light photocatalytic hydrogen production, J. Mater. Chem. A. 5 (2017) 1387–1393. https://doi.org/10.1039/c6ta09633f.

[84] X. Wang, R. Liu, T. Wang, B. Wang, Y. Xu, H. Wang, Dual roles of ZnS thin layers in significant photocurrent enhancement of ZnO/CdTe nanocable arrays photoanode, ACS

Appl. Mater. Interfaces. 5 (2013) 3312–3316. https://doi.org/10.1021/am4003793.

[85] J. Lee, H. Yoon, S. Kim, S. Seo, J. Song, B.U. Choi, S.Y. Choi, H. Park, S. Ryu, J. Oh, S. Lee, Long-term stabilized high-density CuBi2O4/NiO heterostructure thin film photocathode grown by pulsed laser deposition, Chem. Commun. 55 (2019) 12447–12450. https://doi.org/10.1039/c9cc06092h.

[86] P. Wang, L. Cao, Y. Chen, Y. Wu, J. Di, Photoelectrochemical Biosensor Based on Co3O4 Nanoenzyme Coupled with PbS Quantum Dots for Hydrogen Peroxide Detection, ACS Appl. Nano Mater. 2 (2019) 2204–2211. https://doi.org/10.1021/acsanm.9b00165.

[87] Y. Li, N. Zhang, W.W. Zhao, D.C. Jiang, J.J. Xu, H.Y. Chen, Polymer Dots for Photoelectrochemical Bioanalysis, Anal. Chem. 89 (2017) 4945–4950. https://doi.org/10.1021/acs.analchem.7b00162.

[88] X. Xin, Y. Zhang, X. Guan, J. Cao, W. Li, X. Long, X. Tan, Enhanced Performances of PbS Quantum-Dots-Modified MoS2 Composite for NO2 Detection at Room Temperature, ACS Appl. Mater. Interfaces. 11 (2019) 9438–9447. https://doi.org/10.1021/acsami.8b20984.

[89] Y.T. Xu, S.Y. Yu, Y.C. Zhu, G.C. Fan, D.M. Han, P. Qu, W.W. Zhao, Cathodic photoelectrochemical bioanalysis, TrAC - Trends Anal. Chem. 114 (2019) 81–88. https://doi.org/10.1016/j.trac.2019.03.002.

[90] H. Wang, B. Zhang, F. Zhao, B. Zeng, One-Pot Synthesis of N-Graphene Quantum Dot-Functionalized I-BiOCl Z-Scheme Cathodic Materials for “signal-Off” Photoelectrochemical Sensing of Chlorpyrifos, ACS Appl. Mater. Interfaces. 10 (2018) 35281–35288. https://doi.org/10.1021/acsami.8b12979.

[91] S. Bellani, M.R. Antognazza, F. Bonaccorso, Carbon-Based Photocathode Materials for Solar Hydrogen Production, Adv. Mater. 31 (2019) 1–33. https://doi.org/10.1002/adma.201801446.

[92] D. Xue, J. Wang, Y. Wang, G. Sun, J. Cao, H. Bala, Z. Zhang, Enhanced methane sensing properties of WO3 nanosheets with dominant exposed (200) facet via loading of SnO2

nanoparticles, Nanomaterials. 9 (2019) 351. https://doi.org/10.3390/nano9030351.

[93] C. Lazau, M. Poienar, C. Orha, D. Ursu, M. Nicolaescu, M. Vajda, C. Bandas, Development of a new “n-p” heterojunction based on TiO2 and CuMnO2 synergy materials, Mater. Chem. Phys. 272 (2021) 124999. https://doi.org/10.1016/j.matchemphys.2021.124999.

[94] B. Yu, Y. Wu, F. Meng, Q. Wang, X. Jia, M. Wasim Khan, C. Huang, S. Zhang, L. Yang, H. Wu, Formation of hierarchical Bi2MoO6/ln2S3 S-scheme heterojunction with rich oxygen vacancies for boosting photocatalytic CO2 reduction, Chem. Eng. J. 429 (2022) 1–11. https://doi.org/10.1016/j.cej.2021.132456.

[95] R.M. Mohamed, I.A. Mkhalid, M. Alhaddad, A. Basaleh, K.A. Alzahrani, A.A. Ismail, Construction of hierarchical ZnS@ZnO secured from metal – organic framework-ZnS@ZIF-8 for enhanced photoreduction of CO2, J. Taiwan Inst. Chem. Eng. 127 (2021) 208–219. https://doi.org/10.1016/j.jtice.2021.08.017.

[96] M. Xu, X. Zhao, H. Jiang, S. Chen, P. Huo, MOFs-derived C-In2O3/g-C3N4 heterojunction for enhanced photoreduction CO2, J. Environ. Chem. Eng. 9 (2021) 106469. https://doi.org/10.1016/j.jece.2021.106469.

[97] K. Wang, M. Cheng, N. Wang, Q. Zhang, Y. Liu, J. Liang, J. Guan, M. Liu, J. Zhou, N. Li, Inter-plane 2D/2D ultrathin La2Ti2O7/Ti3C2 MXene Schottky heterojunctions toward high-efficiency photocatalytic CO2 reduction, Chinese J. Catal. 44 (2023) 146–159. https://doi.org/10.1016/S1872-2067(22)64155-X.

[98] A. Meng, B. Cheng, H. Tan, J. Fan, C. Su, J. Yu, TiO2/polydopamine S-scheme heterojunction photocatalyst with enhanced CO2-reduction selectivity, Appl. Catal. B Environ. 289 (2021) 120039. https://doi.org/10.1016/j.apcatb.2021.120039.

[99] S. Gong, X. Teng, Y. Niu, X. Liu, M. Xu, C. Xu, L. Ji, Z. Chen, Construction of S-scheme 0D/2D heterostructures for enhanced visible-light-driven CO2 reduction, Appl. Catal. B Environ. 298 (2021) 120521. https://doi.org/10.1016/j.apcatb.2021.120521.

[100] L. Wang, D. Chen, S. Miao, F. Chen, C. Guo, P. Ye, J. Ning, Y. Zhong, Y. Hu, Nitric

acid-assisted growth of InVO4 nanobelts on protonated ultrathin C3N4 nanosheets as an S-scheme photocatalyst with tunable oxygen vacancies for boosting CO2 conversion, Chem. Eng. J. 434 (2022) 133867. https://doi.org/10.1016/j.cej.2021.133867.

[101] F. He, B. Zhu, B. Cheng, J. Yu, W. Ho, W. Macyk, 2D/2D/0D TiO2/C3N4/Ti3C2 MXene composite S-scheme photocatalyst with enhanced CO2 reduction activity, Appl. Catal. B Environ. 272 (2020) 119006. https://doi.org/10.1016/j.apcatb.2020.119006.

[102] F.A. Qaraah, S.A. Mahyoub, A. Hezam, A. Qaraah, F. Xin, G. Xiu, Synergistic effect of hierarchical structure and S-scheme heterojunction over O-doped g-C3N4/N-doped Nb2O5 for highly efficient photocatalytic CO2 reduction, Appl. Catal. B Environ. 315 (2022) 121585. https://doi.org/10.1016/j.apcatb.2022.121585.

[103] M. Liang, T. Borjigin, Y. Zhang, B. Liu, H. Liu, H. Guo, Controlled assemble of hollow heterostructured g-C3N4@CeO2 with rich oxygen vacancies for enhanced photocatalytic CO2 reduction, Appl. Catal. B Environ. 243 (2019) 566–575. https://doi.org/10.1016/j.apcatb.2018.11.010.

[104] Y. Zhao, Y. Chen, L. Du, Q. Wang, X. Liu, L. Li, G. Tian, Fabrication of size-controlled hierarchical ZnS@ZnIn2S4 heterostructured cages for enhanced gas-phase CO2 photoreduction, J. Colloid Interface Sci. 605 (2022) 253–262. https://doi.org/10.1016/j.jcis.2021.07.093.

[105] Z. Wang, Y. Chen, L. Zhang, B. Cheng, J. Yu, J. Fan, Step-scheme CdS/TiO2 nanocomposite hollow microsphere with enhanced photocatalytic CO2 reduction activity, J. Mater. Sci. Technol. 56 (2020) 143–150. https://doi.org/10.1016/j.jmst.2020.02.062.

[106] X. Zhao, J. Guan, J. Li, X. Li, H. Wang, P. Huo, Y. Yan, CeO2/3D g-C3N4 heterojunction deposited with Pt cocatalyst for enhanced photocatalytic CO2 reduction, Appl. Surf. Sci. 537 (2021) 147891. https://doi.org/10.1016/j.apsusc.2020.147891.

[107] K. Chen, X. Wang, Q. Li, Y.N. Feng, F.F. Chen, Y. Yu, Spatial distribution of ZnIn2S4 nanosheets on g-C3N4 microtubes promotes photocatalytic CO2 reduction, Chem. Eng. J. 418 (2021) 129476. https://doi.org/10.1016/j.cej.2021.129476.

[108] J. Wang, Y. Yu, J. Cui, X. Li, Y. Zhang, C. Wang, X. Yu, J. Ye, Defective g-C3N4/covalent organic framework van der Waals heterojunction toward highly efficient S-scheme CO2 photoreduction, Appl. Catal. B Environ. 301 (2022) 120814. https://doi.org/10.1016/j.apcatb.2021.120814.

[109] C.D. Reduction, Designing a 0D/1D S-Scheme Heterojunction of Cadmium Selenide and Polymeric Carbon Nitride for Photocatalytic Water Splitting and Carbon Dioxide Reduction, Molecule. 27 (2022) 6287.

[110] D.O. Adekoya, M. Tahir, N.A.S. Amin, g-C3N4/(Cu/TiO2) nanocomposite for enhanced photoreduction of CO2 to CH3OH and HCOOH under UV/visible light, J. CO2 Util. 18 (2017) 261–274. https://doi.org/10.1016/j.jcou.2017.02.004.

[111] Z. Dong, Z. Zhang, Y. Jiang, Y. Chu, J. Xu, Embedding CsPbBr3 perovskite quantum dots into mesoporous TiO2 beads as an S-scheme heterojunction for CO2 photoreduction, Chem. Eng. J. 433 (2022) 133762. https://doi.org/10.1016/j.cej.2021.133762.

[112] X. Yue, L. Cheng, J. Fan, Q. Xiang, 2D/2D BiVO4/CsPbBr3 S-scheme heterojunction for photocatalytic CO2 reduction: Insights into structure regulation and Fermi level modulation, Appl. Catal. B Environ. 304 (2022) 120979. https://doi.org/10.1016/j.apcatb.2021.120979.

[113] X. Zheng, H. Wang, J. Wen, H. Peng, In2S3-NiS co-decorated MoO3@MoS2 composites for enhancing the solar-light induced CO2 photoreduction activity, Int. J. Hydrogen Energy. 46 (2021) 36848–36858. https://doi.org/10.1016/j.ijhydene.2021.08.161.

[114] A.H. Bashal, K. Alkanad, M. Al-Ghorbani, S. Ben Aoun, M.A. Bajiri, Synergistic effect of cocatalyst and S-scheme heterojunction over 2D/2D g-C3N4/MoS2 heterostructure coupled Cu nanoparticles for selective photocatalytic CO2 reduction to CO under visible light irradiation, J. Environ. Chem. Eng. 11 (2023) 109545. https://doi.org/10.1016/j.jece.2023.109545.

[115] H. Feng, C. Zhang, M. Luo, Y. Hu, Z. Dong, S. Xue, P.K. Chu, A dual S-scheme TiO2@In2Se3@Ag3PO4 heterojunction for efficient photocatalytic CO2 reduction, Nanoscale. 14 (2022) 16303–16313. https://doi.org/10.1039/D2NR04707A.

[116] M. Sayed, B. Zhu, P. Kuang, X. Liu, B. Cheng, A.A. Al Ghamdi, S. Wageh, L. Zhang, J. Yu, EPR Investigation on Electron Transfer of 2D/3D g-C3N4/ZnO S-Scheme Heterojunction for Enhanced CO2 Photoreduction, Adv. Sustain. Syst. 6 (2022) 2100264. https://doi.org/10.1002/ADSU.202100264.

[117] J. Zhao, F. Liu, W. Wang, Y. Wang, N. Wen, Z. Zhang, W. Dai, R. Yuan, Z. Ding, J. Long, S-Scheme-Heterojunction LaNiO3/CdLa2S4 Photocatalyst for Solar-Driven CO2-to-CO Conversion, ACS Appl. Nano Mater. 6 (2023) 8936. https://doi.org/10.1021/ACSANM.3C01443/ASSET/IMAGES/LARGE/AN3C01443_0007.JPEG.

[118] M. Padervand, B. Rhimi, C. Wang, One-pot synthesis of novel ternary Fe3N/Fe2O3/C3N4 photocatalyst for efficient removal of rhodamine B and CO2 reduction, J. Alloys Compd. 852 (2021) 156955. https://doi.org/10.1016/J.JALLCOM.2020.156955.

[119] M. Padervand, S. Ghasemi, S. Hajiahmadi, C. Wang, K4Nb6O17/Fe3N/α-Fe2O3/C3N4 as an enhanced visible light-driven quaternary photocatalyst for acetamiprid photodegradation, CO2 reduction, and cancer cells treatment, Appl. Surf. Sci. 544 (2021) 148939. https://doi.org/10.1016/J.APSUSC.2021.148939.

[120] J. Fu, Q. Xu, J. Low, C. Jiang, J. Yu, Ultrathin 2D/2D WO3/g-C3N4 step-scheme H2-production photocatalyst, Appl. Catal. B Environ. 243 (2019) 556–565. https://doi.org/10.1016/J.APCATB.2018.11.011.

[121] Y. Wang, H. Yu, D. Wang, M. Xing, Y. Zhang, C. Song, Low proton adsorption energy barrier of S-scheme p-CNQDs/VO-ZnO for thermodynamics and kinetics favorable hydrogen evolution, Chem. Eng. J. 437 (2022) 135321. https://doi.org/10.1016/J.CEJ.2022.135321.

[122] H.T. Nguyen, H.M. Bui, Y.F. Wang, S.J. You, High flux and hydrogen peroxide-assisted photocatalytic antifouling membranes from coatings of Cu@ZrO2 onto plasma-grafted PAA/PES, Mater. Today Commun. 33 (2022) 104383. https://doi.org/10.1016/J.MTCOMM.2022.104383.

[123] L.L. Swelm Wageh, Ahmed A. Al-Ghamdi, S-Scheme Heterojunction Photocatalyst for

CO2 Photoreduction, Acta Phys. -Chim. Sin. 37 (2021) 10–11. https://doi.org/10.1002/adma.201802981.

[124] M. Mokhtar M. Mostafa, A. Shawky, S. Fakhruz Zaman, K. Narasimharao, M. Abdel Salam, A.A. Alshehri, N.H. Khdary, S. Al-Faifi, A. Dutta Chowdhury, Enhanced and recyclable CO2 photoreduction into methanol over S-scheme PdO/GdFeO3 heterojunction photocatalyst under visible light, J. Mol. Liq. 377 (2023) 121528. https://doi.org/10.1016/j.molliq.2023.121528.

[125] M.A. Ávila-López, J.Z.Y. Tan, E. Luévano-Hipólito, L.M. Torres-Martínez, M.M. Maroto-Valer, Production of CH4 and CO on CuxO and NixOy coatings through CO2 photoreduction, J. Environ. Chem. Eng. 10 (2022) 108199. https://doi.org/10.1016/j.jece.2022.108199.

[126] Z. Hai, J. Du, M.K. Akbari, C. Xue, Carbon-doped MoS2 nanosheet photocatalysts for efficient degradation of methyl orange, Ionics Vol. 23 (2017) 1921–1925. https://doi.org/10.1007/s11581-017-2144-4.

[127] R.R. Prabhu, A.C. Saritha, M.R. Shijeesh, M.K. Jayaraj, Fabrication of p-CuO/n-ZnO heterojunction diode via sol-gel spin coating technique, Mater. Sci. Eng. B. 220 (2017) 82–90. https://doi.org/10.1016/j.mseb.2017.03.008.

[128] N.T. Hoa, V. Van Cuong, N.D. Lam, Mechanism of the photocatalytic activity of p-Si (100)/n-ZnO nanorods heterojunction, Mater. Chem. Phys. 204 (2018) 397–402. https://doi.org/10.1016/j.matchemphys.2017.10.070.

[129] S.A. Rawool, M.R. Pai, A.M. Banerjee, A. Arya, R.S. Ningthoujam, R. Tewari, R. Rao, B. Chalke, P. Ayyub, A.K. Tripathi, S.R. Bharadwaj, pn Heterojunctions in NiO:TiO2 composites with type-II band alignment assisting sunlight driven photocatalytic H2 generation, Appl. Catal. B Environ. 221 (2018) 443–458. https://doi.org/10.1016/j.apcatb.2017.09.004.

[130] H. Yu, T. Yang, Z. Wang, Z. Li, Q. Zhao, M. Zhang, p-N heterostructural sensor with SnO-SnO2 for fast NO2 sensing response properties at room temperature, Sensors Actuators B. Chem. 258 (2018) 517–526. https://doi.org/10.1016/j.snb.2017.11.165.

[131] Y. Xiao, Y. Li, Nanomaterials design for photoelectrochemical water oxidation, Encycl. Nanomater. (2023) 515–532. https://doi.org/10.1016/B978-0-12-822425-0.00116-0.

[132] P. Augustine, Two-dimensional layered materials for efficient photodetection, Appl. Multifunct. Nanomater. (2023) 265–280. https://doi.org/10.1016/B978-0-12-820557-0.00015-1.

[133] M. Eshete, X. Li, L. Yang, X. Wang, J. Zhang, L. Xie, L. Deng, G. Zhang, J. Jiang, Charge Steering in Heterojunction Photocatalysis: General Principles, Design, Construction, and Challenges, Small Sci. 3 (2023) 2200041. https://doi.org/10.1002/smsc.202200041.

[134] L. Liu, Y. Zhang, H. Huang, Junction Engineering for Photocatalytic and Photoelectrocatalytic CO2 Reduction, Sol. RRL. 5 (2021) 1–19. https://doi.org/10.1002/solr.202000430.

[135] X. Wang, S. Wang, D. Su, S. Xu, S. Cao, Y. Xiao, Constructing a p-n heterojunction in 3D urchin-like CoNixSy/g-C3N4 composite microsphere for high performance asymmetric supercapacitors, J. Alloys Compd. 902 (2022) 163784. https://doi.org/10.1016/J.JALLCOM.2022.163784.

[136] X. Qiao, Z. Zhang, D. Hou, D. Li, Y. Liu, Y. Lan, J. Zhang, P. Feng, X. Bu, Tunable MoS2/SnO2 P−N Heterojunctions for an E ffi cient Trimethylamine Gas Sensor and 4 - Nitrophenol Reduction Catalyst, ACS Sustain. Chem. Eng. 6 (2018) 12375–12384. https://doi.org/10.1021/acssuschemeng.8b02842.

[137] D. Zhang, Z. Xu, Z. Yang, X. Song, High-performance flexible self-powered tin disulfide nanoflowers/reduced graphene oxide nanohybrid-based humidity sensor driven by triboelectric nanogenerator, Nano Energy. 67 (2020) 104251. https://doi.org/10.1016/j.nanoen.2019.104251.

[138] J. Hao, Y. Wang, SnS2/SnS p–n heterojunctions with an accumulation layer for ultrasensitive room-temperature NO2 detection, Nanoscale. 11 (2019) 13741. https://doi.org/10.1039/c9nr02780g.

[139] H. Tang, Y. Li, R. Sokolovskij, L. Sacco, H. Zheng, H. Ye, H. Yu, X. Fan, H. Tian, T. Ren, G. Zhang, Ultra-High Sensitive NO2 Gas Sensor Based on Tunable Polarity Transport in CVD-WS2/IGZO p-N Heterojunction, ACS Appl. Mater. Interfaces. 11 (2019) 40850–40859. https://doi.org/10.1021/acsami.9b13773.

[140] J.Z.Y. Tan, E. Lu, L.M. Torres-, M.A. Avila-l, M.M. Maroto-valer, Production of CH4 and CO on CuxO and NixOy coatings through CO2 photoreduction, J. Environ. Chem. Eng. 10 (2022) 108199. https://doi.org/10.1016/j.jece.2022.108199.

[141] G. Yang, P. Qiu, J. Xiong, X. Zhu, G. Cheng, Facilely anchoring Cu2O nanoparticles on mesoporous TiO2 nanorods for enhanced photocatalytic CO2 reduction through efficient charge transfer, Chinese Chem. Lett. 33 (2022) 3709–3712. https://doi.org/10.1016/j.cclet.2021.10.047.

[142] P. Qiu, J. Xiong, M. Lu, L. Liu, W. Li, Z. Wen, W. Li, R. Chen, Integrated p-n/Schottky junctions for efficient photocatalytic hydrogen evolution upon Cu@TiO2-Cu2O ternary hybrids with steering charge transfer, J. Colloid Interface Sci. 622 (2022) 924–937. https://doi.org/10.1016/j.jcis.2022.04.107.

[143] G.C. Zhangjing Chen, Xueteng Zhu, Jinyan Xiong, Zhipan Wen, A p-n Junction by Coupling Amine-Enriched Brookite-TiO2 Nanorods with CuxS Nanoparticles for Improved Photocatalytic CO2 Reduction, Materials (Basel). 16 (2023) 960.

[144] L. Jiang, K. Wang, X. Wu, G. Zhang, Highly Enhanced Full Solar Spectrum-Driven Photocatalytic CO2 Reduction Performance in Cu2–xS/g-C3N4 Composite: Efficient Charge Transfer and Mechanism Insight, Sol. RRL. 2000326 (2021) 1–12. https://doi.org/10.1002/solr.202000326.

[145] H. Zhao, C.F. Li, L.Y. Liu, B. Palma, Z.Y. Hu, S. Renneckar, S. Larter, Y. Li, M.G. Kibria, J. Hu, B.L. Su, n-p Heterojunction of TiO2-NiO core-shell structure for efficient hydrogen generation and lignin photoreforming, J. Colloid Interface Sci. 585 (2021) 694–704. https://doi.org/10.1016/J.JCIS.2020.10.049.

[146] S.F. Almojil, A.I. Almohana, A.F. Alali, R. Chaturvedi, S. Mehrez, A. Mohamed, S. Rashidi, Y. Cao, A novel g-C3N4-nanosheets/Ni3V2O8 n-p heterojunction

nanocomposite: A promising photocatalyst with enhanced photocatalytic degradation of tetracycline under visible light irradiation, Mater. Sci. Semicond. Process. 152 (2022) 107034. https://doi.org/10.1016/J.MSSP.2022.107034.

[147] C. Wang, Y. Li, L. Huang, L. Yang, H. Wang, J. Liu, J. Liu, Z. Song, L. Huang, Enhanced photocatalytic antibacterial and degradation performance by n-p type 0D/2D SnO2−x/BiOI photocatalyst under LED light, Chem. Eng. J. 411 (2021) 128505. https://doi.org/10.1016/J.CEJ.2021.128505.

[148] Y. Huang, J. Zhang, K. Dai, C. Liang, G. Dawson, Efficient solar-driven CO2 reduction on aminated 2D/2D BiOBr/CdS-diethylenetriamine S-scheme heterojunction, Ceram. Int. 48 (2022) 8423–8432. https://doi.org/10.1016/j.ceramint.2021.12.050.

[149] L. Jiang, Z. Li, D. Wang, T. Guo, Y. Hu, In-situ growth of p-type Ag2O on n-type Bi2O2S with intimate interfacial contact for NIR light-driven photocatalytic CO2 reduction, Appl. Surf. Sci. 601 (2022) 154185. https://doi.org/10.1016/j.apsusc.2022.154185.

[150] H. Wu, J. Bian, Z. Zhang, Z. Zhao, S. Xu, Z. Li, N. Jiang, E. Kozlova, X. Hua, L. Jing, Controllable synthesis of CuPc/N-rich doped (0 01) TiO2 S-scheme nanosheet heterojunctions for efficiently wide-visible light-driven CO2 reduction, Appl. Surf. Sci. 623 (2023) 157066. https://doi.org/10.1016/j.apsusc.2023.157066.

[151] Z. Guan, Y. Chen, Y. Ding, J. Lin, Y. Zhao, Y. Jiao, G. Tian, Efficient charge transfer and CO2 photoreduction of hierarchical CeO2@SnS2 heterostructured hollow spheres with spatially separated active sites, Appl. Surf. Sci. 592 (2022) 153192. https://doi.org/10.1016/j.apsusc.2022.153192.

[152] H. Deng, X. Fei, Y. Yang, J. Fan, J. Yu, B. Cheng, L. Zhang, S-scheme heterojunction based on p-type ZnMn2O4 and n-type ZnO with improved photocatalytic CO2 reduction activity, Chem. Eng. J. 409 (2021) 127377. https://doi.org/10.1016/j.cej.2020.127377.

[153] K.A. Alzahrani, A.A. Ismail, N. Alahmadi, CuCo2O4/CeO2 S-scheme photocatalyst for promoted CO2 photoreduction to CH3OH, J. Mol. Liq. 376 (2023) 0–9. https://doi.org/10.1016/j.molliq.2023.121509.

[154] C. Chen, J. Hu, X. Yang, T. Yang, J. Qu, C. Guo, C.M. Li, Ambient-Stable Black Phosphorus-Based 2D/2D S-Scheme Heterojunction for Efficient Photocatalytic CO2 Reduction to Syngas, ACS Appl. Mater. Interfaces. 13 (2021) 20162–20173. https://doi.org/10.1021/acsami.1c03482.

[155] X. Zhang, D. Kim, J. Yan, L.Y.S. Lee, Photocatalytic CO2 Reduction Enabled by Interfacial S-Scheme Heterojunction between Ultrasmall Copper Phosphosulfide and g-C3N4, ACS Appl. Mater. Interfaces. 13 (2021) 9762–9770. https://doi.org/10.1021/acsami.0c17926.

[156] J. Yang, J. Wang, W. Zhao, G. Wang, K. Wang, X. Wu, J. Li, 0D/1D Cu2-xS/TiO2 S-scheme heterojunction with enhanced photocatalytic CO2 reduction performance via surface plasmon resonance induced photothermal effects, Appl. Surf. Sci. 613 (2023) 156083. https://doi.org/10.1016/j.apsusc.2022.156083.

[157] Y.M. Dai, C.Y. Li, W.H. Ting, J.M. Jehng, Plasmon Ag/AgVO3/TiO2-nanowires S-scheme heterojunction photocatalyst for CO2 reduction, J. Environ. Chem. Eng. 10 (2022) 108045. https://doi.org/10.1016/j.jece.2022.108045.

[158] G. Xiao, J. Niu, Y. Fu, J. Cao, J. Wang, Y. Zheng, C. Li, J. Pan, Enhanced photocatalytic hydrogen evolution and CO2 to CH4 selectivity of Co3O4/Ti3+-TiO2 hollow S-scheme heterojunction via ZIF-67 self-template and Ti3+/Ov, Int. J. Hydrogen Energy. (2023) 1–12. https://doi.org/10.1016/j.ijhydene.2023.01.101.

[159] M. Tahir, B. Tahir, N.A.S. Amin, A. Muhammad, Photocatalytic CO2 methanation over NiO/In2O3 promoted TiO2 nanocatalysts using H2O and/or H2 reductants, Energy Convers. Manag. 119 (2016) 368–378. https://doi.org/10.1016/j.enconman.2016.04.057.

[160] C. Zhao, A. Zhou, Y. Dou, J. Zhou, J. Bai, J.R. Li, Dual MOFs template-directed fabrication of hollow-structured heterojunction photocatalysts for efficient CO2 reduction, Chem. Eng. J. 416 (2021) 129155. https://doi.org/10.1016/j.cej.2021.129155.

[161] J. Jiang, X. Zou, Z. Mei, S. Cai, Q. An, Y. Fu, H. Wang, T. Liu, H. Guo, Understanding rich oxygen vacant hollow CeO2@MoSe2 heterojunction for accelerating photocatalytic CO2 reduction, J. Colloid Interface Sci. 611 (2022) 644–653.

https://doi.org/10.1016/j.jcis.2021.12.108.

[162] X. Han, B. Lu, X. Huang, C. Liu, S. Chen, J. Chen, Z. Zeng, S. Deng, J. Wang, Novel p- and n-type S-scheme heterojunction photocatalyst for boosted CO2 photoreduction activity, Appl. Catal. B Environ. 316 (2022) 121587. https://doi.org/10.1016/j.apcatb.2022.121587.

[163] H. Li, T. Sun, L. Zhang, Y. Cao, Improved photocatalytic activity of ZnO via the modification of In2O3 and MoS2 surface species for the photoreduction of CO2, Appl. Surf. Sci. 566 (2021) 150649. https://doi.org/10.1016/j.apsusc.2021.150649.

[164] Z. Li, Z. Li, J. Liang, W. Fan, Y. Li, Y. Shen, D. Huang, Z. Yu, S. Wang, Y. Hou, Bi-functional S-scheme S-Bi2WO6/NiO heterojunction for photocatalytic ciprofloxacin degradation and CO2 reduction: Mechanisms and pathways, Sep. Purif. Technol. 310 (2023) 123197. https://doi.org/10.1016/j.seppur.2023.123197.

[165] Q. Zhang, X. Guan, X. Wang, X. Zhang, In-situ electrochemical-ion-exchange synthesis of S-scheme 1D/2D BiPO4/ BiOBr heterojunction film from Bi plate with highly efficient photocatalytic CO2 reduction activity, Catal. Commun. 177 (2023) 106664. https://doi.org/10.1016/j.catcom.2023.106664.

[166] Z. Miao, Q. Wang, Y. Zhang, L. Meng, X. Wang, In situ construction of S-scheme AgBr/BiOBr heterojunction with surface oxygen vacancy for boosting photocatalytic CO2 reduction with H2O, Appl. Catal. B Environ. 301 (2022) 120802. https://doi.org/10.1016/j.apcatb.2021.120802.

[167] Y. Xie, Y. Zhou, C. Gao, L. Liu, Y. Zhang, Y. Chen, Y. Shao, Construction of AgBr/BiOBr S-scheme heterojunction using ion exchange strategy for high-efficiency reduction of CO2 to CO under visible light, Sep. Purif. Technol. 303 (2022) 122288. https://doi.org/10.1016/j.seppur.2022.122288.

[168] N. Sun, M. Zhou, X. Ma, Z. Cheng, J. Wu, Y. Qi, Y. Sun, F. Zhou, Y. Shen, S. Lu, Self-assembled spherical In2O3/BiOI heterojunctions for enhanced photocatalytic CO2 reduction activity, J. CO2 Util. 65 (2022) 102220. https://doi.org/10.1016/j.jcou.2022.102220.

[169] H. Yang, J. feng Zhang, K. Dai, Organic amine surface modified one-dimensional CdSe0.8S0.2-diethylenetriamine/two-dimensional SnNb2O6 S-scheme heterojunction with promoted visible-light-driven photocatalytic CO2 reduction, Chinese J. Catal. 43 (2022) 255–264. https://doi.org/10.1016/S1872-2067(20)63784-6.

[170] X. Guo, T. Fowjsponfoubm, Q. Boe, F. Dsjtft, Controllable synthesized step-scheme heterojuction of CuBi2O4 decorated WO3 plates for visible-light-driven CO2 reduction, Nano Res. 15 (2022) 5962–5969.

[171] Z. Zhang, X. Liu, L. Yuanling, H. Yu, W. Li, H. Yu, Unveiling the role of Ag-Sb bimetallic S-scheme heterojunction for vis-NIR-light driven selective photoreduction CO2 to CH4, Appl. Catal. B Environ. 319 (2022) 121960. https://doi.org/10.1016/j.apcatb.2022.121960.

[172] H. Li, D. Wang, C. Miao, Y. Wang, Y. Wang, C. Liu, G. Che, g-C3N4/BiOI S-scheme heterojunction: A2D/2D model platform for visible-light-driven photocatalytic CO2 reduction and pollutant degradation, J. Environ. Chem. Eng. 10 (2022) 108201.

[173] S. She, B. Zhao, J. Wang, Z. Wei, X. Wu, Y. Li, Construction of Bi2O3 quantum Dots/SrBi4Ti4O15 S-scheme heterojunction with enhanced photocatalytic CO2 reduction: Role of Bi2O3 quantum dots and mechanism study, Sep. Purif. Technol. 309 (2023) 123064. https://doi.org/10.1016/j.seppur.2022.123064.

[174] X. Li, Z. Wang, J. Zhang, K. Dai, K. Fan, G. Dawson, Branch-like CdxZn1-xSe/Cu2O@Cu step-scheme heterojunction for CO2 photoreduction, Mater. Today Phys. 26 (2022) 1–10. https://doi.org/10.1016/j.mtphys.2022.100729.

[175] Z. Wang, B. Cheng, L. Zhang, J. Yu, Y. Li, S. Wageh, A.A. Al-Ghamdi, S-Scheme 2D/2D Bi2MoO6/BiOI van der Waals heterojunction for CO2 photoreduction, Chinese J. Catal. 43 (2022) 1657–1666. https://doi.org/10.1016/S1872-2067(21)64010-X.

[176] M. Padervand, S. Ghasemi, S. Hajiahmadi, B. Rhimi, Z.G. Nejad, S. Karima, Z. Shahsavari, C. Wang, Multifunctional Ag/AgCl/ZnTiO3 structures as highly efficient photocatalysts for the removal of nitrophenols, CO2 photoreduction, biomedical waste treatment, and bacteria inactivation, Appl. Catal. A Gen. 643 (2022) 118794.

https://doi.org/10.1016/J.APCATA.2022.118794.

[177] C. Cometto, R. Kuriki, L. Chen, K. Maeda, T.C. Lau, O. Ishitani, M. Robert, A Carbon Nitride/Fe Quaterpyridine Catalytic System for Photostimulated CO2-to-CO Conversion with Visible Light, J. Am. Chem. Soc. 140 (2018) 7437–7440. https://doi.org/10.1021/JACS.8B04007/ASSET/IMAGES/LARGE/JA-2018-04007X_0002.JPEG.

[178] S. Gao, Q. Zhang, X. Su, X. Wu, X.G. Zhang, Y. Guo, Z. Li, J. Wei, H. Wang, S. Zhang, J. Wang, Ingenious Artificial Leaf Based on Covalent Organic Framework Membranes for Boosting CO2 Photoreduction, J. Am. Chem. Soc. 145 (2023) 9520–9529. https://doi.org/10.1021/JACS.2C11146/ASSET/IMAGES/LARGE/JA2C11146_0006.JPEG.

[179] J. Yuan, P. Wang, C. Hao, G. Yu, Photoelectrochemical reduction of carbon dioxide at CuInS2/graphene hybrid thin film electrode, Electrochim. Acta. 193 (2016) 1–6. https://doi.org/10.1016/J.ELECTACTA.2016.02.037.

[180] A. Sudhaik, Sonu, V. Hasija, R. Selvasembian, T. Ahamad, A. Singh, A.A.P. Khan, P. Raizada, P. Singh, Applications of graphitic carbon nitride-based S-scheme heterojunctions for environmental remediation and energy conversion, Nanofabrication. 8 (2023) 1–37. https://doi.org/10.37819/nanofab.008.292.

[181] C. Luo, Q. Long, B. Cheng, B. Zhu, L. Wang, A DFT Study on S-Scheme Heterojunction Consisting of Pt Single Atom Loaded G-C3N4 and BiOCl for Photocatalytic CO2 Reduction, Wuli Huaxue Xuebao/ Acta Phys. - Chim. Sin. 39 (2023). https://doi.org/10.3866/PKU.WHXB202212026.

[182] L. Cheng, X. Yue, J. Fan, Q. Xiang, Site-Specific Electron-Driving Observations of CO2-to-CH4 Photoreduction on Co-Doped CeO2/Crystalline Carbon Nitride S-Scheme Heterojunctions, Adv. Mater. 34 (2022). https://doi.org/10.1002/adma.202200929.